University of Strathclyde
Department of Physics
Photophysics Research Group

Fluorescence Lifetime Activated Cell Screening (FLACS) Platform for Cancer Cell Study

A Thesis submitted to the University of Strathclyde for the degree of

Doctor of Philosophy

By

Natakorn Sapermsap

Declaration

This thesis is the result of the author's original research. It has been composed by the author and has not been previously submitted for examination which has led to the award of a degree.

Signed: 

Date: 12 January 2024

Acknowledgements

I would like to express my deepest gratitude and appreciation to the following individuals and organisations who have supported and contributed to the completion of this thesis:

First and foremost, I am very grateful to my supervisors, Yu Chen and David Birch, for their invaluable guidance, expertise, and unwavering support throughout this research project. Their insightful feedback and encouragement have been instrumental in shaping the direction of this thesis.

I am grateful to the faculty and staff of the Physics department for providing a conducive academic environment and access to resources that have been essential for my research. Their commitment to excellence has been truly inspiring. I would like to acknowledge the support and encouragement from my colleagues and friends who have been with me throughout this academic journey. Their stimulating discussions, encouragement, and camaraderie have made this experience more rewarding.

I also would like to extend my sincere appreciation to the colleagues from the Biomedical Engineering department, David Li and his group for their time, expertise, and constructive feedback. Their input has significantly enriched the quality of this work.

I am deeply indebted to my family and my girlfriend for their unwavering mental support, love, and understanding. Their constant encouragement and belief in my abilities have been the driving force behind my perseverance.

While I have made every effort to acknowledge everyone who has contributed to this thesis, I apologise if I have unintentionally omitted anyone. Please know that your support and assistance have not gone unnoticed and are sincerely appreciated.

Thank you all once again for being a part of this journey and for your invaluable contributions.

Natakorn Sapermsap

Lists of publications

1. Lifetime determination algorithms for time-domain fluorescence lifetime imaging: a review. Y. Li, L. Liu, D. Xiao, H. Li, N. Sapermsap, J. Tian, Y. Chen, D. Li, Fluorescence Imaging - Recent Advances and Applications, Ed Raffaello Papadakis, IntechOpen (2022).

2. Deep learning enhanced fast fluorescence lifetime imaging with a few photons, D. Xiao, N. Sapermsap, Y. Chen, D.D.U. Li, Optica (accepted).

3. Spatial resolution improved fluorescence lifetime imaging via deep learning, D. Z. Zhang, Xiao, W. Xie, N. Sapermsap, Y. Chen, D. Li. Optics Express Vol 30, pp. 11479-11494 (2022).

4. Investigations on average fluorescence lifetimes for visualizing multiexponential decays, Y. Li, N. Sapermsap, Y. Chen, M. Safar, M. Cunningham, J. Tian, D. Li, Frontiers in Physics: Optics and Photonics, Vol 8, 576862 (2020).

5. Histogram clustering for rapid time-domain fluorescence lifetime image analysis, Y. Li, N. Sapermsap, J. Yu, J. Tian, Y. Chen and D. Li Biomedical Optics Express, 12, 4293 (2021).

6. Sapermsap N, Li DD, Al-Hemedawi R, Li Y, Yu J, Birch DJ, Chen Y. A rapid analysis platform for investigating the cellular locations of bacteria using two-photon fluorescence lifetime imaging microscopy. Methods and Applications in Fluorescence (2020).

7. Xiao, D., Zang, Z., Sapermsap, N., Wang, Q., Xie, W., Chen, Y., & Li, D. D. U. Dynamic fluorescence lifetime sensing with CMOS single-photon avalanche diode arrays and deep learning processors. Biomedical Optics Express (2021).

8. Xiao, D., Sapermsap, N., Safar, M., Cunningham, M. R., Chen, Y., & Li, D. D-U. On synthetic instrument response functions of time-correlated single-photon counting based fluorescence lifetime imaging analysis. Frontiers in Physics (2021).

9. Sapermsap N et al., Fluorescence lifetime activated cell screening (FLACS) platform for cancer cell screening. (In preparation)

Presentations

"Fluorescence lifetime detection in flowing cells" oral presentation presented at the 1st year Postgraduate Institute Conference held at Ross Priory, Glasgow (2019).

"Fluorescence lifetime detection in flowing cells" poster presented at the 2nd year Postgraduate Institute Conference held at the University of Strathclyde (Online), Glasgow (2020).

Abstract

The lack of sensitive and affordable tools for rapid and reliable cancer diagnosis remains a major obstacle to reducing cancer mortality. Biopsy, the most commonly used diagnostic tool, involves lengthy multiple processes and costly reagents. Additionally, the outcome of a biopsy depends on the experience of assessors, and interpretation is often subjective. To address these issues, we developed a rapid and high throughput fluorescence lifetime-activated cell screening (FLACS) platform to distinguish between cancer and non-cancer cells based on a flow cytometer (FCM) setup and straightforward time-domain measurements using the novel single photon avalanche diode (SPAD) camara cooperating with the fast fit-free lifetime calculation method including centre of mass (CMM) method and phasor plot.

The FLACS prototype combines FCM with a wide-field microscope equipped with a 192x128 SPAD camera, which is characterised and configured as a Megapixel. The sample is injected by a syringe pump and hydrodynamically focused into a narrow stream inside a flow cell down to 45 μm using sheath fluid, such as distilled water or PBS, driven by a peristaltic pump. The flow cell is based on the microscope slide design with 210 x 70 μm microfluidic channel. A graphic user interface (GUI) software has been developed to control and configured the SPAD camera, receive time-resolved fluorescence data, and analyse using fast and fit-free methods. Moreover, multiple FCM parameters can be graphically displayed as distribution and scattering plots, and the software also allows users to selectively identify some areas of the plots to specifically analyse sub-population. This helps the users to understand the insight of the sample and to easily distinguish sample populations. The current development of the platform shows speedy performance with a maximum detection rate of 1147 frames per second (fps), while the optimal speed is 309 fps with the least possibility of miscounted particles due to the dead time from data transferring and processing.

In order to distinguish between cancer and non-cancer cells, an RNA nanoprobe for cancer cell detection is synthesised and tested with complementary deoxyribonucleic acid (cDNA) prior to human embryonic kidney 293 (HEK293) and human prostate cancer (PC3) cell lines. The nanoprobe design is based on a gold nanorod core with hairpin oligonucleotides (hpDNA) labelled with Cyanine-5 (Cy5), which is initially in a quenched state through Förster resonance energy transfer (FRET) and becomes fluorescent after hybridisation with

target ribonucleic acid (RNA). The 291% and 76% increase in fluorescence intensity and lifetime, respectively, were observed after incubating the nanoprobe with the target RNA.

To ensure the accuracy and reliability of measuring before proceeding to the precious nanoprobe with cell lines, the platform undergoes testing using C- and YG-fluorescent microspheres (C- and YG-beads). These beads mock-up positive and negative cell lines by mimicking their long and short fluorescence lifetimes, as well as strong and weak intensity characteristics, respectively. By flowing a single type of bead, the platform can detect the fluorescence lifetime of 1.89 ± 0.10 ns and 1.49 ± 0.66 ns for C- and YG- beads, respectively. For mixed bead samples, the data is extracted using an intensity threshold of > 285 photons and using phasor position acquired from single-type bead measurement to neglect the events without beads, and to filter the events with C- and YG- beads showing the extracted lifetime of 1.87 ± 0.13 ns and 1.64 ± 0.43 ns, respectively. By combining the prototype with the RNA nanoprobe, this platform can successfully detect the flowing PC3 cell lines incubated with the RNA nanoprobe for 2 hours, which shows a lifetime of 1.34 ± 0.34 ns, longer than 1.14 ± 0.26 ns in the case of HEK293 cell lines. This trend follows the results acquired from the fluorescence lifetime imaging microscopy (FLIM) technique, which shows the lifetime values of 1.25 ± 0.43 ns and 0.93 ± 0.02 ns for PC3 and HEK293 cases, respectively, demonstrating the capability for differentiating cancer cells from non-cancer cells using the FLACS platform.

Our FLACS platform has the potential to improve cancer diagnosis by providing a rapid, reliable, and alternative measurement to traditional biopsy methods. Future development will focus on improving the platform's sensitivity and specificity, validating its performance in clinical settings, and optimising the RNA nanoprobe for improved cancer detection.

Abbreviations

ADC	Analouge to Digital Converter
CCD	Charge-Coupled Device
cDNA	Ccomplementary DNA
CFD	Constant Function Discriminator
CMM	Centre of Mass Method
CMOS	Complementary Metal Oxide Semiconductor
c-Myc	Myelocytomatosis oncogene
cps	Count Per Secound
CT	Computed Tomography
CTAB	Cetyltrimethylammonium Bromide
Cy5	Cyanine-5
DDT	Dichlorodiphenyltrichloroethane
DNA	Deoxyribonucleic Acid
EGFP	Enhanced Green Fluorescent Protein
FCM	Flowcytometer
FLACS	Fluorescence Activated Cell Screening
FLIM	Fluorescence Lifetime Imaging Microscopy
FOV	Field Of View
fps	Frame per second
FRET	Förster resonance energy transfer
FSC	Forward Scattering
FWHM	Full Width Half Maximum
GFP	Green Fluorescent Protein
GNR	Gold Nanorod
GUI	Graphic User Interface
HEK293	Human Embryonic Kidney cell line
Hela	Cervial Cancer cell line
hpDNA	hairpin DNA
Im	Imaginary part
LSB	Least Significant Bit
LSPR	Localisation Surface Plasmon Resonance
LUT	Look Up Table
MHA	Mercapto Hexadecanoic Acid
MRI	Magnetic Resonance Imaging
mRNA	messenger RNA

MSB	Most Significant Bit
ND	Natural Density
NLLS	Non-Linear Least Square
PBS	Phosphate Buffer Saline
PC3	Prostate Cancer cell line
PCB	Printed Circuit Board
PGA	Programmable Gain Amplifier
PMT	Photomultiplier Tube
Re	Real part
RF	Radio Frequency
RFP	Red Fluorescent Protein
RNA	Ribonucleic Acid
ROI	Region Of Interest
SET	Surface Energy Transfer
SNR	Signal-to-Noise Ratio
SPAD	Single Photon Avalanche Diode
SSC	Side Scattering
TAC	Time to Analouge Converter
TE	Tris-EDTA buffer
TCEP	tris(2-carboxyethyl)phosphine
TCSPC	Time-correlated Single Photon Counting
TDC	Time to Digital Converter
TPE	Two Photon Excitation
TBE	Tris-Borate-EDTA
UV-Vis	Ultraviolet to Visible
WD	Window Discriminator

Contents

List of Figures

List of Tables

Chapter 1 Introduction

Since the discovery of fluorescence, a new non-invasive method of physical, biological, and chemical characterisation has been developed. Fluorescence spectroscopy and microscopy have become the most powerful tool and are widely used in biological studies and clinical applications. In cancer liquid biopsy, it is essential to detect rare events, such as circulating tumour cells or specific cancer-related markers present in low abundance in the blood. These rare events could hold critical diagnostic and predictive information. Traditional methods might not be sensitive enough to detect these infrequent occurrences accurately. Flow cytometer (FCM), with its ability to identify and quantify rare events, becomes a valuable tool of liquid biopsy for cancer detection and monitoring. In addition, FCM offers a high-throughput capability as it can process a large number of cells rapidly. This allows for the efficient analysis of a significant number of cells in a short period. Additionally, FCM can provide valuable data about cell populations, such as the percentage of specific cell types, which is crucial for understanding the characteristics of a sample and its implications in cancer diagnostics.

In the last few decades, the FCM is being developed and relies on fluorescence intensity detection to distinguish and analyse sample properties. The result of traditional FCM can be affected by variation in laser intensity and local concentration of fluorophore. On the other hand, time resolved FCM is not affected by these variations. Additionally, fluorescence lifetime measurement can be used to differentiate between mixed fluorophore populations that emit similar fluorescence intensities or overlapping emission spectra but different lifetimes. Time-resolved FCM has gained popularity in the biological sciences, particularly in the study of cellular metabolism and protein-protein interactions through Förster resonance energy transfer (FRET) mechanisms [1]. This technique also allows for the observation of fluorescence lifetime changes that result from structural alterations in proteins, providing valuable insights into cellular processes [2]. It is also useful in cell sorting, where it can be used to sort cells based on their fluorescence lifetime rather than their fluorescence intensity.

This thesis aims to develop a prototype of a fluorescence lifetime-based FCM, or fluorescence lifetime-activated cell screening (FLACS) system for cancer cell screening. This system will utilise fluorescence lifetime measurement to provide a new and improved method for cell analysis in biological and medical applications. The research will focus on optimising the design and performance of the prototype, exploring its potential applications in the early

diagnosis of cancer, and implementing fluorescence lifetime to flow cytometry analysis. Through the integration of cutting-edge technology and advanced algorithms, this thesis demonstrates the possibility of lifetime-based flow cytometry and creates a way for its widespread use in biological research. The final goal of this research is to provide a more accurate, efficient, and cost-effective tool for cell analysis and contribute to the advancement of knowledge in the field of life sciences.

In this chapter, the basics of the fluorescence process were introduced, followed by a survey on fluorescence and lifetime detection in the flow cytometry technique. Followed by the motivation of this work, the fluorescence lifetime will be brought as the new parameter of FCM and discuss where is our position of time-resolved FCM in the commercial market, as well as compare the available fast and fit-free methods.

1.1 Fluorescence Photophysics

Fluorescence is the ability of a substrate to absorb at a specific wavelength and emits light in some future time with a longer wavelength. The fluorescence process can be described using Jablonski's diagram (Figure 1.1) [1].

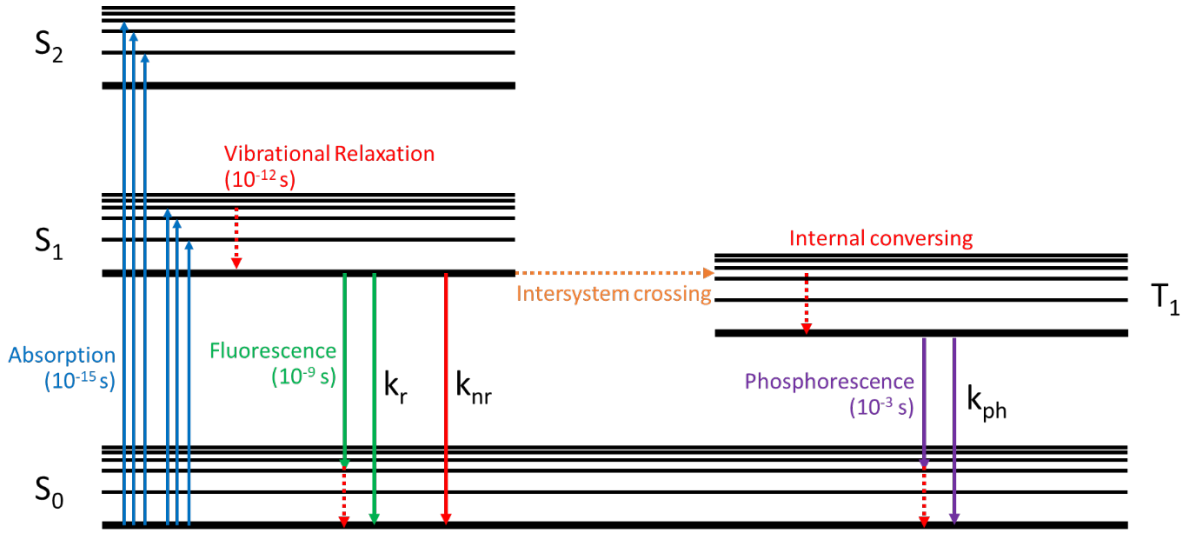

Figure 1.1 Jablonski diagram where S_0, S_1 and S_2 represent the electronic ground state, first and second excited states respectively, while T_1 represents the first triplet electronic excited state. The excited fluorophore is followed by rapid vibrational relaxation to the lowest vibration excited state in S_1 and returns to the ground state radiatively (k_r) or non-radiatively (k_{nr}). The phosphorescence emission (k_{ph}) occurs after intersystem crossing to T_1.

As stated by the Jablonski diagram (Figure 1.1), describes the process of fluorophore after absorbing excitation light. S_0, S_1, S_2 represent the ground, first excited and second excited

singlet electronic state and T_1 describes the first excited triplet electronic state. Absorption of a photon occurs when the fluorophore absorbs a photon which has higher energy than its electronic bandgap. The fluorophore is then excited from the ground state S_0 (lowest energy state) to any vibrational state of S_1 or S_2, usually spending 10^{-15} s transition time. Therefore, the absorption profile contains information on the bonding and structure of fluorophores and the vibrational state of S1 and S2. Immediately, the fluorophore loses energy and relaxes to the lowest vibrational of S_1 by internal conversion, which generally occurs within 10^{-12} s. Then the fluorophore either radiatively (at a rate k_r) or non-radiatively (at a rate k_{nr}) decays. In the radiative decay, fluorescence occurs when the fluorophore relaxes from the lowest vibrational state of S_1 to any vibrational state of S_0 (Kasha's Rule) and contains information on the vibrational spacing of S_0. The fluorescence process usually occurs with a lifetime near 10^{-9} s, whereas the slower process, called phosphorescence, occurs when the relaxation happens from the triplet state. In the case of non-radiative decay, the process generates heat, then the fluorophore relaxes to the ground state. The absorption and the radiative decay normally occur from the lowest vibrational state. The fluorescence is isotropic and can be detected in all directions (Figure 1.2). Typically, the emitted photon has lower energy compared to the absorbed photon and there is a right shift (red shift) of the emission peak compared to the absorption peak, called Stokes shift (Figure 1.3) enabling the usage of long-pass (LP) or band-pass (BP) filter to extract emitted signal from the excitation light.

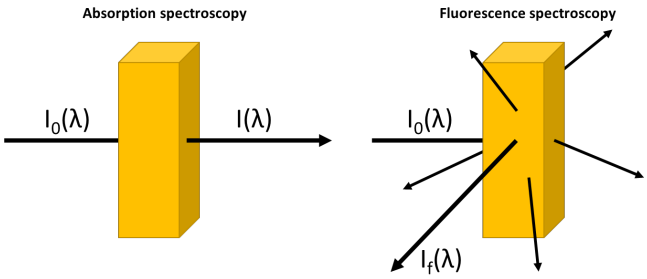

Figure 1.2 (a) measurement of absorption, and (b) fluorescence spectra, adapted from [2]

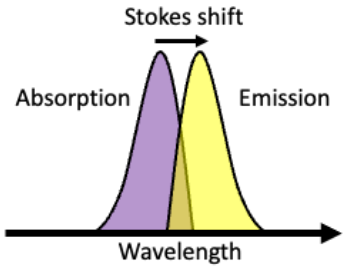

Figure 1.3 An illustration of Stokes shift showing the shifted peak wavelength due to energy losses during the relaxation process

1.1.1 Fluorescence lifetime and quantum yield

Fluorescence lifetime and quantum yield are two common important characteristics of a fluorophore. Fluorescence is a complex process in that not every absorbed photon results in radiative decay. This is described by quantum yield, which is the ratio of the number of emitted to absorbed photons expressed by Equation 1.1.

$$Q = \frac{k_r}{k_r + k_{nr}} \tag{1.1}$$

where Q is quantum yield, k_r is the radiative decay rate and k_{nr} is the non-radiative decay rate, and $k_r + k_{nr}$ is the total decay rate. The value of quantum yield is between 0 – 1 (0 – 100%) and the high quantum yield values indicate a higher number of absorbed photons are emitted. Typically, the quantum yield is always less than 1 because of energy loss. In addition, direct measurement of quantum yield is a difficult process because the emission occurs in every direction. The fluorophore must be placed in the middle of the photon-collecting sphere to integrate all emitted photons.

Fluorophore normally stays excited for a short period on a nanosecond scale before emitting a photon and going back to the ground state. The emission is a random process and the lifetime is mainly based on a statistical average. The fluorescence lifetime is defined as the average time that a fluorophore spends in an excited state before returning to the ground state and emitting a photon and this time can be varied from picoseconds to nanoseconds [4], [5]. Fluorescence lifetime measurement has been shown to offer several advantages over traditional intensity-based measurements, particularly in samples that exhibit spectrally overlapping emissions with distinct lifetime properties, show variations in excitation intensity, have variations of localised fluorophore concentrations, and exhibit strong autofluorescence such as biological sample [6]. These measurements provide valuable information regarding environmental parameters such as pH, temperature, viscosity, molecular interactions, and energy transfer[3]. It has also been demonstrated that fluorescence lifetime can be influenced by metal-enhanced processes [7] and the solvent in which the sample is suspended [8].

The decay rate is described by Equation 1.2 where all molecules M are initially brought to the excited state and the decay happens via radiative or non-radiative route to the ground state.

$$\frac{d[M^*]}{dt} = -(k_{nr} + k_r)[M^*] \tag{1.2}$$

where $d[M^*]/dt$ is the decay rate and $[M^*]$ is the molecular concentration of excited molecules M. The solution of this equation is Equation 1.3, which is in exponential decay form describing the emission intensity over time when the molecule is excited by δ-function at t = 0.

$$I(t) = I_0 exp\left(-\frac{t}{\tau}\right) \tag{1.3}$$

where $I(t)$ is the fluorescence intensity at time t, which is proportional to the remaining molecules in the excited state, I_0 is the intensity at t = 0 and τ is the fluorescence lifetime of the fluorophore. In addition, the lifetime can be written as the inverse of the sum of the decay rate, as shown in Equation 1.4 [3]. For a single exponential, the intensity will approximately drop to 63% of I_0 at $t = \tau$. However, complex fluorophores need a multi-exponential decay model written by Equation 1.4, which is modified from Equation 1.3 and its average lifetime is expressed by Equation 1.5.

$$I(t) = \sum_{i=1}^{n} \alpha_i exp\left(-\frac{t}{\tau_i}\right) \tag{1.4}$$

$$\bar{\tau} = \frac{\sum_{i=1}^{n} \alpha_i \tau_i}{\sum_{i=1}^{n} \alpha_i} \tag{1.5}$$

where n is the number of lifetime components, α_i is the relative amplitude and τ_i is the lifetime of each component. The lifetime can also be defined in term of the inverse of the total decay rate (Equation 1.6)

$$\tau = \frac{1}{k_r + k_{nr}} \tag{1.6}$$

Based on Equations 1.1 and 1.6, the lifetime can be written in terms of quantum yield as Equation 1.7

$$\tau = \frac{Q}{k_r} \tag{1.7}$$

1.1.2 Fluorescence quenching and energy transfer

Fluorescence quenching is a molecular process that can decrease fluorescence intensity. The quenching process can be categorised into three types of quenching: static quenching, dynamic quenching and FRET. Static quenching is caused by the formation of a non-fluorescent complex of quencher with the fluorophore in the ground state and the fluorophore is no longer capable to emit photons. Static quenching does not affect the fluorophore's excited state; therefore, the lifetime is unchanged [2]. The reduced intensity of static quenching can be described by Equation 1.8 below.

$$\frac{I_0}{I} = 1 + K_s[Q] \tag{1.8}$$

where I_0 and I correspond to fluorescence intensity with and without quencher Q respectively, $[Q]$ is quencher concentration, and K_S is a static quenching constant indicating the ratio of the non-fluorescent complex formed. Dynamic quenching (or collisional quenching) is the deactivation process of fluorophore in the excited state caused by collision with quencher molecules. The energy in the excited molecule is transferred to the quencher resulting in the fluorophore returning to the ground state faster and this process shortens the lifetime. The quenched intensity and lifetime of dynamic quenching can be described by Equation 1.9 and 1.10 below.

$$\frac{I_0}{I} = 1 + K_D[Q] \tag{1.9}$$

$$\frac{\tau}{\tau_0} = 1 + k_q\tau_0[Q] \tag{1.10}$$

where K_D is the Stern-Volmer dynamic quenching constant relating to the sensitivity of fluorophore to the quencher, k_q is the quenching constant and τ and τ_0 are quenched and unquenched lifetime respectively. Dynamic quenching is greatly diffusion dependent that requires an excited fluorophore and quencher in contact. Therefore, a higher temperature can increase the kinetic energy of the quencher leading to more possibility of collision. A typical example of a dynamic quencher is oxygen, which is common and well-known [9].

Another quenching mechanism is FRET, which is known as Förster resonance energy transfer from a donor fluorophore to an acceptor fluorophore. The FRET process can be described using the Jablonski diagram of FRET in Figure 1.5. Initially, the donor fluorophore is in the excited state, then may transfer its energy to the acceptor fluorophore through a non-radiative dipole-dipole interaction where the energy transfer rate depends on spectral overlap between the donor's emission and acceptor's absorption, and the distance between donor and acceptor. This process reduces the fluorescence intensity and lifetime of the donor while increasing the fluorescence intensity of the acceptor. FRET is extremely sensitive to distance and can only occur in a very short distance (typically ≤10 nm depending on R_0 [2]) (Figure 1.4), and the energy transfer efficiency is given by Equations 1.11.

$$E_{FRET}(r) = \frac{1}{1 - \left(\frac{r}{R_0}\right)^6} \tag{1.11}$$

where r is the distance between acceptor and donor, R_0 is the critical distance (Förster distance) at which the energy transfer efficiency is 50%, τ_D is donor fluorescence lifetime in the absence of acceptor, E_{FRET} is FRET efficiency and k_{FRET} is energy transfer rate. FRET is

also known as a spectroscopic ruler due to the distance-dependent property allowing intermolecular distance measurement.

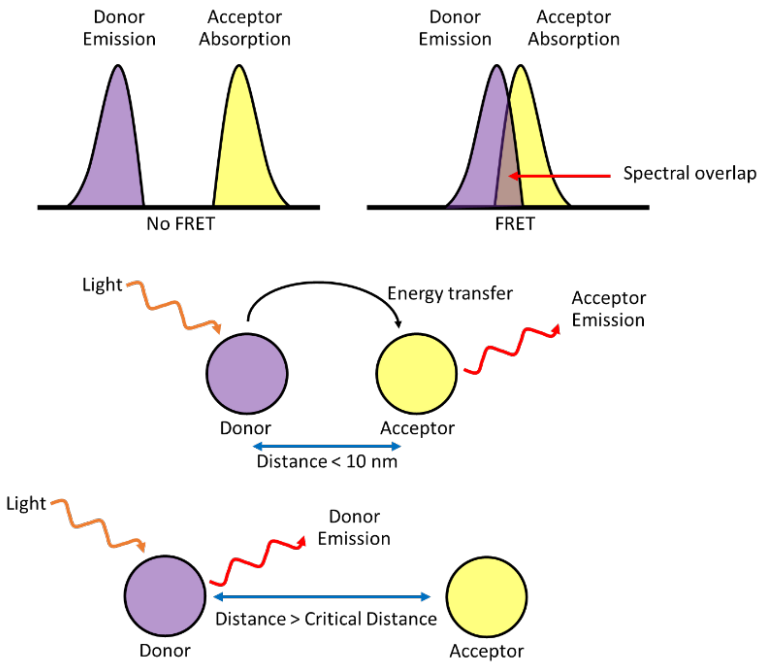

Figure 1.4 Diagram of FRET between donor and acceptor. FRET does not occur when the acceptor absorption does not overlap with the donor emission, and the distance exceeds the critical distance.

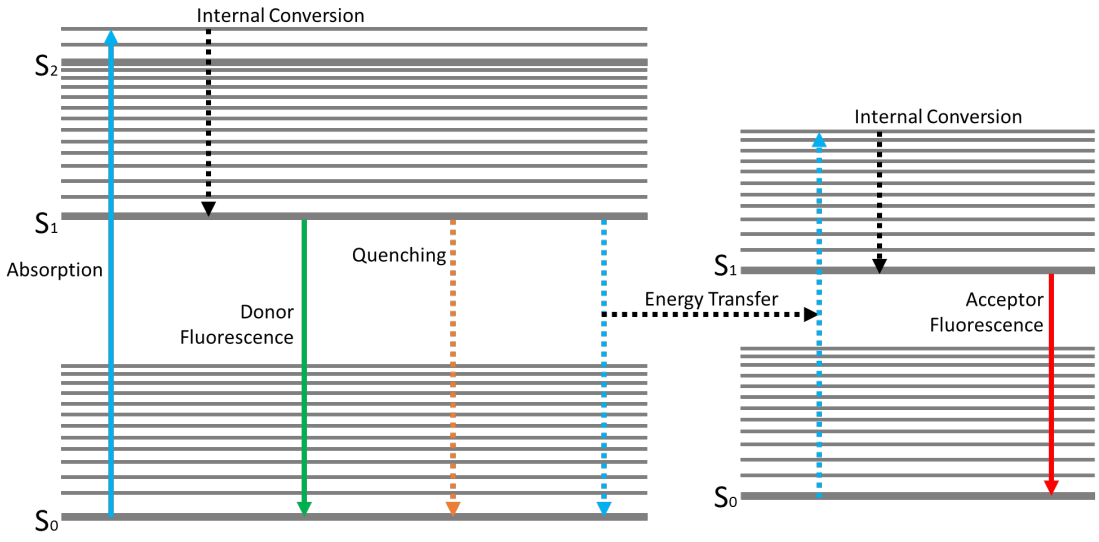

Figure 1.5 Jablonski diagram of FRET indicating a coupled transition between donor emission and acceptor absorption.

In the case of donor and acceptor surfaces such as gold nanoparticles, the energy transfer occurs as a result of the interaction between the electric field of the dipole and the surface plasmons of gold. This is called surface energy transfer (SET), which is dependent on the distance between the dipole and the metal surface, while the transfer efficiency is given by Equations 1.12, where d is the distance between the fluorophore and the gold surface and d_0 is the surface energy transfer (SET) radius [10], [11].

$$E_{FRET}(r) = \frac{1}{1 - \left(\frac{d}{d_0}\right)^4} \tag{1.12}$$

A gold nanorod (GNR) is a cylindrical nanostructure with typical size over 50 nm in length and 11 – 15 nm in diameter. The GNR generates strong absorption due to the localised surface plasmon resonance (LSPR) and the absorption peaks is tuneable by adjusting the aspect ratio (length/diameter) [12]. In addition, GNR has been widely used in nanomedicine as a drug delivery agent and cancer detection because of its less toxicity compared to the other types of nanoparticles [13]. The GNR has been reported that can act as the acceptor [14]–[16] when the emission of fluorophore spectrally overlaps with the absorption of GNR caused by localised surface plasmon resonance. The fluorescence intensity and lifetime are reduced by SET when the fluorophore is close enough to the GNR. Therefore, the GNR can be used as biological probes for biomedical studies such as cellular imaging, monitoring cells and messenger ribonucleic acid (mRNA) detection. Wei et al. and Mbalaha et al. demonstrated an mRNA nanoprobe design based on gold nanorod functionalised with hpDNA for early-stage cancer detection and treatment [17], [18]. As shown in Figure 1.6, in case of the absence of the ribonucleic acid (RNA) target, the Cyanine-5 (Cy5) is close to the dye enough to enable FRET causing Cy5 to have low intensity and short lifetime. After introducing the target RNA, the structure of the hairpin changes to linear increasing Cy5-GNR distance. This greatly reduces FRET efficiency resulting in higher fluorescence intensity and longer lifetime.

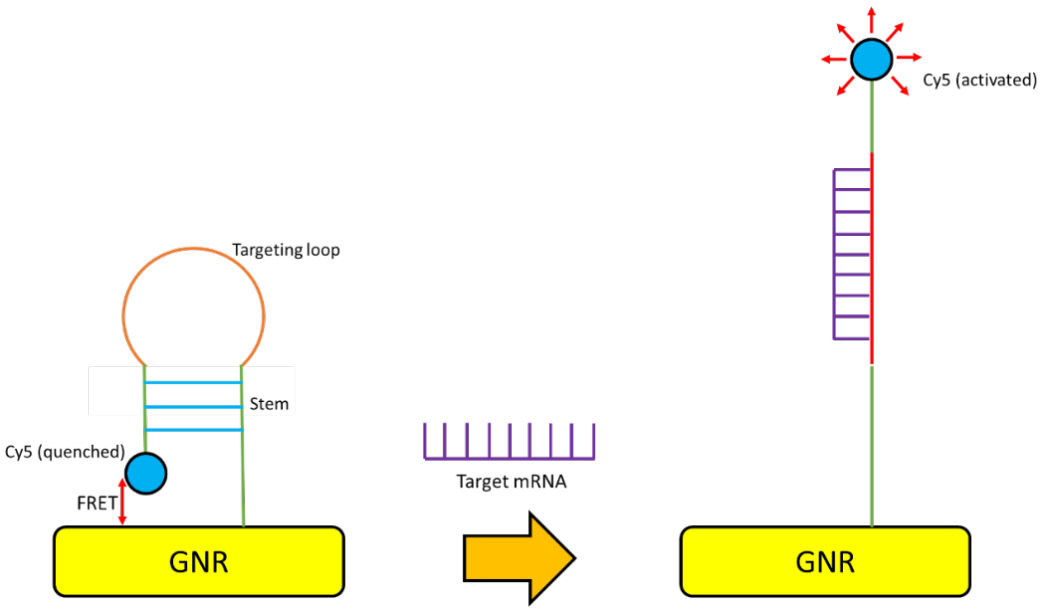

Figure 1.6 Illustration of hpDNA functionalised GNR for mRNA detection: closed-loop with FRET (left) and opened-loop without FRET (right). The image is adapted from [17]

1.1.3 Two-photon luminescence

Multi-photon luminescence is a luminescence process in which a fluorophore absorbs multiple low-energy photons simultaneously and emits high-energy photons. This process requires a high photon density excitation source and heavily relies on the probability that the required number of photons is present at the same time in a measurement area [3]. The illustration of multi-photon luminescence is shown in Figure 1.7. Two-photon excitation fluorescence is defined by the simultaneous absorption of two identical photons, which provides the total energy required for the fluorescence process.

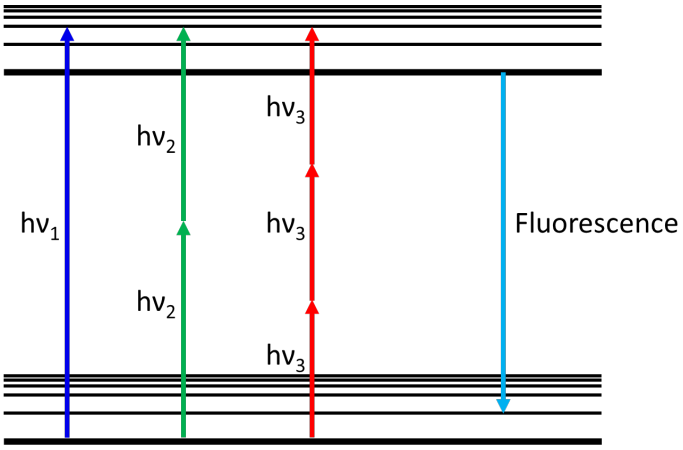

Figure 1.7 Diagram of single and multi-photon excitation. The image is adapted from [3]

The actual excitation area is smaller than the size of the laser beam illuminating the fluorophores because this phenomenon relies on two-photon absorption, necessitating two laser photons to arrive simultaneously, two photons in an extremely short time window, at the interaction region. The laser beam energy E in the measurement area is given by Equation 1.13.

$$E = PT = m\left(\frac{hc}{\lambda}\right) \tag{1.13}$$

where m is the mean photon number depending on the optical power P and on the time frame considered T, h is Plank's constant, λ is the wavelength, and c is light speed. Because the photon statistics of a laser is poissonian, which is the probability distribution used to describe two-photon excitation (TPE) fluorescence. The probability that two photons arrive at the fluorophore's region simultaneously within the same extremely short time frame T is determined by Equation 1.14.

$$p_2 = \frac{1}{2}m^2 \tag{1.14}$$

m is small (because we consider an extremely short time frame T) and p_2 is two-photon excitation probability, which depends on the square of the optical power through parameter m. TPE offers an advantage in strongly localised excitation where most of the absorption occurs at the focal plane, leading to better contrast image generation. Moreover, this can reduce damage to the sample as lower photon energy (longer wavelength) is used.

1.1.4 Time and frequency domain measurement

Fluorescence measurement can be classified into two types: steady-state, and time-resolved measurement (Figure 1.8). Steady-state measurement is an intensity-based measurement where the sample is continuously observed and illuminated by a constant beam light source. The excitation and emission profile of the sample is recorded as a function of wavelength (Figure 1.8 (A)). In time-resolved measurement, the sample is exposed by shot pulsed (Figure 1.8 (B)) or modulated laser (Figure 1.8 (C)), and the intensity profile is recorded over time with a high-speed nanoscale timing system.

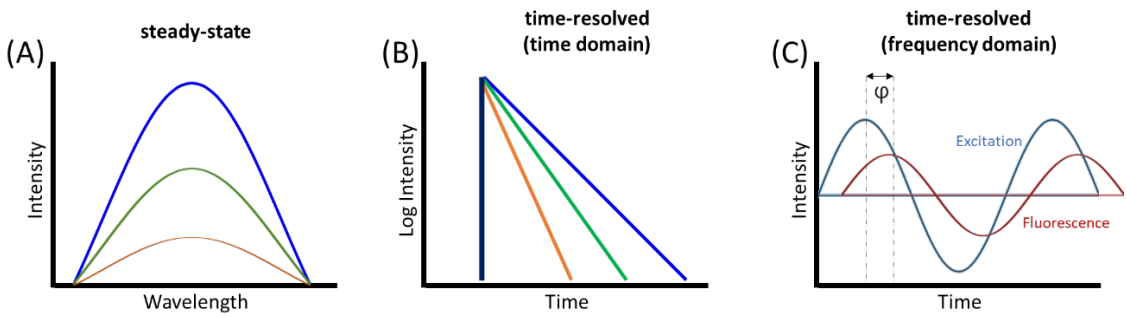

Figure 1.8 (A) steady-state (B) time-resolved measurement (time domain) and (C) time-resolved measurement (frequency domain). The image is adapted from [3]

Frequency-domain measurement is common because it requires minimised hardware and signal processing. The laser is modulated at a frequency of 1 – 100 MHz of a sinusoidal wave, while the fluorescence signal contains the same wave profile with attenuated amplitude and shifted phase due to fluorescence decay kinetics that the fluorophore spends a short time before emission [19]. The measured fluorescence signal contains the same modulation frequency from excitation can be written by Equation 1.15.

$$E(t) = E_0(1 + m_{cm}\sin(\omega t - \phi)) \tag{1.15}$$

where *E(t)* is modulated emission intensity as a function of angular modulation frequency (ω), phase (ϕ) and modulation amplitude (m_{cm}). The fluorescence lifetime can be calculated by Equation 1.16 by using phase delay compared to the excitation signal measured from the side scattering signal.

$$\tau = \frac{\tan \Delta\phi}{\omega} \tag{1.16}$$

where $\Delta\phi$ is phase shift and τ is fluorescence lifetime. The advantage of frequency domain measurement is the speedy performance due to the developed algorithm and uncomplex data processing. However, the drawback is this method needs high signals as the analogue signal is affected by noise. This makes it challenging to resolve small lifetime changes such as FRET.

Time-domain measurement the sample is excited by δ-function excitation, while the fluorescence signal is observed over time by using a single photon counting detector. Then, a histogram of the arrival emitted photon time is reconstructed according to the recorded data. Usually, the fluorescence lifetime is calculated by the fitting method using the single or multi-exponential model and tested by least square analysis [2]. This measurement is typically performed by Time-Correlated Single Photon Counting (TCSPC) system. Further

mathematical detail will be described later in Chapter 2. Time-domain is superior for low signal intensities, offering the ability to resolve complex fluorescence decay of biological samples, thus providing deeper insights into the system under study [20]. For instance, the high temporal resolution of time-domain fluorescence measurement makes it a valuable tool for investigating energy transfer processes, such as FRET, as well as for studying quenching mechanisms. Furthermore, time-domain measurement represents a direct measurement of fluorescence decay, which is of significant advantage as it enables a more straightforward interpretation of the obtained data.

Nevertheless, the disadvantage of this method is its slow speed and requires multiple data processing, especially for the fitting method which is not possible for real-time detection applications. Therefore, several fast and fit-free algorithms and hardware platforms for time-domain measurement have been invented in the last decade [21].

Overall, the choice between time-domain and frequency-domain fluorescence measurement depends on the goals of the experiment and the properties of the sample being studied. Both methods have their advantages and limitations, and both can be valuable tools for studying the fluorescence phenomena.

1.2 Flowcytometry

As flow cytometry is a technology that combines several concepts. It is difficult to estimate a single starting point [22]. It has become a widely utilised method for protein detection within cells through the use of fluorescently labelled antibodies. Due to technological advancements, the current flow cytometer is smaller, more user-friendly, and cost-effective equipment and is widely used in routine clinical practice in hospitals worldwide.

FCM is a technique used to measure the properties of a single cell or a particle as it flows in a fluid suspension across a laser-illuminated area. FCM has served as a powerful tool in high-throughput applications in biomedical research and has been widely used in haematology, immunology, microbiology, and nanoscience applications [1], [23]–[26]. FCM can detect thousands of cells per second and extract information about a desired or pure subpopulation from a heterogeneous mixture allowing more specific analysis. Traditional FCM composes of three main parts as shown in Figure 1.9 where a fluidic system delivers single cells into the flow cell, an optical system for laser illumination and collecting emission signals, and an electronic system for controlling and data acquisition. The suspended cell is hydrodynamically focused to achieve the cell's diameter, typically 10 - 30 μm width, by using a stable two-layer laminar flow (sample and sheath fluid), confirming that all cells pass the laser illumination area in the centre of the flow cell. The optic system records multiple parameters

simultaneously through the optics system in two directions. As shown in Figure 1.10, the parameters that have been detected are represented by the forward scattering (FSC) which serves as an indicator of cell size. The 90-degree direction, indicated by side scatter (SSC) and fluorescence (FL), represents the complexity of the cell and the number of fluorophores present, respectively. Additionally, the fluorescence signal can provide insight into cellular processes and the phenomenon of FRET.

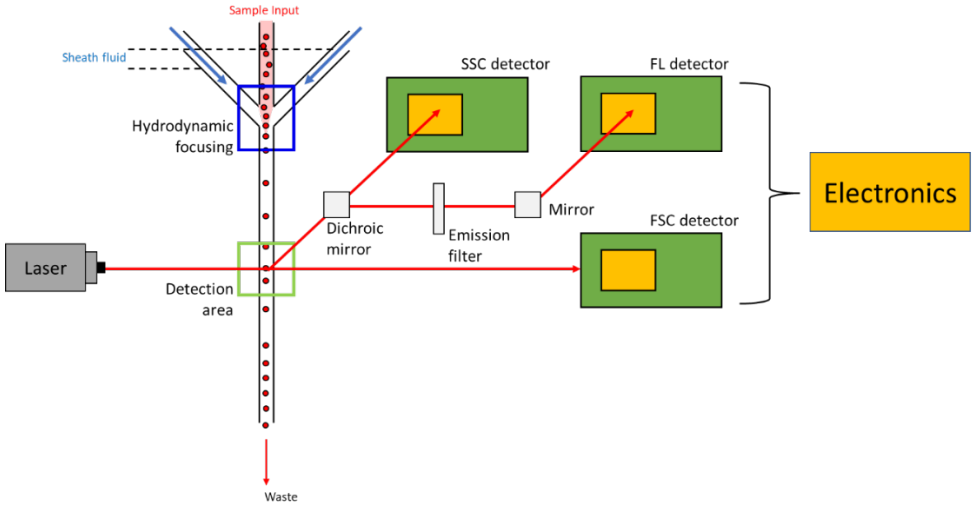

Figure 1.9 A schematic diagram of simple FCM for detecting forward scattering, side scattering and fluorescence intensity and the electronic system controlling data acquisition

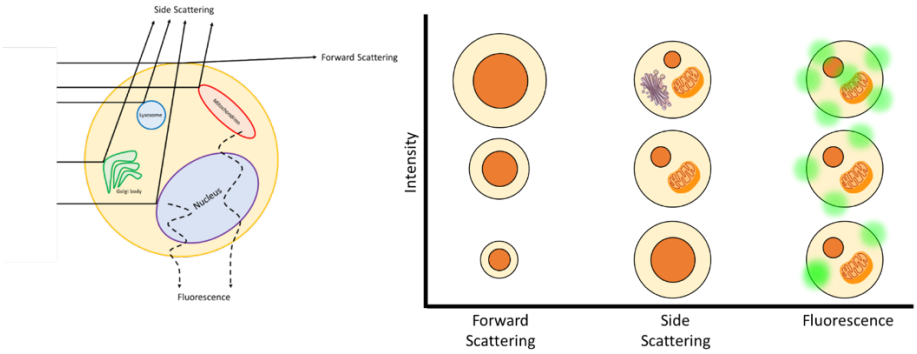

Figure 1.10 Detected parameters in FCM where FSC, SSC and FL are proportional to the cell's size, cell's complexity and amount of fluorophore, respectively. Larger cell sizes lead to higher FSC signals, with complex cells like granulocytes exhibiting higher SSC signals compared to simpler cells such as lymphocytes or monocytes. In fluorescence, the signal is dependent on the quantity of uptake fluorophores.

In contemporary times, flow cytometer systems have become increasingly complicated and costly. These expenses do not include the added expenses associated with the usage of

analysis software, as obtaining a license for each session of usage is mandatory for the administrator. While there are options for free software in flow cytometry analysis, they do not provide the same level of real-time analysis capability as commercial software [27].

The flow cytometer retains several advantages, including the ability to detect multiple parameters in a single measurement, such as scattering, fluorescence intensity, and lifetime. The lifetime measurements offer an advantage in detecting between two fluorophores with closely matched emission wavelengths, which is often challenging when using intensity-based measurements relying on filter selection to isolate the signal. This capability widens the range of selectable fluorophores for improved experimental flexibility. Furthermore, the use of single-cell streaming in flow cytometry allows for the individual measurement of each cell, thus eliminating the potential for bias that may occur during area selection in microscopy. The usage of GNR and deoxyribbonucleic acid (DNA) recognition in FCM has been demonstrated to enable selective mRNA sensing and enhance side scattering intensity in recent studies [28], [29]. This approach is a promising method for biosensing applications.

1.2.1 Time-resolved flow cytometry and its applications

In recent years, the development of FCM faces challenging problems of detection and requires a complex experimental setup. Typically, the fluorescence intensity detection of FCM is limited by the spectral overlap of fluorophores and laser availability [30]. Therefore, the number of labels increases the optical system's complexity and cost. To overcome these problems, the measurement of fluorescence lifetime in FCM had been introduced.

The story of LT-FCM begins in 1992 [31]. The early stage of development is based on frequency-domain measurement with the timing resolution under 200ps, however, the phase-resolved is biased towards short lifetime components [31], [32]. Even with the demodulation process, the lifetime tends toward a longer lifetime [33]. Although the frequency-domain measurement technique offers fast lifetime measurement [20], [34], the researcher still focuses on time-domain measurement due to the excellent resolvability of spectrally overlapped fluorophore, capability of detection for low signal intensities, ability to resolve complex fluorescence decay of biological sample to get deeper information [20], [30], [35]. Although the potential of time-domain FCM has increased since its first appearance, there is a need for real-time analysis and high-throughput cell screening. Moreover, lifetime measurement in flow is still not acceptable routinely because of reduced photon counts due to the short measurement time per particle [30]. Various applications of time-resolved FCM from scientific research and commercial product in the market for biomedical research have been reported in the last decades.

Various studies have been conducted to develop and modify commercial flow cytometer systems to accommodate the measurement of fluorescence lifetime. Faisal et al. have reported a benchtop two-colour channel flow cytometer system for detecting the lifetime shift of autofluorescence of Nicotinamide adenine dinucleotide phosphate (NAD(P)H) from cervical cancer (HeLa) cells with a scan rate of 1,000 cells/sec [36]. The system setup is modified from an assembly of a commercial flow cytometer from Kinetic River Corp equipped with a syringe pump for injecting the sample at 0.05 – 0.5 µl/min and a pressure pump for delivering phosphate buffer saline (PBS) as sheath fluid. The fluorescence signal is collected by a photomultiplier (PMT) (Hamamatsu). However, this system can only perform the frequency-domain measurement and needs to perform static time-domain measurement separately from a TCSPC system.

Wenyan et at. have demonstrated a frequency-domain flow cytometer system modified from a commercial system (FACSVantage^{TM}, BD) to detect the lifetime shift of enhanced green fluorescent protein (EGFP) during bacterial phagocytosis [37]. The excitation source (Vortran) is modulated laser at 25 MHz and the fluorescence signal is collected by two PMTs (Hamamatsu). The cell sample is driven by a pressure pump and the system can detect at the rate of 1,000 cells/sec. The average fluorescence lifetime has been obtained over onboard field programmable gate array (FPGA) processing.

Nedbal et al. have shown the development of a time-domain microfluidic fluorescence lifetime flow cytometer based on an in-house developed microscope to study the FRET efficiency of green and red fluorescent protein (GFP-RFP) pairs [38]. The laser and timing electronic system are based on equipment from Becker & Hickl (B&H) including a pulsed laser at 80 MHz and a PMT card. The fluidics system is based on a T-junction chip (Dolomite Microfluidics, UK) connected with a pressure pump for delivering cells ($3x10^5$ cells/ml). The system can detect up to 3,000 events/min, limited by the dwell time of PMT to collect enough photons for each particle.

Kage et al. have successfully measured time-domain data from fluorescent beads excited by modulated laser by using customed FPGA board to synchronise the timing with PMT [30], [35], [39]. However, the system is limited by PMT integration time and data channel resulting in a few hundred photons per event and not possible to get single-bead information in one measurement. This platform is designed for bead-based sensing of biomolecular interaction.

In a recent study conducted by Ruofan et al., a commercial flow cytometer was modified to incorporate frequency-domain optoelectronics in order to display real-time phasor plots for the purpose of cell counting [40]. The utilisation of the phasor plot method demonstrated an

efficient and practical means of distinguishing fluorescence signals from stained yeast cells based on phasor position. However, the system is limited by its signal processing speed, which restricts real-time processing to a maximum of 1,000 events at a time.

In 2016, Rocca et al. presented a significant advancement in time-domain fluorescence lifetime flow cytometry through the development of a new cell sorting system [41]. This system incorporates fluorescence lifetime measurements to enable real-time fluorescence lifetime-activated actuation for sorting cells. The system achieves a maximum cell throughput of 60,000 cells per second with an error rate of 0.6%. This high throughput is made possible by the single photon avalanche diode (SPAD) sensor's pile-up-resistant embedded centre of mass method (CMM) processor, which allows for low-latency measurement and thresholding of fluorescence lifetime. Although the sensor generates a digital control signal with a latency of only 16.6μs, the samples are measured within 10 ms exposure time, which greatly reduces the detection rate down to 1,000 cells/second and increases the chance of multiple particles appearing in the measurement area.

For commercial development, Kinetic River has presented a time-domain fluorescence lifetime flow cytometer that is capable to measure the multi-exponential of a single cell at a rate of up to 1,500 cells/sec [42] or 10,000 cells/sec with 8 data channels [43]. However, its timing resolution is coarse and not possible to detect a lifetime below 500ps.

1.2.2 Rapid fluorescence lifetime analysis in the flow cytometer

The interest in obtaining fluorescence lifetime in the flow cytometer is growing rapidly due to the potential of rare event detection observed by the lifetime. The circulating tumour cells (CTCs) have been reported that the average number of the CTCs presented in blood is 203 cells/ml and 20 cells/ml for ovarian and prostate cancer, respectively [44]. Therefore, the developing techniques are advancing towards faster and more reliable lifetime estimation methods in FCM. However, the accuracy and maximum speed are affected by some factors including the number of photons, analysis algorithm, and hardware specification. In order to determine the real-time fluorescence lifetime of flowing cells, the lifetime estimation method must be fast, reliable and require a low number of photons.

For hardware limitations, the current time-resolved FCM uses PMT with the TCSPC system and associated software to generate the decay profile. TCSPC is a precise electronic stopwatch equipped with a time-to-amplitude converter (TAC) and analogue-to-digital converter (ADC) that converts time between start-stop signal into the amplitude of an analogue signal, and then into digital data. This configuration has high timing resolution and the instrument response function IRF width can be as small as 2.6 ± 0.2 ps [45]. Although

TAC-ADC delivers exceptional precision, time to digital converter (TDC) can outperform in terms of recording speed. TDC is an electrical circuit that uses a chain of logic gates to determine the time that delivers IRF width of 20ps [21]. PMT is suffered from a long integration time to collect enough photons for lifetime estimation and detects the low number of photons due to limited data channels [30]. Photon throughput of PMT is also limited by the pile-up effect, which sets the detection rate at a low level. When the detector detects a photon, the TCSPC spend some time processing each photon. During this time called dead time, no other photons are being recorded which can lead to photon counting loss. Due to the advancement of complementary metal oxide semiconductor (CMOS) manufacturing, The TDC has been successfully implemented in a pixel of a single photon avalanche diode (SPAD) array and this greatly broadens photon bandwidth allowing the detection of multiple photons in each measurement (or each laser pulse). Recently, the SPAD array with 252x144 pixels shared 1,728 TDC [46] and 192x128 with TDC in each pixel [47].

The effectiveness of the algorithm for lifetime estimation is also necessary for real-time measurement applications. Traditional fluorescence lifetime calculation is based on the curve-fitting method that resolves the exponential coefficient and fluorescence lifetime from the deconvolution process and the fitted mathematical model is tested by least square analysis to determine parameters of the model with the highest probability of being correct [2], [3]. However, this approach is time-consuming, not possible for real-time application, and can have errors in the case when photon numbers are low, and the results depend on the user's initial configuration for calculation such as decay model, shift value, estimated lifetime and background. In the FCM application, the analysis goal is reliable and automatic rapid analysis. The time-consuming analysis can lead to increased system dead time, which can boost the chance of miscounted particles. Various fast and fit-free lifetime analyses, for determining lifetime value or illustrating the lifetime population of the sample, have been purposed in the last few decades as listed below.

(1) Mean photon arrival time calculation is a fast and simple method that estimates the lifetime by averaging the arrival time of every photon in the fluorescence decay without fitting processes [48]. However, this method is sensitive to noise and needs entire fluorescence decay, which makes this method accurate in short-lifetime regions. The mean arrival time can be expressed by Equation 1.17 below.

$$\tau_{mean} = \frac{1}{N}\sum tn(t) \tag{1.17}$$

where N is the total number of photons, t is the time corresponding to each channel and $n(t)$ is the corresponding photon number in each time channel.

(2) Phasor approach, developed by Digman in 2008 [49], represents a significant advancement in the analysis of fluorescence lifetime data. This technique offers a unique and powerful way to simplify the often-complicated task of interpreting fluorescence decays by using sine and cosine transform of the decay data into phasor coordinates, comprising the real (Re) and imaginary (Im) components, respectively. A detailed exploration of the mathematical explanation behind the phasor approach is given in Chapter 2. The resulting phasor plots is a visualisation for approximating fluorescence lifetime and energy transfer processes. Short-lifetime components tend to cluster in the bottom right corner of the phasor plot, while long-lifetime components locate in the bottom left corner. Furthermore, the phasor approach enables the estimation of the fluorescence model. Points on the semi-circle line of the phasor plot correspond to single exponential decay fluorescence, whereas points inside the semi-circle indicate multi-exponential decay. This means that not only can researchers estimate the lifetime and identify different fluorescence components, but they can also deduce the decay kinetics (Figure 1.11).

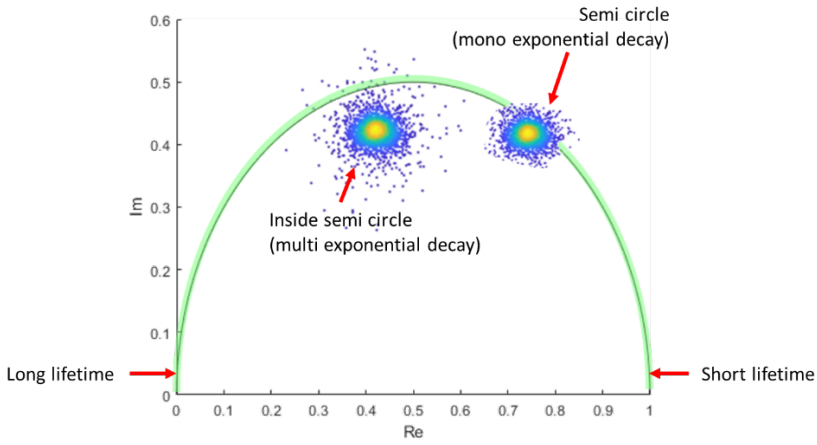

Figure 1.11 Illustration of phasor plot where fluorescence decay locates on the semicircle, while multi-exponential decay appears inside the semicircle. Along the semi-circle, the short lifetime occurs on the right side and the long lifetime occurs on the right side.

(3) rapid lifetime determination method is a rapid method that calculates lifetime from photon counts in two time-gate windows. This calculation has speedy performance; however, the drawback is limited accuracy, precision and narrow lifetime range [50]. This algorithm calculates lifetime by using Equation 1.18.

$$\tau_{rapid} = \frac{\Delta t}{\ln\left(\frac{I_1}{I_2}\right)} \quad (1.18)$$

where Δt is the width of the window to be analysed, I_1 and I_2 are integrated intensities in the time window.

(4) The τ_A/τ_I method, developed by Yahui et al., is a novel technique for analysing the multi-exponential nature of fluorescence decay data [51]. This method involves comparing intensity-weighted and amplitude-weighted lifetime measurements in order to gain more understanding of the fluorescence decay process. This approach represents a significant advancement in the field of fluorescence analysis. This method has been used to quickly investigate the intracellular location of bacteria [52].

(5) CMM represents a powerful and versatile tool for fluorescence lifetime analysis in various applications. The CMM algorithm is a highly efficient, hardware-friendly and fit-free method for obtaining intensity-weighted fluorescence lifetime information for real-time applications [53], [54]. This approach has been demonstrated to be effective in both calibrated [55] and non-calibrated IRF [56], and with or without background subtraction. CMM is able to process fluorescence lifetime imaging microscopy (FLIM) data with a speed that is unsurpassed by other methods, taking only 0.2 seconds to calculate 150 x 150 pixels with 256 bins [50]. Additionally, the lifetime approximation process can be further enhanced by the use of pre-calculated look-up tables or pattern recognition techniques.

1.3 Thesis Motivation

The FLACS platform developed in this study is a game-changer for biomedical research and clinical application. Our system has been designed with a compact setup and user-friendly interface, utilising commercially available optical and fluidic components to significantly reduce costs for both components and daily operation. This means that our system can be used more widely, benefiting researchers and clinicians who previously may not have had access to such technology.

Our system specifically targets RNA present in the cytoplasm, which plays an important role in regulating the cell cycle process. Over-expression of genes can lead to the generation of tumours, for example, Myelocytomatosis oncogene (C-Myc) has been found in over 40% of all human cancers, making our system a vital tool in the fight against cancer [57]. By designing a high-throughput FCM capable of measuring the lifetimes of flowing cells individually, cancerous and non-cancerous cells can be distinguished using the nanoprobe.

This will revolutionise cancer research and diagnosis, leading to better treatments and outcomes for patients.

While there are currently time-resolved flow cytometers on the market, most are based on frequency-domain measurement with detection rates up to 1,000 cells/sec [36], [37], [40]. The few time-domain FCMs that do exist have low throughput or low timing resolution [38], [41]. The system in this thesis is different, being a high-throughput time-domain FCM capable of rapid lifetime analysis. A prototype of a time-domain fluorescence lifetime flow cytometry platform is assembled on a compact wide-field microscope setup to measure the fluorescence lifetime of flowing fluorescent beads and cells loaded with fluorophores or nanoparticles. This system, known as reliable, low-cost, and compact FLACS, has the potential to make a significant impact on biomedical research and clinical applications.

To achieve the goals, a 192x128 TCSPC SPAD array has been calibrated and configured to a single pixel with 24,576 data channels to increase photon bandwidth. This pixel integration, as known as the megapixel technique, collects the incoming photon timestamp of every pixel and generates a fluorescence decay. This enables photon pile-up-free measurement [58]. CMM and phasor plot have been chosen as the real-time analysis tool due to their ability to resolve lifetime rapidly with good accuracy and promising capability to differentiate lifetime population. Furthermore, the CMM require a minimum of 200 photons for calculation, which is much lower compared to the 1,000 photons required for the fitting method and 300 photons for maximum likelihood estimation [21]. The developed analysis software has a graphical user interface (GUI) which is user-friendly, and responsive and does not require an experienced user for proper measurement.

The later chapters of this thesis describe the development processes of the platform. The prototype has been designed, constructed and characterised with an effort to enhance its accuracy and reliability for biomedical research and clinical application. This system has shown the capability of differentiating flowing particles/cells of different fluorescence lifetimes, suggesting a potential for cancer research and diagnosis, leading to better treatments and outcomes for patients.

Chapter 2 Experimental Methodology

Fluorescence spectroscopy is a powerful analytical technique widely employed in various scientific fields, including chemistry, biology, and materials science. In this chapter, we will delve into the fundamental concepts of fluorescence measurements, ranging from ultraviolet-visible (UV-Vis) spectroscopy and steady-state measurements to advanced time-resolved fluorescence spectroscopy. Furthermore, visualization techniques will be explored, such as confocal and lifetime imaging. Lastly, the chapter will conclude by introducing rapid time-resolved fluorescence analysis techniques, including the centre of mass method (CMM) and phasor plots in its last section.

2.1 Ultraviolet-visible Spectroscopy

UV-Vis spectroscopy is a relative measurement technique that measures excitation including absorption and scattering of a sample compared with a reference solution. In this study, the extinction spectrum of samples is investigated by a Perkin Elmer Lambda 2 spectrometer. Figure 2.1 shows the diagram of the typical setup of a UV-Vis spectrometer. The sample and reference are filled in a cuvette and placed in sample chambers in the spectrometer. The spectrometer typically equips with two light sources providing a broad range of excitation from a deuterium lamp (190 – 350nm) and a halogen lamp (300 – 1100nm) that produce a light beam to the sample. The excitation wavelength is precisely selected through a monochromator. Two detectors detect the light beam that either passes through or is absorbed by the sample or reference measuring how much light has been absorbed compared to the reference. This information is used to produce an absorbance spectrum as a function of wavelength, expressed by Equation 2.1.

$$A = \log\left(\frac{I_0}{I}\right) \tag{2.1}$$

where A is absorbance, I_0 and I are light intensity passes through the reference and sample channel, respectively. The absorbance spectrum is a valuable tool to determine the concentration of a substance in the sample, which is beneficial for purity and contamination testing, and nanoparticle study [14]. Beer-Lambert has described that the absorbance proportionally relates to the concentration described by Equation 2.2 (Beer-Lambert Law).

$$A(\lambda) = \epsilon(\lambda)cl \tag{2.2}$$

where ϵ is the molar extinction coefficient describing the ability of a substance to absorb light at a specific wavelength, c is concentration and l is the optical path length.

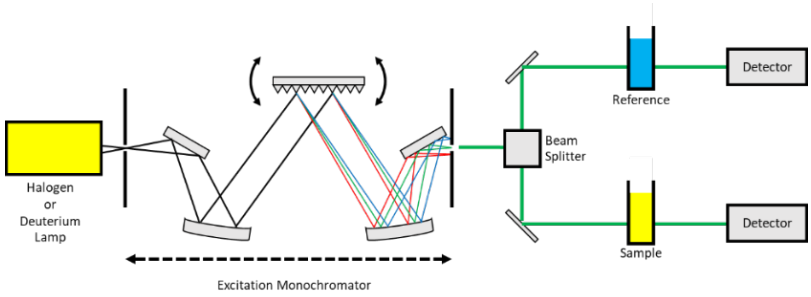

Figure 2.1 A schematic diagram of the typical setup of a UV-Vis spectrometer

2.2 Steady-state Fluorescence Spectroscopy

Steady-state fluorescence spectroscopy is a technique that uses a light beam to excite a substrate at the desired wavelength, and measures emitted light then plotted as a function of wavelength. In this study, the fluorescence emission spectra are obtained by Fluorolog-3 spectrofluorometer (Horiba, UK). Figure 2.2 shows the instrument equipped with a broad wavelength xenon lamp to generate a light beam that passes through a monochromator to select excitation wavelength. After the sample has been excited and emits the fluorescence, the emission is collected at 90° compared to the excitation channel through a monochromator. The emission intensity is then recorded as a function of wavelength and calibrated with excitation intensity and dark counts.

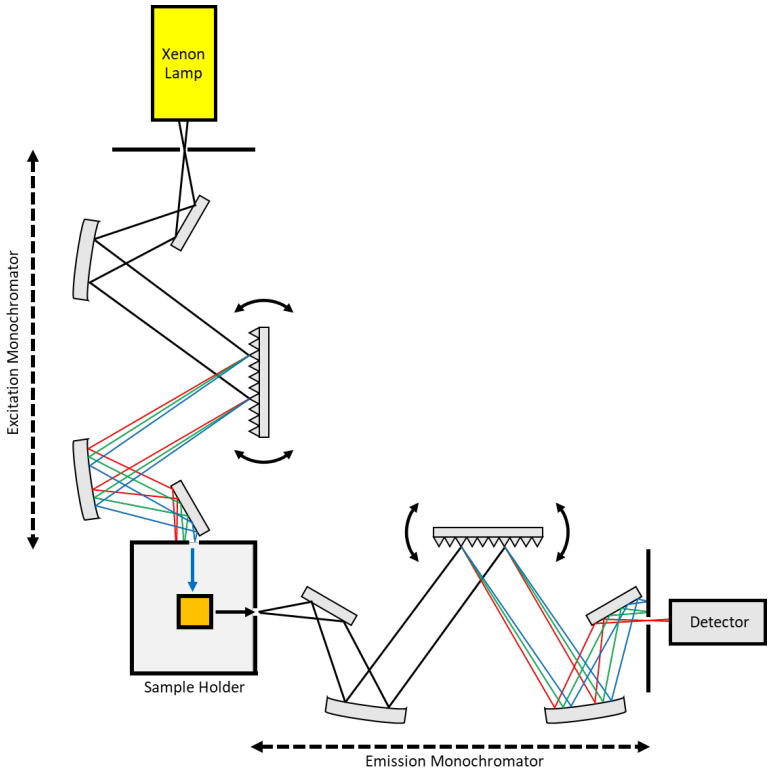

Figure 2.2 Schematic diagram of a fluorescence spectrometer

2.3 Time-resolved Fluorescence Spectroscopy

Time-resolved fluorescence spectroscopy is a technique used to measure the time that molecule stays in the excited state, known as fluorescence lifetime. This technique has been used to study ultrafast phenomena such as chemical reactions, protein folding and monitoring biological dynamics to provide additional information apart from intensity-based measurement, which is affected by photobleaching. In this study, the time-domain measurement is performed in the Horiba DeltaFlex fluorescence lifetime spectrometer system (Horiba, UK) (Figure 2.3). The sample is illuminated by a pulsed laser beam at a specific wavelength, and the fluorescence signal is recorded as a function of time by a photomultiplier, through a long-pass emission filter and a polariser. The polariser is set to a magic angle of 54.7° to avoid the signal from depolarised effect from molecular rotation leading to difficulty in data analysis [59]. The measurement configuration is controlled through DataStation software (Horiba, UK) on a PC.

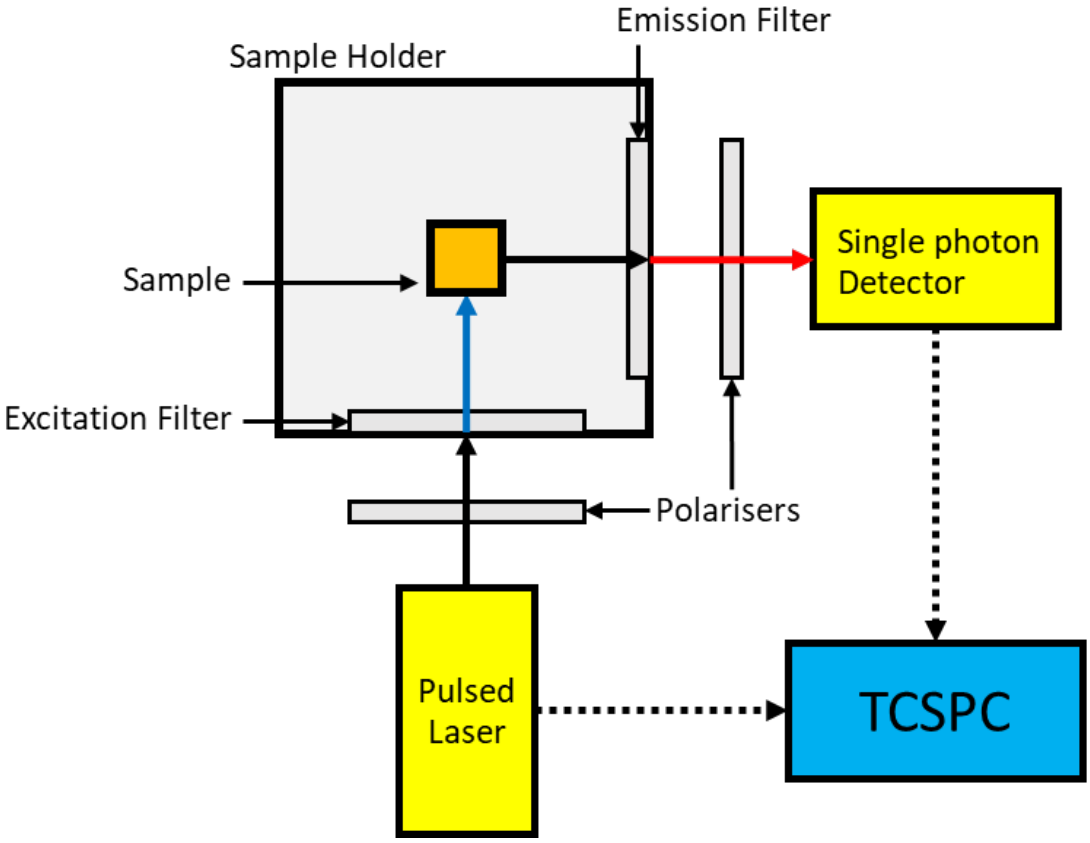

Figure 2.3 Schematic diagram of a time-resolved fluorescence spectrometer

2.3.1 Time correlated single photon counting

Time-domain measurement relies on TCSPC which is a technique to measure the time-resolved intensity of light allowing to measure of the arrival time of a single photon on a nanosecond scale with sub-nanosecond resolution and reconstructing the collected data into a histogram of intensity against the arrival time. This instrument requires a high repetition rate mode-lock laser and a very sensitive photon detector such as a PMT or SPAD. TCSPC is the most popular method in pulse fluorometry as it has promising advantages such as single-photon sensitivity, known statistics (Poisson) and low distortion caused by amplitude variation as it is using digital circuit [2].

TCSPC is a rapid stopwatch that works in the cycle between the start and stops trigger signal provided by the laser controller and detector, respectively. The measurement starts with the generation of the excitation pulse to excite the sample and send a sync signal as a start signal. When the signal arrives at a TAC it generates a voltage slope which increases linearly over time on the nanosecond timescale. When the second signal that comes from the detected photon from the detector arrives at the TAC, the voltage slope stops. After the stop signal, the TAC contains a data set of voltage which is proportional to the time delay between two inputs (excitation and emission). Both signals are passed through a constant function discriminator (CFD) which precisely determines the arrival time and reduces miscounted events caused by noise. The recorded data in TAC is amplified by a programmable gain amplifier (PGA) and then convert to a readable numerical value by using an ADC to minimise the wrong readings, a window discriminator (WD) is used to restrict the voltage in the given range. The converted voltage from the single photon is stored, as a single event in a time bin. A histogram of the decay curve is constructed by repeating the process many times (Figure 2.4).

The electronic response is also an important factor. The TCSPC detects only the first arriving photon and is followed by a resting time in the range of a hundred nanoseconds to 10 microseconds. During this period of time, called “dead time”, the system cannot detect the new incoming photons, and the dead time is much longer than the fluorescence decay. For the excitation source with a very high repetition rate, the TAC can constantly be in rest mode. Detecting several photons in one working cycle would cause distortion to the decay leading to a shorter lifetime or pile-up effect. To avoid dead time, the laser power needs to be adjusted keeping the detector count rate below 2% of the laser repetition rate and reverse mode TCSPC is required in a practical setup. The reverse mode is the normal TCSPC process, as described above, but uses the emission pulse as the start signal and the excitation pulse as the stop signal. This allows for the measurement of the distribution of fluorescence rise times, rather than

fluorescence decay times, and the system only faces the dead time only photon event instead of every excitation pulse. The recorded data is then flipped by software to make it like the normal forward mode.

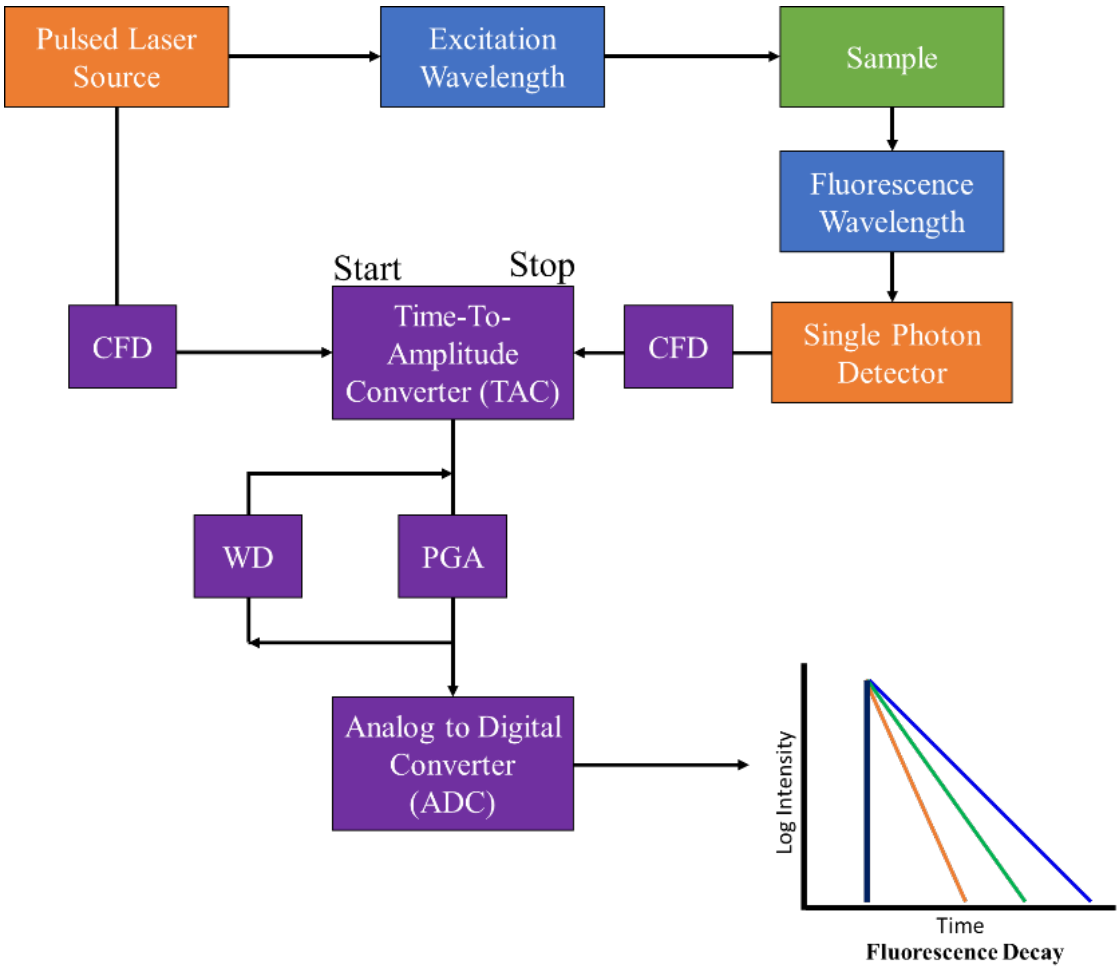

Figure 2.4 Diagram of TCSPC process used for reconstructing fluorescence decays. The laser pulse triggers timing electronic, which then stops by a stop signal from the detector. The measured time is converted and stored as an intensity histogram against photon arrival time. CFD is a constant function discriminator, PGA is the programmable gain amplifier and WD is the window discriminator. The image is adapted from [3]

Apart from fluorescence decay, the instrument response function (IRF) is also needed for the lifetime estimation process. IRF is the measurement of the shortest profile measurable by the system or sample with zero lifetime, which represents the response from the system. In an ideal TCSPC system, the IRF resemble a δ-function, however, the width is broadened due to the characteristic of the excitation source, detector, and electronics. In this study, the IRF is

obtained from scattering signal at 90° of diluted LUDOX AS-40 colloidal silica solution (Sigma-Aldrich) through a natural density filter and polariser at 0°.

2.3.2 Least square fitting analysis

Since the IRF is not a perfect δ-function in practice but has a width of 0.5 to 2 ns, extracting information involves considering the excitation pulse as a series of δ-functions with different amplitudes starting at different delay times [3]. The measured fluorescence intensity decay is the sum of all these exponential decays resulting from the convolution of the impulse response and the IRF. This convolution can be described by Equation 2.3.

$$F(t) = \int_0^t P(t')i(t-t')dt' = P(t) \otimes i(t) \tag{2.3}$$

where *F(t)* is measured fluorescence intensity at time *t*, *P(t)* is IRF, *i(t)* is fluorescence impulse response, and *t'* is moving time delay corresponding to the series of δ- function and $\otimes$ means convolution.

The fluorescence lifetime is determined by the deconvolution process on the measured fluorescence decay. This process is an iterative process by selecting the mathematical model to be convoluted with recorded IRF and comparing it with recorded IRF and repeating until the model has achieved the minimum difference between calculated and measured parameters [3], [59] (Figure 2.5). Typically, the fluorescence decay model is described by exponential decay as Equation 2.4 [60].

$$i(t) = A + B_1 exp\left(-\frac{t}{\tau_1}\right) + B_2 exp\left(-\frac{t}{\tau_2}\right) + \cdots + B_n exp\left(-\frac{t}{\tau_n}\right) \tag{2.4}$$

where *n* is the required number of lifetime components, which is corresponding to the number of fluorophore species presented in the sample, *A* is background offset, *B* is the relative intensity of a given lifetime component. Solving this inverse problem to obtain the amplitude and lifetime components, however, is time-consuming and can be prone to errors and artefacts, especially when the photon count is low [61].

The goodness of fitting of the model is determined by the chi-square (χ^2) value via non-linear least square analysis (NLLS) (Equation 2.5).

$$\chi^2 = \sum_N \frac{\left(Y(i)-F_d(i)\right)^2}{\sigma(i)^2} \tag{2.5}$$

where *i* is the time channel, *Y(i)* is the measured data, $F_d(i)$ is the calculated value from the model, $(Y(i)- F_d(i))$ represents the deviation of the model from the measured data and *σ(i)* is the standard deviation. The χ^2 value of *1* is obtained from the most possible ideal model,

however, it is practically accepted that the value of $0.9 < \chi^2 < 1.2$ is considered a good fit [62]. Moreover, TCSPC is described by Poisson distribution where only one photon is detected in one working cycle. This allows us to directly determine the standard distribution as $\sigma = \sqrt{N(i)}$, where N is the number of detected photons if there is no systematic error and the uncertainty is only from counting statistics.

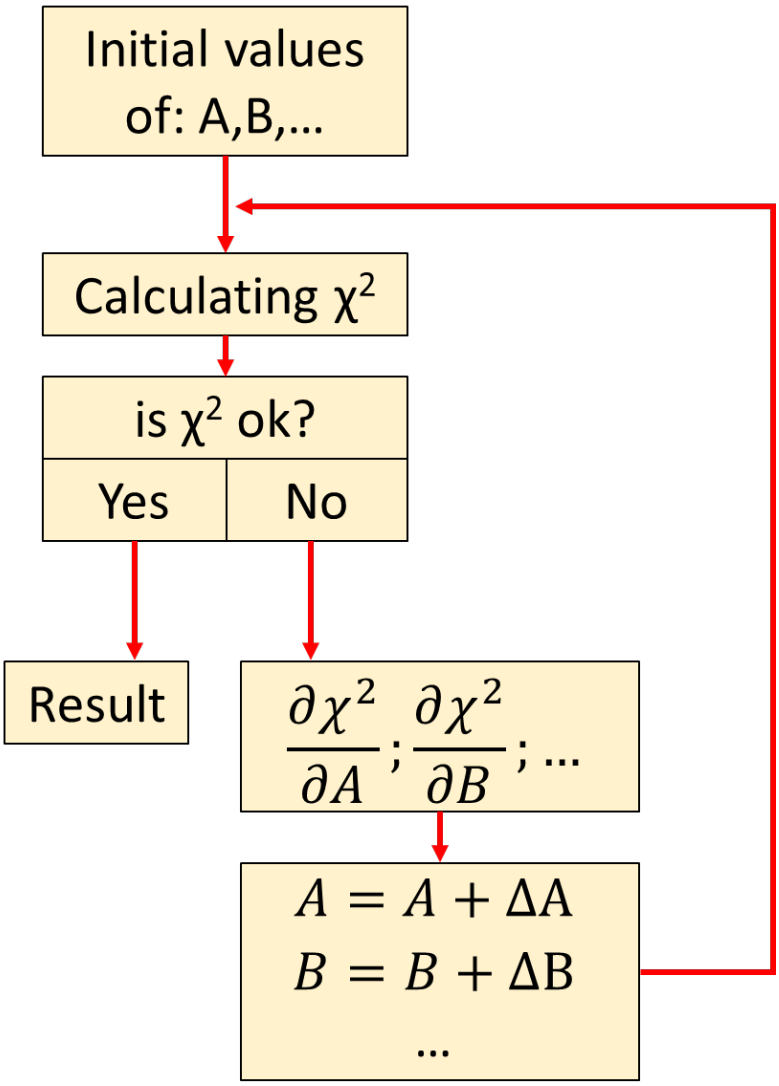

Figure 2.5 Block diagram showing least-square fitting process.

Another parameter to indicate the goodness of fitting is weighted residual, which compares the mismatch area between the fitted model and measured data [60]. This method provides information on fitting quality. Good fits should show randomly distributed residuals centred at zero, while non-random residuals can indicate the requirement of additional or fewer

exponential components. The residual is calculated for every single data channel by Equation 2.6, where W_t is the weighted residual.

$$W_t = \frac{Y(i) - F_d(i)}{\sigma(i)} \tag{2.6}$$

In this study, the least square fitting analysis mentioned above is performed in DAS6 software (Horiba, UK) as shown in Figure 2.6. The error value for each lifetime component is determined through the standard deviation obtained from the fitting results provided by the software.

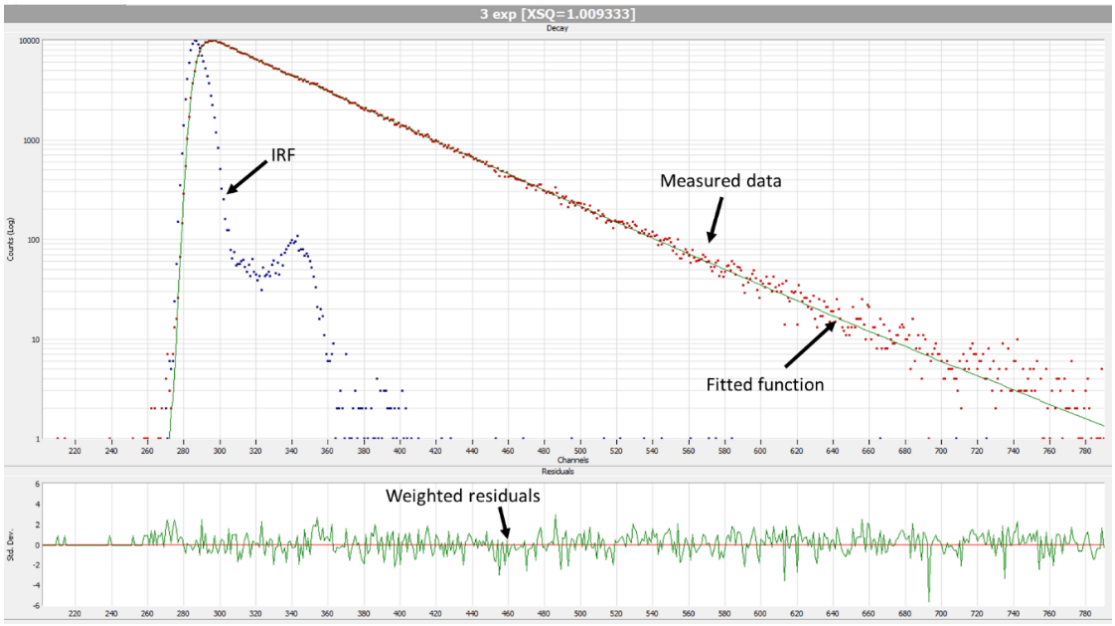

Figure 2.6 Screenshot of the DAS6 software showing the fluorescence decay of RNA nanoprobe hybridised with cDNA (red dot) with IRF (blue dot) and the three-exponential fitted model (green line). In the upper plot, Y-axis is intensity (counts), while the x-axis is time (bin) with 26 ps bin width. The lower plot shows a weighted residual indicating a good fit with $\chi^2 \approx 1.01$.

2.4 Confocal Fluorescence imaging microscopy

Nowadays, the conventional fluorescence microscope has been used in several field research especially in biological science as a non-invasive and non-destructive technique. The microscope comprises a dichroic mirror and emission filter which reflect the excitation light but transmit the fluorescence signal. The sample is illuminated by the excitation light through the objective lens, then the emitted fluorescence signal can pass through to the detector. Besides the conventional microscope, the confocal microscope uses an adjustable aperture to reject out-of-focus light and see only the signal from the focus plane, resulting in an image of

the out-of-focus plane that is significantly attenuated compared to the image from the focal plane. Although the entire sample is illuminated, the highest excitation and emission are found at the focal point. Figure 2.7 shows a diagram of a confocal microscope where the dashed green rays represent light from the out-of-focus plane, while red rays are the emission from the focal plane which can travel to the detector. Moreover, confocal microscopy allows cross-section imaging of cells with high resolution, which can be reconstructed into 3D images or stacked images from several z-axis positions of the focal plane.

In this study, fluorescence intensity imaging is performed on a laser scanning confocal microscope (LSM510, Zeiss) equipped with Argon laser (458, 477, 488 and 514nm) and HeNe (543nm) for one-photon excitation, while Chameleon Ultra (690 – 1020nm) for two-photon excitation. The sample is pixelised and scanned all over the x and y direction in the focal plane. The system contains selections of dichroic mirrors, filters, and two detectors allowing to performance of two-colour fluorescence intensity imaging (Figure 2.8).

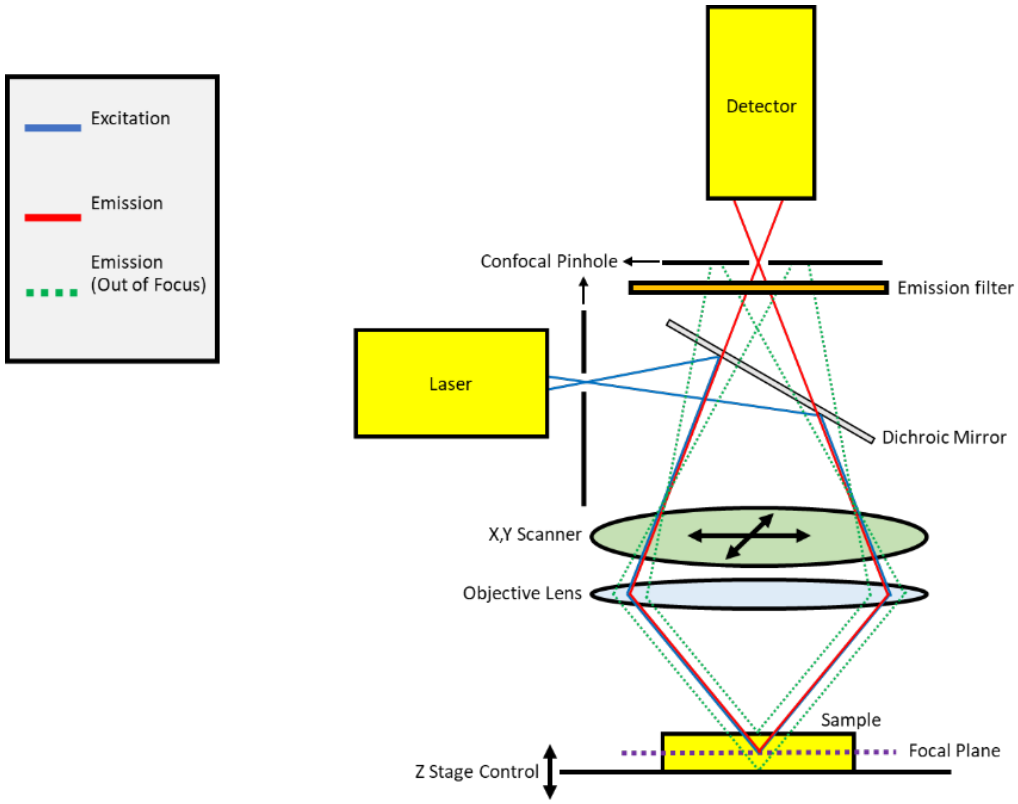

Figure 2.7 Schematic diagram of a confocal microscope. The laser excitation is focused to a specific pixel in a desired focal plane (blue ray), while the optical system passes the in-focus emission (red ray) to the detector and blocks the out-of-focus emission (green dash) by the pinhole. This process repeats pixel by pixel to construct the image.

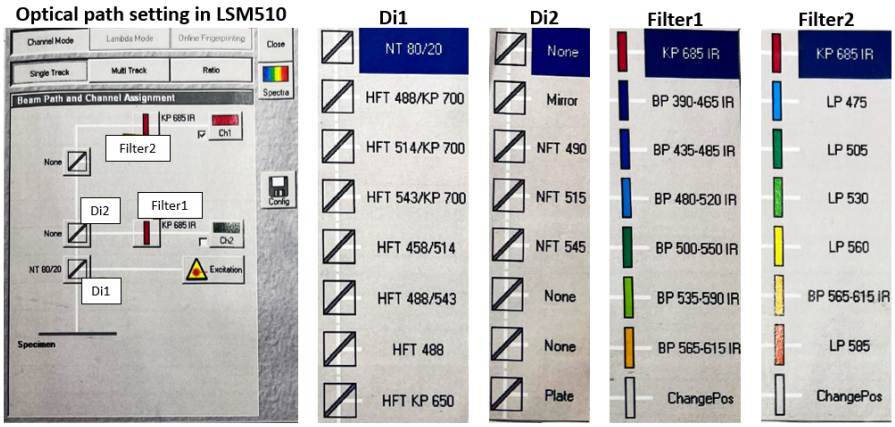

Figure 2.8 Optical path configuration in the LSM510 software showing available dichroic mirrors and filters. Di1 is an excitation dichroic mirror, which directs the laser to the sample and collects fluorescence emission. Di2 is another dichroic mirror that can reflect some wavelength to detector 2 (Ch2). Filter1 and Filter2 are emission filters for detectors 1 and 2 (Ch1 and Ch2).

2.5 Fluorescence lifetime imaging microscopy

FLIM is another powerful fluorescence lifetime-based technique that utilises the advantage of lifetime measurement and has been used to study biological samples. FLIM technique can be divided into two categories; (1) confocal scanning FLIM where the sample is allocated into pixels and then illuminated by either single- or multi-photon excitation, and scanned pixel by pixel, and (2) wide-field FLIM is camera-based FLIM where the whole sample is excited, and the image is reconstructed by multi-pixel sensor based on charge-coupled device (CCD) or CMOS technology [47]. Each pixel is FLIM and contains fluorescence lifetime data indicated by coded colour.

2.5.1 Scanning two-photon excitation Fluorescence lifetime imaging microscopy

The TCSPC system is also used in scanning FLIM system. As the scanning head moves pixel by pixel across the scanning area to deliver an excitation pulse, the fluorescence signal is continuously collected by the PMT during dwell time. The measurement is repeated numerous times (≈ 100 times) to construct the fluorescence decay, collecting a sufficient number of photons per pixel for the least square-fitting lifetime analysis mentioned earlier in this thesis. The lifetime of each pixel is represented by a colour map, indicating the lifetime differences between pixels.

In this study, the scanning FLIM is performed on a modified LSM510 system with a TCSPC card (SPC-830, B&H). The sample is excited by a tuneable femtosecond Ti:Sapphire laser

(Chameleon, Coherent) as a two-photon excitation source to reduce cellular damage. The repetition rate is 80 MHz with an illuminating duration of less than 200 fs. The emitted photons are collected through a 63x water-immersion objective lens (N.A. = 1.0) and transferred into a photomultiplier (DCC-100, B&H) detector. This system must be operating in absolute darkness. Figure 2.9 shows a diagram of the FLIM system used in this study.

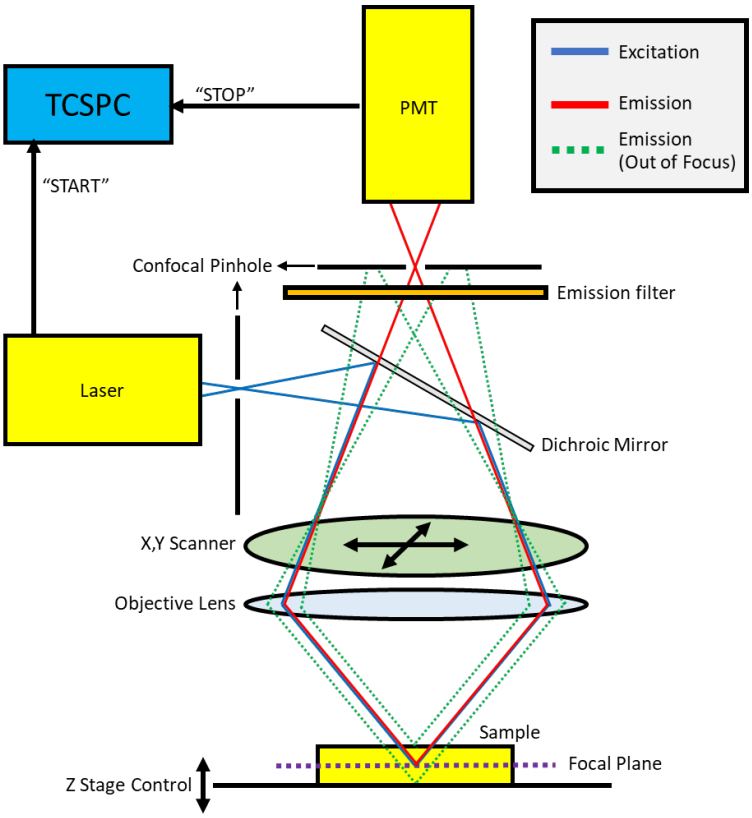

Figure 2.9 Schematic diagram of scanning fluorescence lifetime imaging microscopy. The laser excitation is focused on a specific pixel in a desired focal plane (blue ray), while the optical system passes the in-focus emission (red ray) to the detector and blocks the out-of-focus emission (green dash) by the pinhole. The start signal is simultaneously generated with the laser pulse and the stop signal is from the detected signal photon. This scanning repeats pixel by pixel to collect enough photons for the lifetime analysis of each pixel.

2.6 Fast and fit-free time-resolved fluorescence analysis

The fast and reliable method calculation process is required in a specific application such as lifetime-based flow cytometry for detecting fast-moving cells [1] and dynamic FLIM for detecting organelles in a live cell, cellular metabolism, and protein interaction [21]. For common methods such as least square or maximum like hood estimation, the remaining challenges are slow lifetime calculation and impossible for real-time data analysis. This

analysing involves multiple processes, which is time-consuming and users need to select a suitable decay model. Therefore, various fast and fit-free fluorescence lifetime analyses have been developed to be used in FLIM imaging [21]. In this study, the lifetime data is detected and displayed in real-time, therefore the data transferring, and calculation time is also included as the dead time before the system collects the new arrival photon. Two rapid lifetime analyses: CMM and phasor method have been adapted for FCM data and used in this study because they have been recently proven their speedy performance [53], [54], [63], [64] and ability to resolve the lifetime even with low photon counts [21].

2.6.1 Centre of mass method

The CMM is a new and simple method for fast fluorescence lifetime calculation [54]. The CMM improves speed by directly calculating the lifetime from the collected photons without choosing the lifetime model; moreover, it provides real-time lifetime and intensity that benefit rare event detection in FCM applications. In addition, this method had been implemented in an FPGA processor equipped with a SPAD showing the possibility of on-chip processing, which can further improve the photon collecting rate [41].

The term "centre of mass" of CMM comes from the calculation process, which is similar to the centre of mass in mechanic physics. For a linear object with a continuous mass density $f(r)$ and total mass M_T (Figure 2.10), the centre of mass (CM) is defined by Equation 2.7.

$$CM = \frac{\int rf(r)dl}{\int f(r)dl} = \frac{\int rf(r)dl}{M_T} \tag{2.7}$$

If the mass density of the linear object length T distributes as a single-exponential decay function with fluorescence lifetime τ in the range $0 \leq t \leq T$ along the x-axis (Figure 2.10). The mass equation can be written as $f(t) = Aexp(-t/\tau)$. Therefore, Equation 2.7 can be rewritten as Equation 2.8.

$$CM = \frac{\int_0^T tf(t)dt}{\int_0^T f(t)dt} = \frac{\int_0^T t(Ae^{-\frac{t}{\tau}})dt}{\int_0^T (Ae^{-\frac{t}{\tau}})dt} \tag{2.8}$$

where the denominator is the total photon count, while the numerator is the information of total photon events. Both can be calculated separately as below:

$$\int_0^T tf(t)dt = A\tau^2\left(1 - e^{-\frac{T}{\tau}}\right) - A\tau Te^{-\frac{T}{\tau}}$$

$$\int_0^T f(t)dt = A\tau\left(1 - e^{-\frac{T}{\tau}}\right)$$

These integrals can be put in Equation 2.8, thus the equation can be written as Equation 2.9

$$CM = \frac{A\tau^2\left(1 - e^{-\frac{T}{\tau}}\right) - A\tau T e^{-\frac{T}{\tau}}}{A\tau\left(1 - e^{-\frac{T}{\tau}}\right)} = \tau - \frac{Te^{-\frac{T}{\tau}}}{1 - e^{-\frac{T}{\tau}}} \tag{2.9}$$

From the right side of Equation 2.9, the second term can be neglected when $T > 7\tau$ and the CM located at distance τ in the x-axis can be estimated as the lifetime *(CM ≈ τ)*. Furthermore, in the case of $4\tau < T < 7\tau$, the second term is pre-calculated and stored in a look-up-table (LUT), which can still map the *CM* to the lifetime rapidly [53].

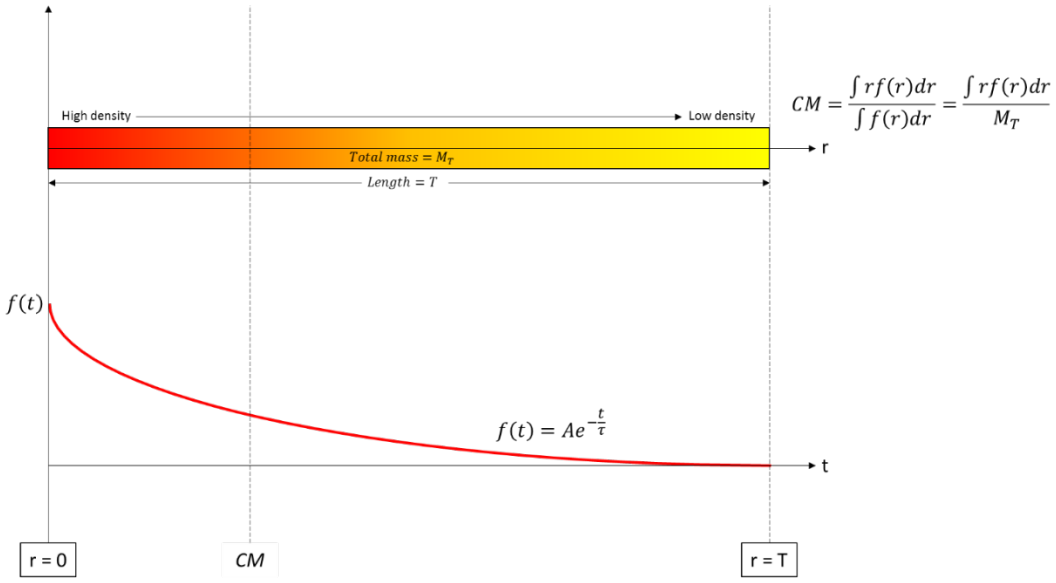

Figure 2.10 Centre of mass of a linear object with mass density function of single-exponential decay

The CMM has been mathematically well proven, however, due to timing electronic, the arrival time of photon events is not a continuous function and is quantised by binning process into M time bins with bin width h (Figure 2.11). Therefore, lifetime calculation in the hardware or MATLAB is a discrete integral process and the calculated lifetime is equal to the fitting method when *M* is close to infinity [53]. Therefore, Equation 2.8 can be rewritten as the sum of many integrals in each time bin, as shown in Equation 2.10.

$$\tau = \frac{\int_{t_0}^{t_1}\left(\frac{t_0 + t_1}{2} - t_0\right) f(t)dt + \cdots + \int_{t_{M-1}}^{t_M}\left(\frac{t_{M-1} + t_M}{2} - t_0\right) f(t)dt}{\int_{t_0}^{t_M} Ae^{-\frac{t}{\tau}}dt} \tag{2.10}$$

Equation 2.10 can be simplified in the summation form as Equation 2.11

$$\tau = \frac{\sum_{j=0}^{M-1} \Delta t_j \int_{t_j}^{t_{j+1}} f(t)dt}{N_c} = \left(\frac{\sum_{j=0}^{M-1} jN_j}{N_c} + \frac{1}{2}\right) h = Rh \tag{2.11}$$

where $t_j = jh$, and $\Delta t_j = t_j - t_0 + \frac{h}{2}$ and N_j is the number of recorded photons in the j^{th} time bin ($N_j = \int_j^{j+1} f(t)dt, j = 0, 1, 2, 3, \ldots, M\text{-}1$), and N_c is total photons ($N_c \int_0^T f(t)dt$), and $R = \left(\frac{\sum_{j=0}^{M-1} jN_j}{N_c} + \frac{1}{2}\right)$. According to Equation 2.11, the fluorescence decay profile can be put directly into the equation and get the lifetime. This equation also is implemented into GUI software for rapid lifetime analysis.

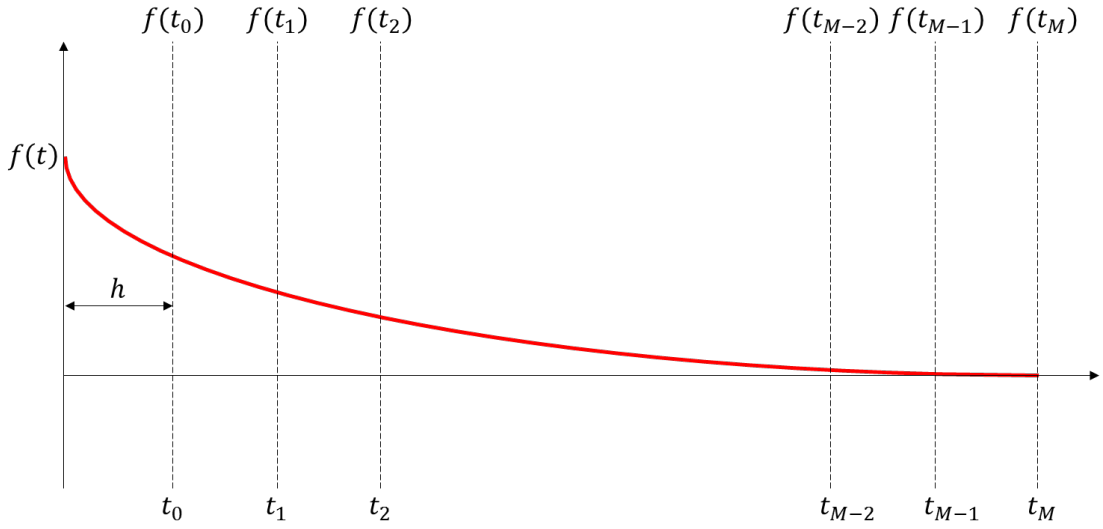

Figure 2.11 M time bins with width h that stores photon events in hardware

The accuracy of CMM is determined by quantisation error and the precision is from Poisson noise, which can be improved by increasing photon counts [53]. The CMM method relies on user-pre-defined measuring windows and the result is very sensitive to the start and end of the window that covers the decay curve. A too-large or too-small window may cause a shift in CM and generates an inaccurate lifetime. For accurate determination of the lifetime, the CMM is applied to both the fluorescence decay and the IRF data to obtain τ_{CMM} and τ_{IRF}, respectively. Subsequently, the IRF-calibrated lifetime (τ_{diff}) is calculated using Equation 2.12 [55].

$$\tau_{diff} = \tau_{CMM} - \tau_{IRF} \tag{2.12}$$

2.6.2 Phasor plot analysis

Phasor has been purposed to reduce the complexity and time consumption of FLIM analysis [49]. Phasor is a technique to illustrate FLIM data as a graphical representation by mapping fluorescence decay from a single pixel to a single dot in a Fourier space indicated by real part

(Re) and imaginary part (Im) coordinates. The coordinates are expressed by Equations 2.13 and 32 [63].

$$Re_{i,j}(\omega) = \frac{\int_0^T I_{i,j}(t) \cdot \cos(\omega t)\, dt}{\int_0^T I(t) dt} \tag{2.13}$$

$$Im_{i,j}(\omega) = \frac{\int_0^T I_{i,j}(t) \cdot \sin(\omega t)\, dt}{\int_0^T I(t) dt} \tag{2.14}$$

where $Re_{i,j}$ and $Im_{i,j}$ are the x and y coordinates of the phasor plot, i and j are pixel positions in FLIM image, ω is the angular frequency of the modulated signal, $I(t)$ is the decay function and the term $\int_0^T I(t)dt$ is total photons. The transformed decay always appears within the universal semi-circle with values $0 < Re < 1$ and $0 < Im < 0.5$.

However, in the TCSPC system, the sample is exposed to a pulsed laser not modulated laser. Therefore, the ω can be rewritten as $2\pi/T$. Moreover, the fluorescence decay acquired from SPAD is a discrete function where the distance between data points is defined by bin width. It is impossible to perform transform the decay using Equations 2.13 and 2.14, therefore the Re and Im equations can be rewritten as Equations 2.15 and 2.16 where t is the time bin and T is the total time bin.

$$Re_{i,j} = \frac{\sum_0^T I_{i,j}(t) \times \cos\left(\frac{2\pi}{T} t\right)}{\sum_0^T I_{i,j}(t)} \tag{2.15}$$

$$Im_{i,j} = \frac{\sum_0^T I_{i,j}(t) \times \sin\left(\frac{2\pi}{T} t\right)}{\sum_0^T I_{i,j}(t)} \tag{2.16}$$

In the experiment, the recorded fluorescence decay does not only represent the lifetime of the fluorescent species but also includes the contribution from the IRF and the phasor polar position is always shifted by θ_1 due to IRF (Figure 2.12(A)). For accurate determination of phasor plot, the plot must be calibrated by IRF which represents zero lifetime species to remove the shifting, as shown in Figure 2.12(B) and generate high-quality fluorescence phasor plots. The phasor position of the IRF is described by Equations 2.17 and 2.18.

$$Re_{irf} = \frac{\sum_0^T I_{irf}(t) \times \cos\left(\frac{2\pi}{T} t\right)}{\sum_0^T I_{irf}(t)} \tag{2.17}$$

$$Im_{irf} = \frac{\sum_0^T I_{irf}(t) \times \sin\left(\frac{2\pi}{T} t\right)}{\sum_0^T I_{irf}(t)} \tag{2.18}$$

where I_{irf} is IRF measured from urea crystal. Therefore, the IRF-calibrated *Re'* and *Im'* can be rewritten as Equation 2.19 and 2.20 to represent the phasor position of IRF as a zero-lifetime value.

$$Re'_{i,j} = (Re_{i,j})(Re_{irf}) + (Im_{i,j})(Im_{irf}) \quad (2.19)$$

$$Im'_{i,j} = -(Re_{i,j})(Im_{irf}) + (Im_{i,j})(Re_{irf}) \quad (2.20)$$

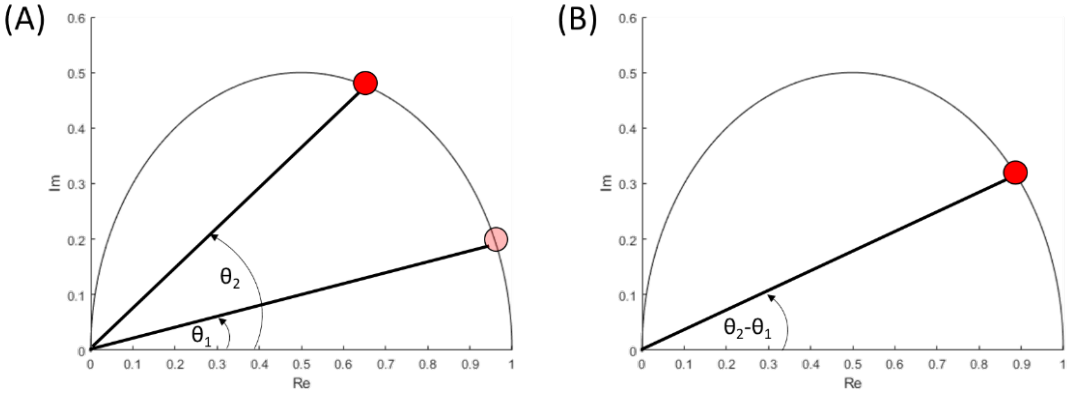

Figure 2.12 Diagrams showing (A) phasor position of the sample (red) and IRF (light red), and (B) IRF-calibrated phasor position.

The phasor plot is commonly used to represent complex signals in a simplified way. The phasor diagram provides information on both the magnitude and the phase of the signal, making it a useful tool for analysing decay curves of fluorescence emission. The position of the phasor on the diagram is indicative of the decay curve's characteristics. Mono-exponential decay curves, which are representative of a single decay process, appear as a straight line along the universal semicircle. In contrast, multiple-exponential decay curves, which are characteristic of multiple decay processes, appear inside the semicircle. Furthermore, any reaction that occurs in the excited state of a molecule can result in a movement of the phasor's position outside the boundaries of the semicircle. Such deviations, also known as complex phasors, can provide information on the dynamics of the reaction, including the presence of energy transfer pathways, quenching, or excited-state reactions [63].

The phasor's spatial orientation not only imparts insight into the distinctive decay profile characteristics but also bears a correlation to the lifetime of the constituent species. Notably, the right segment of the semicircular representation (as delineated in Figure 2.13(enclosed in a red circle)) corresponds to species that exhibit shorter lifetimes, whereas the left segment indicates longer lifetime species. The association between phasor position and lifetime is described somewhere [65]. In instances where only species with a singular lifetime is present,

the lifetime may be estimated directly using the coordinates through the application of Equation 2.21.

$$\tau = \frac{T}{2\pi}\left(\frac{Im}{Re}\right) \tag{2.21}$$

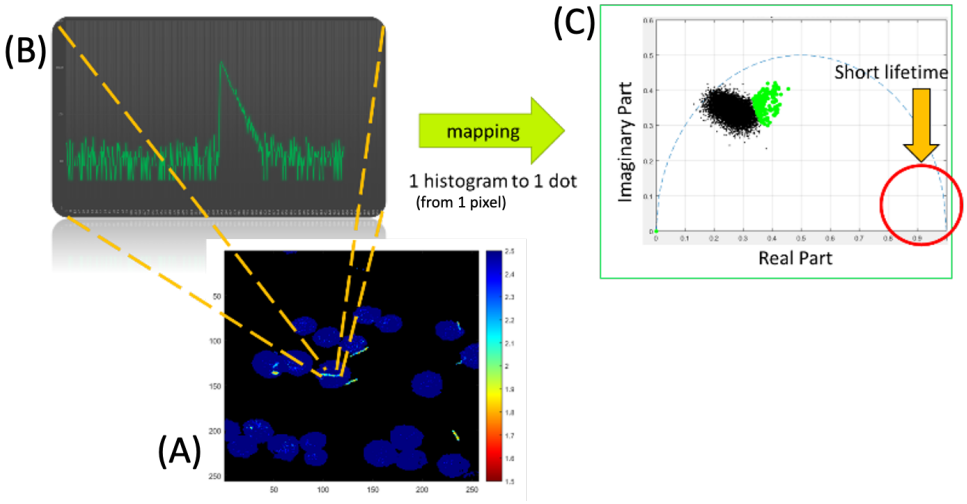

Figure 2.13 Process of phasor analysis (A) FLIM image of GFP-labelled lactobacillus and Alexa 548 labelled cell actin macrophage (B) Histogram of one pixel from the FLIM image (C) Phasor plot of all pixels of the image showing two-lifetime population black and green dots.

2.7 Conclusion

In this chapter, we discuss the experimental methods employed in this work. UV-Vis absorption spectroscopy is utilized to determine the concentration of the gold nanoprobe, applying the Beer-Lambert law. Steady-state measurements provide the spectral fingerprint of the sample, indicating the optimal excitation wavelength for the highest emission intensity. We delve into the details of fluorescence lifetime spectroscopy, covering instrumentation and the exponential decay fitting model. This lifetime spectroscopy is crucial for characterising the dye used in this work and for observing changes in the fluorescence lifetime of the gold nanoprobe in the presence and absence of the mRNA target. Additionally, FLIM is performed in this work to measure the intracellular gold nanoprobe lifetime and compare it with the results from our cancer cell screening system. Lastly, we introduce a novel, fast, and fit-free method for fluorescence lifetime analysis, including CMM and phasor plot illustrations.

Chapter 3 A fast and fit-free analysis platform for routine cancer cell studies using FLIM

3.1 Introduction

Cancer is a significant global health concern, representing the second leading cause of death worldwide. In 2014, there were 163,000 cancer-related deaths in the UK, and the mortality rate is on the rise [66]. Lung and prostate cancers are prevalent in men, while breast cancer is common among women. Cancer is a complex disease that progresses through multiple stages, leading to increased mortality. To mitigate cancer mortality rates and enhance patient survival, the development of sensitive, specific, and cost-effective tools for early, rapid and reliable cancer diagnosis is necessary.

Most cancer detection tools currently rely on antibody labelling for protein detection, which necessitates multiple procedures, expert assessment, and expensive reagents. Messenger RNA (mRNA) is one type of RNA which is an essential intermediary in protein production at the cellular level, lying between DNA genes and protein products. Cancer cells exhibit distinct RNA expression from healthy cells, making it feasible to detect the presence of cancerous cells using mRNA-based approaches. mRNA has been found in the serum of cancer patients, and C-Myc is a critical factor involved in regulating cellular growth and metabolism, making it an attractive target for early-stage cancer detection [57], [67].

Recent studies have shown that mRNA nanoprobe-based on gold nanorods is a promising approach to differentiate between healthy and cancer cells based on fluorescence intensity and lifetime [17], [18]. The nanoprobe consists of a GNR core with a fluorophore-labelled single-stranded DNA in hairpin shape (hpDNA) with sequences in the loop complementary to the target RNA. GNRs emerge as optimal candidates for fluorophore-quenching nanosensors, mainly owing to their biocompatibility and distinctive optical properties rooted in the concept of LSPR. The LSPR effect in GNRs is a result of the oscillation of free electron clouds around the metal core, particularly along the axis of the nanorod. This generates absorption of light at specific wavelengths, enabling efficient energy transfer between GNRs and nearby fluorophores [68], [69]. Although LSPRs are found in other types of nanoparticles, the LSPR in gold nanospheres is not tuneable [70], while the LSPR in silver nanoparticles is tuneable but has a very broad absorption wavelength [71]. The GNRs' dual absorption peaks further contribute to their versatility, with the absorption from the transverse mode around 500 nm and a tuneable longitudinal mode ranging 600 to 1000 nm [72]. The

strong absorption property of GNRs makes them ideal fluorescence quenchers in distance-dependent FRET, with an effective range between the fluorophore and GNR surface of approximately 1 to 8 nm [3]. Furthermore, the nanoprobe exhibits the ability to recognise and bind to a complementary single-stranded DNA sequence [29]. In the absence of target mRNA, the hpDNA typically forms a stem and loop structure, as shown in Figure 3.1, resulting in the quenching of fluorescence through nonradiative dipole-dipole interactions. In the presence of complementary DNA (cDNA) targets, hpDNA undergoes a structural transition from a looped to linear form, leading to a distance increase between the fluorophore and GNR of up to 20 nm. This removes quenching and subsequently leads to recovery or even an enhancement of fluorescence intensity and changes in fluorescence lifetime [3].

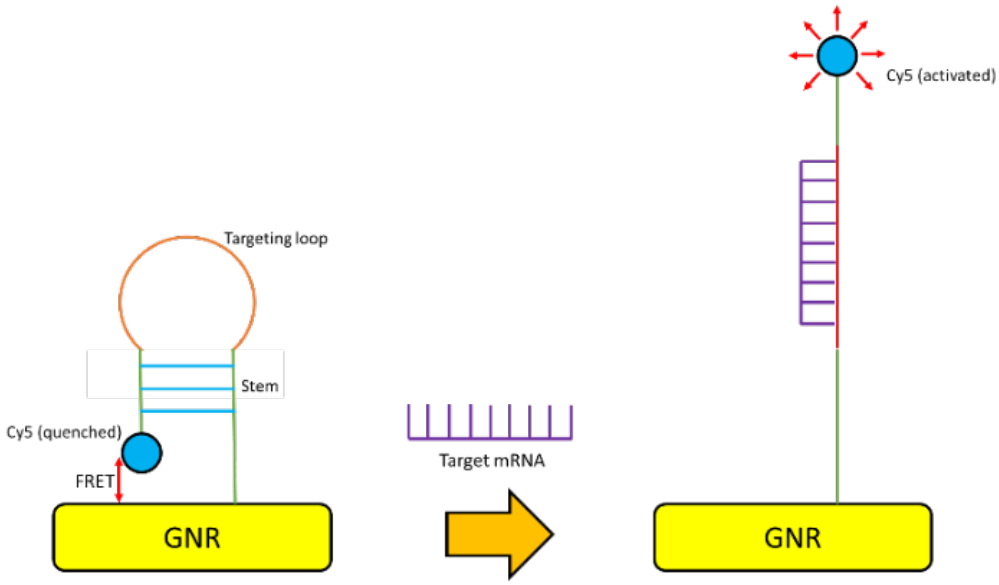

Figure 3.1 An illustration of hairpin DNA fictionalised GNR for mRNA detection: closed-loop (left) and opened-loop (right)

Previous studies have demonstrated that FLIM for intra-cellular imaging of GNRs results in improved contrast compared to traditional fluorescence intensity imaging. This enhancement is shown by the large differences in fluorescence lifetime between GNRs and the surrounding cellular environment, for example, the two-photon luminescence of gold nanorods have typically short lifetimes (100ps) compared to the fluorescence lifetimes of typical fluorophores (1.0 ~ 4.0 ns) [73]. Furthermore, FLIM imaging can assess the energy transfer between gold nanorods to adjacent fluorophores and FRET-FLIM has been successfully employed in resolving the cell take-up of gold nanorods and intra-cellular pathways [74], [75]. FLIM is not only able to distinguish spectrally overlapping fluorophores but it can also be used to probe the immediate surroundings and dynamical processes of fluorophores.

Commercially available FLIM analysis tools usually provide initial quick analysis such as first-moment analysis, and curve-fitting routines for further detailed analysis that requires end-users to choose fitting models (mono-, bi- or multi-exponential) and perform the analysis based on whether the reduced-chi squared is within a specific user-selected criterion. Such exponential models, however, cannot be defined properly in complex biological systems and the fitting routine is not mathematically unique, which can lead to ambiguous interpretations. This is why more and more FLIM researchers are applying the phasor approach [76]–[78] to avoid complications in analysis and interpretations. Although some commercial tools do allow users to choose their areas of interest, they are not free [79], [80].

In many applications, the analysis goal is to obtain the average lifetime to provide contrast instead of resolving all unknown parameters. Without resorting to complex iterative curve-fitting routines, there are easier ways to obtain lifetime information by using the CMM method and phasor plot. The CMM method has been proven without [81] or with the IRF considered [82]. The measured IRF is also calibrated in the phasor analysis provided by the proposed analysis platform.

In this study, the developed analysis platform is used to study FLIM images through three different lifetime analyses: the centre of mass method, the non-linear fitting model [83], and the phasor plot. These methods serve as distinct mappings to optimise contrast according to the applications of the user. The decay function was calibrated using the IRF obtained from dried urea ($(NH_2)_2CO$) measurements [84]. The calculation speed is assessed by benchmarking the total calculation time on a PC equipped with an Intel core i5-7500 3.40 GHz CPU and 16 GB RAM running MATLAB software. The developed platform presents a novel approach for rapid and model-free lifetime analysis without requiring fluorescence decay model selection (Figure 3.5). By using the mRNA nanoprobe, the platform enables the visualisation of cancer and non-cancer cells through phasor plots, distribution plots, and fluorescence lifetime and intensity images. Its user-friendly design simplifies lifetime analysis, making it suitable for routine applications in cancer studies. Additionally, users can easily select regions of interest (ROI) from phasor plots, lifetime images, and intensity images, facilitating rapid cross-comparison studies.

3.2 RNA nanoprobe preparation

The nanoprobe described in this study is based on the utilisation of DNA-functionalised GNRs. The synthesis process for the probe has three steps, including the synthesis of the GNRs, a round-trip phase transfer (also known as a ligand exchange process) and DNA functionalisation. The GNR synthesis process is a two-step procedure, which requires the use

of a surfactant such as cetyltrimethylammonium bromide (CTAB) to selectively control the growth area of the GNRs. However, the positively charged bilayer of CTAB has been found to have a strong cytotoxic effect due to its ionic nature, which can interact strongly with nucleic acids. To mitigate this issue, the CTAB is replaced with a more suitable thiol molecule, such as mercaptohexadecanoic acid (MHA), through a ligand exchange process during the synthesis. This step enables the subsequent DNA functionalisation.

3.2.1 GNR synthesis

The GNR is synthesised by a seed-mediated method assisted by silver nitrate (AgNO3) which is 2 step process: seed and growth solution [16], [17], [85], [86]. Figure 3.2 illustrates the overprocess of this synthesis process. Firstly, the seed solution is prepared by adding 0.25 ml of 1 mM $HAuCl_4$ into 7.5 ml of CTAB while it is being vigorously stirred and then 0.6 ml of 0.01M ice-cold $NaBH_4$ is added at once at the moment the solution changes to yellow-brown colour. The seed solution depends on the CTAB quality [87]. The seed solution is kept undisturbedly for 3 hours to get 3.5 – 4 nm GNPs [21]. Secondly, the growth solution is prepared by mixing 200 ml of 0.2M CTAB, 200 ml of 1 mM $HAuCl_4$, 10 ml of 4 mM $AgNO_3$, and 2.8 ml of 0.0778 M ascorbic acid (AA), respectively. After adding AA, the colour of the solution changes from orange-brown (Au^{3+}) to colourless (Au^{+}). Then, the stirring is turned off to stabilise the growth solution for 1 minute. Finally, 0.4 ml of the seed solution is injected into the growth solution. The final solution is kept in an incubator (37 C°) overnight to get GNR-CTAB. To wash the synthesised GNR and remove the excess CTAB, the GNR-CTAB solution is centrifuged at 12,000 rpm for 30 minutes, remove supernatant and re-suspended in distilled water, then repeat the washing again. The washed GNR-CTAB is measured in concentration by UV-Vis and kept in the dark at room temperature. This process requires a good quality of CTAB as different purities may give different results [88].

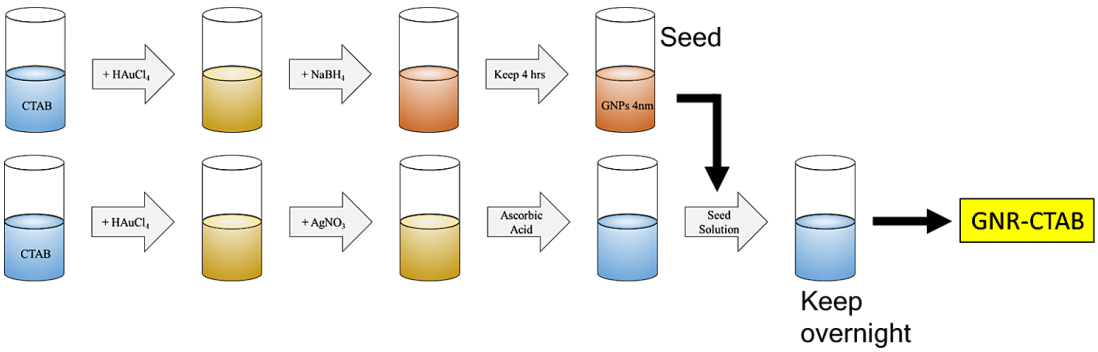

Figure 3.2 Schematic diagram showing GNR-CTAB synthesis process. Seed and growth solutions are prepared separately. The seed is added to the growth solution after incubation for 3 hours.

3.2.2 Ligand exchange process

Gold nanorods have been widely studied for their biocompatibility, making them a promising material for various biomedical applications, including in vivo diagnosis and therapy. However, a limitation of utilising GNRs in these applications is the toxicity of the CTAB commonly used during the synthesis process [88]. Despite the biocompatibility of the GNRs themselves, the presence of CTAB in the GNR-CTAB makes it incompatible for in vivo use due to its cytotoxic effects on cells. Therefore, alternative surfactants such as MHA must be used in order to produce GNRs that are suitable for in vivo applications.

The round-trip phase transfer process includes 2 main steps: removing CTAB and ligand exchange [89]. This process is illustrated in Figure 3.3. To remove the covering CTAB, the process starts by mixing 25-50 nM of GNR-CTAB and dichlorodiphenyltrichloroethane (DDT) with the same volume for 10 seconds. Acetone (C_3H_6O) is added to make a solution with GNR-CTAB:DDT:Acetone ratio 1:1:4 and mixed for 10 seconds, at this moment, the CTAB has been replaced by DDT. After 5 minutes the solution splits into 2 layers and the GNR-DDT is collected from the top layer. The excess DDT is removed by adding toluene ($C_6H_5CH_3$) and methanol (CH_3OH) with GNR-DDT:$C_6H_5CH_3$:CH_3OH ratio 1:1:5, gently stirring, then incubate for 3 hours. The solution divides into two layers where the pellets of GNR-DDT are precipitated to the bottom after 3 hours. The top layer of the solution is carefully removed.

The ligand exchange process involves vigorously mixing GNR-DDT with MHA and toluene in a heat bath, where the flask is temperature-controlled at 97°C. The GNR-DDT is re-suspended in 1 ml of toluene in a sonic bath for 2 seconds. The process begins by adding 9 ml of toluene to the flask as the temperature reaches 97°C, followed by the addition of 13 µl of 0.01 M MHA and the re-suspended GNR-DDT when the temperature stabilises at 97°C. The reaction continues for 10 minutes or until some aggregations are observed. Subsequently, the flask is removed from the heat bath, washed twice with 2 ml of toluene, and the product is collected by re-suspending it in 1.4 ml of isopropanol (C_3H_8). After centrifugation at 8000 rpm for 6 minutes and drying at room temperature for 5 minutes, the excess solution is removed. Finally, the GNR-MHA is stored by re-suspending it in 50 µl of Tris-Borate-EDTA (TBE) buffer. The success of the reaction can be confirmed by observing two clear peaks in UV-Vis absorption spectroscopy.

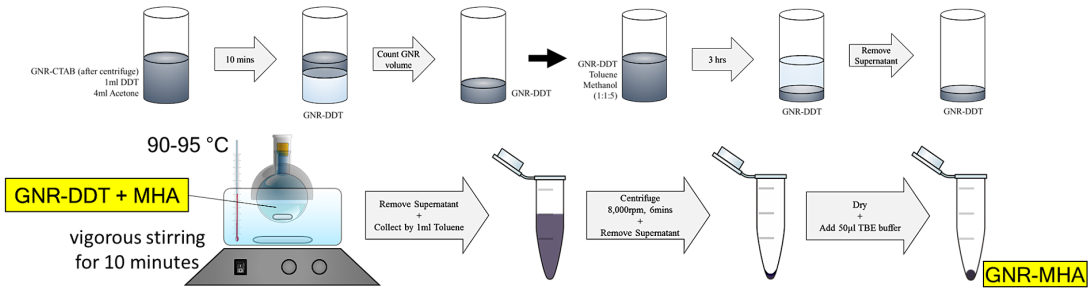

Figure 3.3 Schematic diagram showing ligand exchange process to modify GNR surface from CTAB to MHA.

3.2.3 DNA functionalisation

hpDNA with a fluorophore at the 3' end and thiol group at 5' is used to attach with GNR. The base sequence of hpDNA is shown in Table 1. The underlined bases form a stem structure, while the italicised bases correspond to the mRNA-sensitive region. The hpDNA is activated in tris(2-carboxyethyl)phosphine (TCEP) in 1X Tris-EDTA (TE) buffer for 1 hour in a temperature-controlled shaker in the dark at 4°. The ratio of hpDNA and TCEP in TE is 1:1. Then, the hpDNA is precipitated in a mixture of ethanol, NaMgAcetate and hpDNA with a ratio of 7:1:2 respectively and the mixture is kept in a -20°C freezer for 2-3 hours. Next, the mixture is centrifuged at 97°C 13000 rpm for 15 minutes, remove from the supernatant and re-suspend in 100 µl ddH_2O.

The GNR-MHA is functionalised by the activated hpDNA by the salt ageing process shown in Figure 3.4. The concentration ratio of hpDNA:GNR is 1:400. The GNR-MHA is centrifuged at 12,000 rpm for 10 minutes at room temperature. The total volume of the salting solution is calculated to achieve a concentration of 5 nM gold nanorods (GNR). This solution is prepared by mixing GNR with 100 µl hpDNA, 10% of the total volume of 0.02% SDS, 10% of the total volume of 1 mM Sodium phosphate buffer (Na phosphate buffer, pH 5), and ddH2O. The mixture is then shaken at 1100 rpm in the dark at 4°C overnight. At this stage, the solution appears black with a blueish tint from the Cy5 in the hpDNA strand.

The following morning, 10 µl of salting buffer (Na Phosphate, pH 5) is added hourly until it reaches 25% of the total volume. The solution's colour should remain black; if it lightens, the addition is skipped by one hour. This process is terminated when all the salting buffers have been added, precipitation of black powder is observed, or the solution becomes clear. Subsequently, the solution is shaken overnight at 4°C in the dark.

The next morning, the solution undergoes washing by centrifugation with two different washing buffers: (1) a mixture of 1 ml 10 mM Na phosphate buffer pH 7, 1 ml 0.02% SDS,

and 8 ml ddH2O, (2) a mixture of 1 ml 10 mM Na phosphate buffer pH 7 and 9 ml ddH2O. This washing process is repeated four times with the first buffer and three times with the second buffer, removing excess hpDNA-Cy5 remaining from the reaction. The washed nanoprobe is re-suspended in 50 µl of 10 mM Na phosphate buffer (pH 7) and stored at 4°C in the dark.

Table 1 Sequence of hpDNA and cDNA [17]

Sample	DNA sequence
hpDNA-Cy5	5'-Cy5-CTGACTTG *GTG AAG CTA ACG TTG AG* CAAGTCAG-AA-$(CH_2)^6$-HS-3'
C-Myc cDNA	5'-CCT CAA CGT TAG CTT CAC CAA-3'

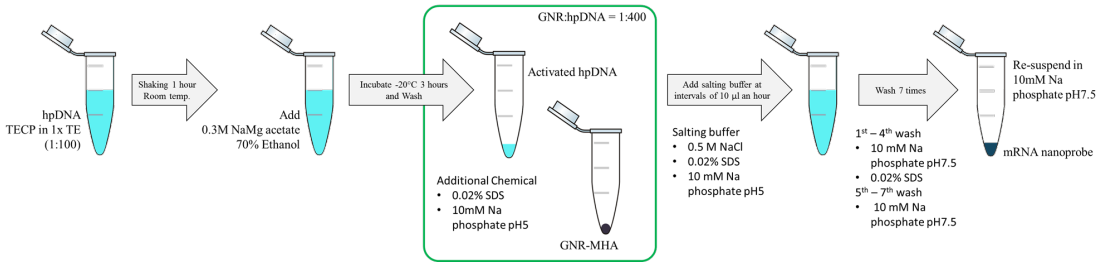

Figure 3.4 Schematic diagram showing the DNA activation process and DNA functionalisation process

3.2.4 Characterisation of hpDNA-Cy5 Nanoprobe

The working principle of the mRNA nanoprobe is based on a FRET pair, comprising a GNR core acting as an acceptor and hairpin DNA labelled with Cy5 dye (hpDNA-Cy5) serving as a donor. The fluorescence of the donor is quenched when it approaches the acceptor, resulting in a reduction in fluorescence intensity and lifetime.

3.2.4.1 Reference measurement of hpDNA-Cy5

The reference measurement of hpDNA-Cy5 was conducted to visualise the excitation and emission wavelengths of the nanoprobe. This was achieved by exposing 312.6 nM hpDNA-Cy5 to excitation light from a Xeon lamp with a wavelength range of 580 to 680 nm. The fluorescence emission was then collected through a monochromator from 600 to 700 nm with a 1 nm increment. A 3D steady-state measurement was performed using the Fluorolog-3 instrument.

The fluorescence lifetime of standalone hpDNA-Cy5 is an important parameter to measure as a reference lifetime in the absence of the quenching effect from GNR. We use the Horiba

DeltaFlex lifetime kit to measure the fluorescence lifetime of hpDNA-Cy5. The excitation of hpDNA-Cy5 was carried out using a 638 nm pulsed laser at a repetition rate of 1 MHz, while the fluorescence emission was collected through a monochromator with a 32 nm window width at 665 nm. To determine the fluorescence lifetime, we fitted the fluorescence decay curve using a 2-exponential decay model described by Equation 3.1.

$$I(t) = A + A_1 exp(-t/\tau_1) + A_2 exp(-t/\tau_2) \quad (3.1)$$

$$\tau_{av} = \frac{A_1\tau_1 + A_2\tau_2}{A_1 + A_2} \quad (3.2)$$

where A is the background value, A_1 and A_2 are the relative amplitude indicating the contribution of lifetime components τ_1 and τ_2, respectively. Then, the average fluorescence lifetime is determined by Equation 3.2.

3.2.4.2 Nanoprobe concentration determination

Ultraviolet-visible spectroscopy (UV-Vis) is used to characterise the optical properties and concentration of the mRNA nanoprobe. The sample is exposed to a halogen and deuterium lamp to produce a broad wavelength range from 200 – 1100 nm, with water serving as the reference. The concentration of the mRNA nanoprobe is determined by applying the Beer-Lambert law, which relates the absorbance of a sample to its concentration and the path length of light through it. The concentration is given by Equation 3.3.

$$c = \frac{A}{\epsilon l} \quad (3.3)$$

where A is the absorbance at the transverse mode peak wavelength (λ), ϵ is the extinction coefficient, l is the optical path, and c is the nanoprobe concentration.

3.2.4.3 Fluorescence Intensity and Lifetime Changes after cDNA Hybridisation

The hybridisation of nanoprobe is a technique used to study the interaction between the hpDNA and the target molecule, such as cDNA. This interaction is characterised by changes in the fluorescence intensity and lifetime of the probe upon binding to the target. In this particular study, 0.1 nM nanoprobe is incubated with the C-Myc cDNA with a ratio of 1:1000 nanoprobe:cDNA. The incubation of the probe and cDNA is conducted at 37°C for 2, 5 and 24 hours in an incubator. The incubated sample is characterised using the change in fluorescence intensity and lifetime measured at various time points, including before the addition of cDNA to the nanoprobe solution and 2 hours, 5 hours, and 24 hours after the addition.

Lifetime measurement of the nanoprobe and hpDNA-Cy5 is performed on a Horiba DeltaFlex. A pulsed laser with a wavelength of 638 nm is used to excite the sample at a repetition rate of

1 MHz. The fluorescence signal is then collected through a 670 nm long-pass filter. The bin width of the TCSPC is set to 26 ps. The fluorescence decay is analysed by the 3-exponential decay fitting method with fixed τ_1 for simulate the scattering signal from GNR, which is described by Equation 3.4 to determine fluorescence lifetime.

$$I(t) = A + A_1 exp(-t/\tau_1) + A_2 exp(-t/\tau_2) + A_3 exp(-t/\tau_3) \quad (3.4)$$

$$\tau_{av} = \frac{A_2\tau_2 + A_3\tau_3}{A_2 + A_3} \quad (3.5)$$

where A is the background value, A_n is the relative amplitude indicating the contribution of each lifetime component τ_n. The value of τ_1 is fixed at 1 bin, equivalent to 26 ps, matching the time resolution of the TCSPC system. This adjustment is made because scattering events typically occur over very short durations, while τ_2 and τ_3 are used to calculate the average lifetime of the sample indicating quenched and unquenched mRNA nanoprobe as shown in Equation 3.5, respectively.

Furthermore, the observation of change in the fluorescence intensity in the presence of cDNA is conducted using the Fluorolog-3 instrument that is equipped with a broad wavelength Xeon lamp. Specifically, the sample is excited by the light that has a wavelength of 640 nm selected by a monochromator, and the emitted light is recorded within the range of 650-750 nm through a monochromator, using a 1 nm step increment. The peak intensity is determined at the emission wavelength of 665 nm.

3.2.5 Fixed cell slide preparation

In order to prepare the fixed cell microscope slide, sterile 13mm coverslips are coated with 200 µl polylysine (Sigma) for 20 mins in a 24-well plate to create a suitable surface for cell attachment. Then, the coverslips are washed with double-distilled water 3 times and left overnight to dry. In each coverslip, 100,000 cells in 0.5 ml cell growth media are seeded and left overnight. On the next day, 0.1 nM of nanoprobe is added to each well and left incubated for 4 hours. After incubation, the coverslip with the cell is washed 3 times with PBS. The cells are fixed by using 4% paraformaldehyde for 15 minutes, followed by 3 washes of double-distilled water. The coverslip is attached cell-side down on a glass slide with 10 µl of mounting media (Fluoroshield, Sigma). The completed microscope slides are left overnight in a 4° fridge to dry.

The utilisation of fixed cell slides in confocal microscopy allows for detailed imaging of cellular structures and dynamics. In this study, a scanning confocal microscope (LSM510) equipped with a TCSPC system was employed to acquire high-resolution images of cells. The microscope was excited using a two-photon excitation source with a laser wavelength of 850 nm, specifically chosen to excite the Cy5 fluorescent dye [90]. The fluorescence signal

was collected through a 63x water-immersion objective lens (N.A. = 1.00), with a 685 nm short-pass filter and a dichroic mirror with R-band > 700 nm to efficiently remove the excitation laser light. To acquire accurate lifetime measurements, each pixel was scanned 100 times to acquire a sufficient number of photons per pixel. The dwell time of each pixel is 1.60 µs, while the time per scan is 986.76 ms.

3.3 Software design

The software is developed by a MATLAB GUI to process the following tasks: converting .asc data from the microscope, loading IRF and FLIM data, analysing the data using multiple methods and displaying analysed data. Once the data has been loaded and clicked the 'Plot' button, the global fluorescence intensity and lifetime, lifetime distribution, fluorescence intensity decay, and phasor plot will be displayed within a few seconds. The main GUI is displayed in Figure 3.5. In addition, Figure 3.6 shows the settings that can adjust the ROI, colour bar and intensity threshold. A popup window for selective area analysis appears after clicking the "Set area" button. The area is defined by a rectangle shape centred at the x and y positions, while the size of the rectangle is defined by the left, right, bottom and top edges. Once, the area has been selected, the user can choose the "Selected area" radio button and click "Plot" to show the data from the specific area. The hand-free phasor gate is performed by clicking the "Phasor Gate" button in the main window. All analysed data can be exported as MATLAB files, images and Excel files.

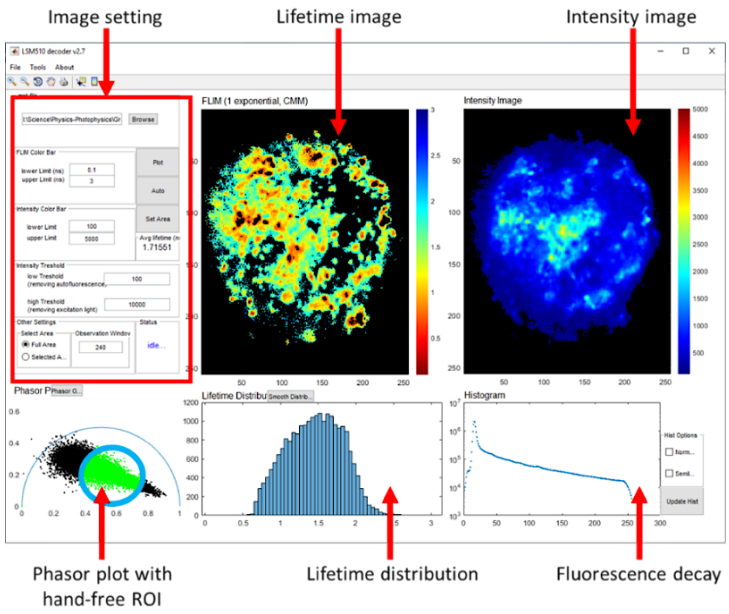

Figure 3.5 Newly developed platform for FLIM analysis showing fluorescence intensity and lifetime images, phasor analysis, decay curves and lifetime histogram corresponding to the selected region of interest.

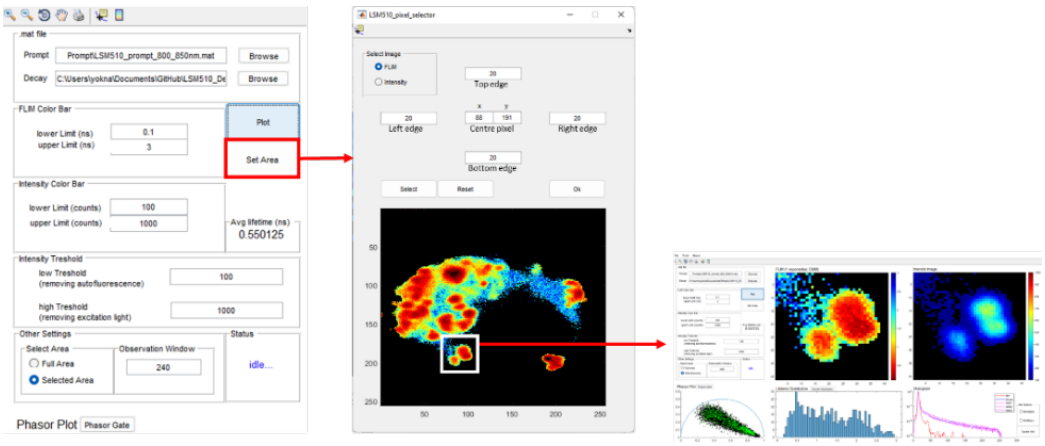

Figure 3.6 Setting parameters and area selection in the GUI.

3.4 Experimental Result

3.4.1 Reference measurement of hpDNA-Cy5 Nanoprobe

The reference measurement of hpDNA-Cy5 includes 3D steady-state measurement and fluorescence lifetime measurement. Figure 3.7(A) displays the steady-state result showing a colour-coded emission intensity plot with varied excitation and emission wavelength, indicating that the hpDNA-Cy5 exhibits the highest intensity indicated by red colour when excited with 645 nm light and detected at 665 nm. In the lifetime measurement Figure 3.7(B) shows the fluorescence decay of the hpDNA-Cy5 with IRF measured from the LUDOX solution. The lifetime is fitted well with a 2-exponential decay model with χ^2 value of 1.04, showing the lifetime value of 1.40 ± 0.01 ns and 0.65 ± 0.02 ns with 90.7% and 9.3% contribution, respectively. The average lifetime of hpDNA-Cy5 is 1.33 ± 0.01 ns.

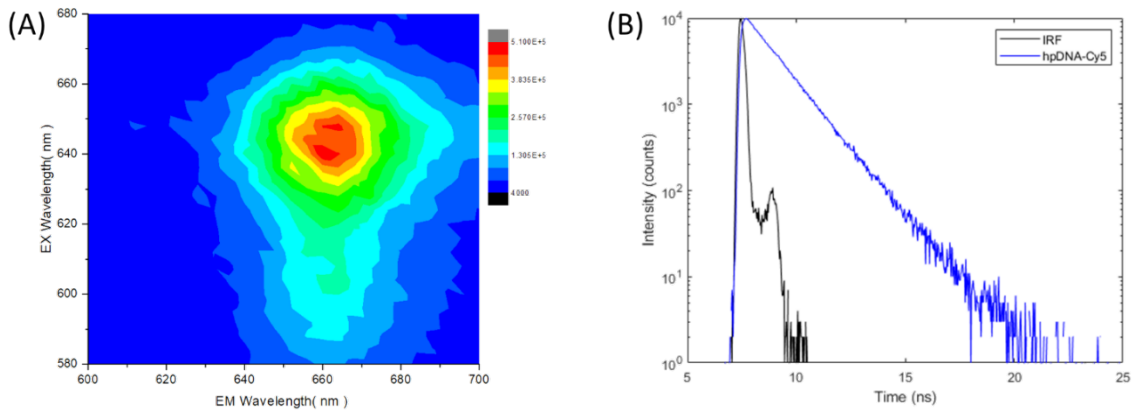

Figure 3.7 (A) colour-coded fluorescence emission intensity with varied excitation and emission wavelength, (B) Measured time-resolved data after excited by 645 nm. Fluorescence decay of hpDNA-Cy5 (blue) is collected at 665 nm and IRF (black) is collect at 645 nm.

3.4.2 Characterisation of mRNA Nanoprobe: Effect of cDNA Hybridisation

The determination of the concentration of the mRNA nanoprobe is an essential step before studying cDNA hybridisation to ensure the correct amount of cDNA required for testing the nanoprobe. The concentration can be determined by applying the Beer-Lambert law to the absorption spectra. Figure 3.8 illustrates the absorption spectra of the 20-times dilution of the mRNA nanoprobe in a 100 µl microcuvette after the DNA functionalisation process and overnight incubation. The spectra reveal three distinct absorption peaks at 260, 524, and 766 nm, corresponding to hpDNA at 260 nm [91] and the transverse and longitudinal modes of LSPR, respectively. In this study, the parameters A = 0.83, l = 1 cm, and ε = 4.4 $nM^{-1}cm^{-1}$ were determined and used to calculate the concentration of the nanoprobe as 0.19 nM.

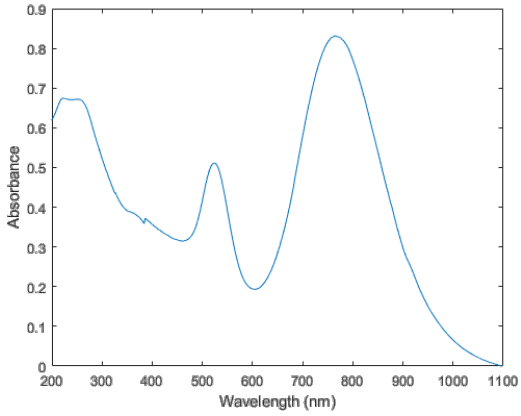

Figure 3.8 Absorption spectrum of mRNA nanoprobe

The present study aimed to characterise the performance of a synthesised nanoprobe in detecting a specific target cDNA sequence. To ensure that the added cDNA is abundant enough to be reliably detected by the nanoprobe, the nanoprobe:cDNA ratio was set to 1:1000. The characterisation was conducted both before the addition of 100 µM cDNA (0.19 µl) to the nanoprobe solution and after the addition of cDNA.

Steady-state measurements showed that the fluorescence emitted from the nanoprobe alone was of relatively low intensity. However, upon the introduction of cDNA, a noticeable increase in fluorescence intensity was observed, starting at I_0 = 1120 counts per second (cps), and increasing over time, as illustrated in Figure 3.9. The fluorescence intensity values at 2 hours, 5 hours, and 24 hours were 1625 cps, 1928 cps, and 3258 cps, respectively. This significant 2.91-fold increase in intensity suggests that the synthesised nanoprobe is a DNA sequence capable of binding to the target cDNA. The results thus demonstrate the potential of the nanoprobe for use in the sensitive detection and quantification of specific DNA sequences.

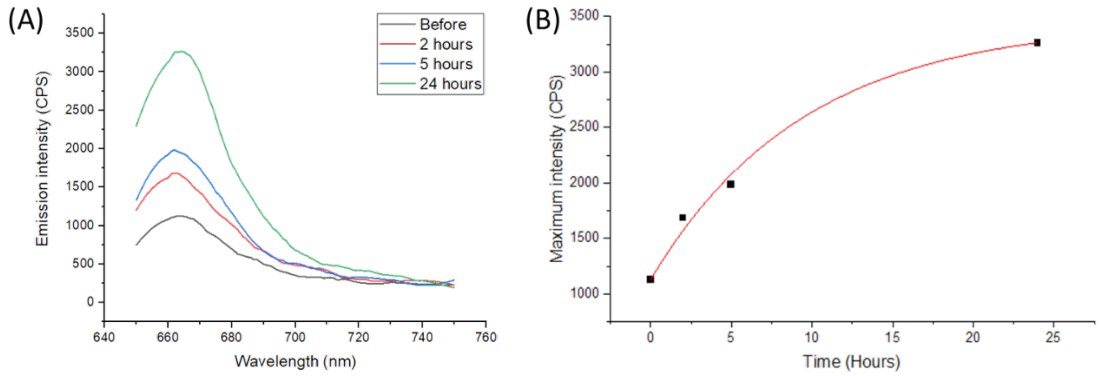

Figure 3.9 (A) Fluorescence emission spectral profile before and after adding cDNA for 2, 5 and 24 hours (overnight) (B) Fluorescence intensity at λ = 665 nm.

In order to further characterise the nanoprobe, fluorescence lifetime measurements were conducted using a TCSPC system to investigate the quenching effect and recovery of Cy5 after the introduction of cDNA. As shown in Figure 3.10(A), the fluorescence decay of the nanoprobe was monitored over time. These decays were then subjected to analysis using a least square fitting method and a 3-exponential decay model. Table 2 presents the relative amplitude (A) values for the corresponding analysed lifetime contributions, which represent scattering from gold nanorods (τ_1), quenched Cy5 (τ_2), and unquenched Cy5 (τ_3), with a value of approximately 1. Notably, τ_1 was fixed at 26 ps, as scattering typically occurs over a short period of time. These findings provide further insight into the performance of the synthesised nanoprobe, particularly with regard to the quenching effect and the recovery of Cy5 fluorescence upon binding to the target cDNA sequence.

The fluorescence lifetime results are shown in Table 2 and Figure 3.10. Before introducing the cDNA, τ_2 and τ_3 shows values of 0.15 ± 0.04 and 1.24 ± 0.01 ns, respectively. After adding cDNA for 2 hours, 5 hours and 24 hours, τ_3 shows increasing values from 1.29 ± 0.01 ns to 1.36 ± 0.01 ns, while τ_2 slightly increases to 0.33 ± 0.05 ns. The relative amplitude is also an important variable showing the percentage contribution of the corresponding lifetime. As shown in Figure 3.10(B), A_1 represent the contribution of scattering signal that significantly decrease from 61.05% to 39.17%, while A_3 shows the increase in the contribution of unquenched Cy5 from 34.11% to 54.13% after cDNA incubation. Interestingly, A_2 indicates quenched Cy5 with a contribution of 4.84%. A_3 reaches the maximum at 2 hours, then slowly decreases to 6.71% when incubate overnight. The lowest A_2 before incubation is due to the strong quenching effect from GNR on the Cy5 that makes the life very short enough to combine with A_1, as shown by the extra contribution of A_1 at 61.05%, compared to stable A_1 contribution of around 40% from 2 – 24 hours. This also

shows that some nanoprobe has been already unquenched before adding the target. Unlike intensity-based characterisation, the nanoprobe only shows a 1.76-fold of average lifetime increase (Figure 3.10(C)).

Table 2 Fluorescence lifetime fitted parameters with the 3-exponential model with the fixed first component at 26 ps before and after incubating with the nanoprobe for 2 hours, 5 hours and 24 hours. These three-lifetime components indicate scattering from GNR (τ1), quenched Cy5 (τ2) and unquenched Cy5 (τ3). A1, A2 and A3 values represent the relative contribution of the corresponding lifetime value to the measurement. τ_{AVG} is the average lifetime calculated from the second and third components excluding the contribution from scattering. This fitting process indicates a good fit with χ2 between 0.9 – 1.2.

Time (hours)	A_1	τ_1 (ps)	A_2	τ_2 (ns)	A_3	τ_3 (ns)	τ_{avg} (ns)	χ^2
0	61.05	26	4.84	0.15 ± 0.04	34.11	1.24 ± 0.01	0.43 ± 0.03	0.97
2	40.81	26	11.68	0.10 ± 0.04	47.51	1.29 ± 0.01	0.63 ± 0.03	0.97
5	43.25	26	7.38	0.13 ± 0.06	49.37	1.30 ± 0.01	0.65 ± 0.04	1.17
24	39.17	26	6.71	0.33 ± 0.05	54.13	1.36 ± 0.01	0.76 ± 0.03	1.08

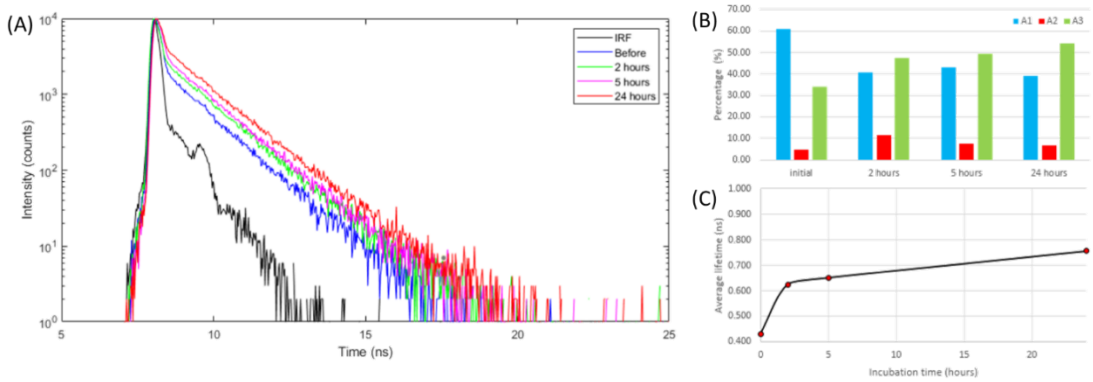

Figure 3.10 (A) Fluorescence intensity decay of the nanoprobe before (blue) and after 2 hours (green), 5 hours (magenta), and 24 hours (red), while the black line indicates IRF. (B) The relative contribution of each lifetime component from scattering (blue), quenched.

The result from steady-state and fluorescence lifetime measurement shows increasing in fluorescence intensity and lifetime after adding the cDNA. This indicates the decreasing FRET efficiency described by the hybridisation of cDNA with the hairpin loop of the probe that results in a structural change of the hpDNA that moves the fluorophore away from the GNRs. FRET is not only a distance-dependent phenomenon but also requires an overlap

spectral area between the donor's emission and the acceptor's absorption. Figure 3.11 shows the overlap area between the emission of Cy5 (orange line) and the absorption of the longitudinal surface plasmon peak of the GNRs (yellow line), however, this area is not ideal resulting in high background levels in the absence of cDNA. These results suggest that a nanoprobe is a promising tool for sensitive detection and quantification of the cDNA sequences, which can be applied to biological and clinical applications.

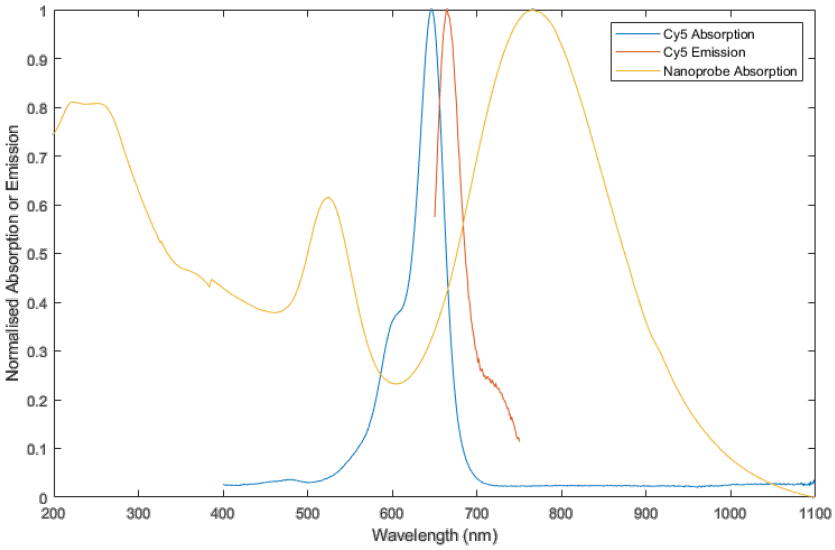

Figure 3.11 A spectral plot showing Cy5 absorption (blue), Cy5 emission (read), and GNR absorption (yellow). The absorption wavelength of the GNR is overlapping with the emission from Cy5.

3.4.3 Investigating fluorescence lifetime in cancer and non-cancer cell using the developed platform

The objective of this study was to evaluate the performance of the platform in identifying cells by utilising the C-Myc nanoprobe. The nanoprobe was incubated in two different cell lines: non-cancer Human embryonic kidney 293 (HEK293) and human prostate cancer (PC3) that over-express C-Myc mRNA. The resulting fluorescence intensity images are presented in Figure 3.12(A and B) for PC3 and HEK293 cells, respectively. The data obtained were analysed using the platform's implementation of CMM (τ_{CMM}) and phasor plot analysis, while a traditional exponential decay fitting method defined by τ_{FIT} was also performed on the same PC for comparison of analysis speed.

The developed platform demonstrates superior performance in terms of speed and contrast compared to traditional fitting methods. This is demonstrated by the global fluorescence decay generated from FLIM data, presented in Figure 3.12(I). Additionally, Figure 3.12(E

and F) depict the τ_{CMM} images of HEK293 and PC3 cells, respectively, incubated with the mRNA nanoprobe and generated by the platform in mere 0.14 seconds and 0.15 seconds, respectively. In contrast, τ_{FIT} images (Figure 3.12(C and D)) were separately generated by a MATLAB code and required 1,206.72 seconds and 1,178.73 seconds, respectively (Table 3). The same colour scale was used in all images, and it can be observed that the τ_{CMM} images reveal different coded colours for cell or nanoprobe pixels, while the τ_{FIT} images were overwhelmed by the strong signal from two-photon luminescence from GNR, which has a very short lifetime. In terms of phasor analysis, the platform takes only 0.07 seconds and 0.10 seconds to generate global phasor plots of HEK293 and PC3 cells, respectively, indicated by the black dots in Figure 3.12(G and H).

In order to ensure that the platform can accurately distinguish between tumour cells that have hybridised with the target mRNA nanoprobe and those that have not, the platform employs a combination of intensity thresholding and phasor gating techniques. The intensity threshold is used to remove autofluorescence, while the phasor gate is used to filter out signals from GNR. The position of the GNR signals in the phasor plot has been previously reported as being located in the bottom right corner of the short lifetime region, whereas signals from control cells are typically found in the long lifetime region at the top left [49], [63]. As illustrated in Figure 3.12(G and H), these are τ_{CMM} images of ROI that were selected by applying a threshold of intensity greater than 200 counts and a hand-free phasor gate (shown in Figure 3.12(K and L)), in order to extract the unquenched nanoprobe signal.

From Table 3, in HEK cells incubated with a nanoprobe containing an ROI, the fluorescence lifetime imaging (FLIM) image appears black due to the removal of most pixels outside of the ROI. Analysis of the remaining pixels shows average $\tau_{CMM} = 0.93 \pm 0.02$ ns and $\tau_{FIT} = 0.21 \pm 0.02$ ns. As demonstrated by the phasor plot, which also shows a position close to the bottom right area, the data indicates a short lifetime from quenched Cy5 in the nanoprobe in HEK293 cells. In contrast, the FLIM image for PC3 cells incubated with the same nanoprobe and ROI displays a yellow, green and blue ring with a lifetime between 1.0 – 1.5 ns. The ROI analysis shows average $\tau_{CMM} = 1.25 \pm 0.43$ ns and $\tau_{FIT} = 0.27 \pm 0.11$ ns, which is longer than in HEK293 cells, suggesting reduced quenching between Cy5 and gold nanoparticles. This is confirmed by the τ_{CMM} distribution plot as shown in Figure 3.12(J). The phasor plot also demonstrates this trend, with more green dots located in the middle of the plot, indicating a longer lifetime region.

The results of the study indicate that the τ_{CMM} method exhibits significantly superior performance in terms of speed and resolvability compared to the τ_{FIT} method. Specifically,

the τ_{CMM} demonstrated a 1000-fold increase in speed when compared to the fitting method. Additionally, the τ_{CMM} method provided a higher level of contrast, with a lifetime ratio (τ_{PC3}/τ_{HEK293}) of 1.34 for nanoprobe in PC3 and HEK293 cells, as opposed to the ratio of 1.29 obtained using the τ_{FIT} method.

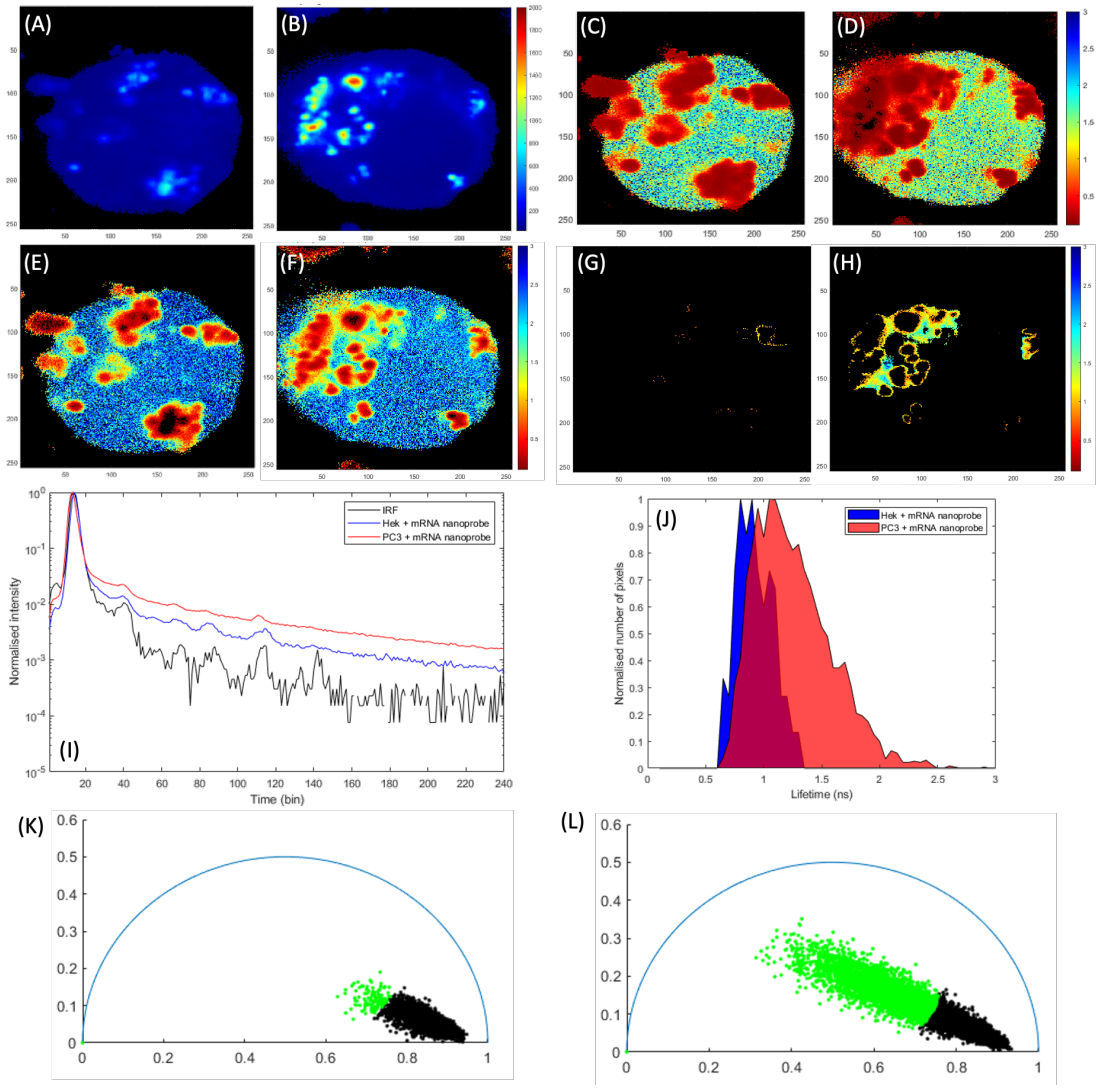

Figure 3.12 Fluorescence intensity images of (A) HEK293 with nanoprobe and (B) PC3 with nanoprobe. Global fluorescence lifetime images of HEK293 with nanoprobe analysed using (C) fitting and (E) CMM methods, and PC3 with nanoprobe analysed using (D) fitting and (F) CMM. Phasor plots for HEK293 and PC3 with nanoprobe are shown in (K) and (L), respectively. Images (G) and (H) represent the results after applying phasor gates, as indicated by the green areas in (K) and (L). The time-resolved fluorescence data is displayed in (I), illustrating the IRF in black, HEK293 incubated with nanoprobe in blue, and PC3 incubated with nanoprobe in red. Finally, (J) shows the τ_{CMM} distribution of HEK293 incubated with nanoprobe in blue and PC3 incubated with nanoprobe in red.

Table 3 Speed and calculated lifetime comparison between the fitting method (τ_{FIT}), the centre of mass method (τ_{CMM}) and the phasor plot.

Method	HEK293 with nanoprobe (τ_{HEK293})		PC3 with nanoprobe (τ_{PC3})	
	Calculation time (s)	Lifetime (ns)	Calculation time (s)	Lifetime (ns)
τ_{FIT}	1,206.72	0.21 ± 0.02	1,178.73	0.27 ± 0.11
τ_{CMM}	0.14	0.93 ± 0.02	0.15	1.25 ± 0.43
Phasor plot	0.07	Bottom right corner	0.10	The middle and bottom right corner

In addition, these measurements have a poor IRF profile as indicated by the black line in Figure 3.12(I) which shows extra multiple peaks after the main peak. This indicates internal reflection and scattering within the optical path that influences the measurement as indicated by the red and blue line in Figure 3.12(I). Our software has implemented IRF subtraction which has been described by Equation 2.12 to reduce the effect of IRF.

3.5 Conclusion

Overall, we have built a rapid and reliable tool for routine FLIM analysis, which can rapidly distinguish between healthy and cancer cells. CMM and phasor analysis have speedy performances and superior clarity than intensity imaging and are theoretically faster than traditional fitting methods, as our method does not require model selections or require setting extra constraints as most traditional analysis tools do [59]. This method only takes less than a few seconds to generate fluorescence intensity and lifetime images with corresponding lifetime distribution and phasor plot. The speed can be further improved with a faster CPU. Moreover, the direct estimation algorithms are hardware-friendly, offering even much faster analysis if they are implemented in electronic hardware [81], [92]. Different tools provide their own strategies for selecting areas of interest, but they do not offer comparable speedy analysis. From the experiments and the analysis conducted, the time-resolved fluorescence imaging or analysis using the RNA nanoprobes allows the differentiation of cancer and non-cancer cells from their lifetimes. The imaging platform, as well as the tool developed, can be widely applied in research conducting FLIM measurements.

Chapter 4 Characterisation of the SPAD Sensor

4.1. Introduction

Typical time-resolved flow cytometers utilise high-performance single-photon detectors, such as PMT, in combination with a TCSPC channel to collect the timestamp of each incoming photon. Generally, PMT is a vacuum tube with a series of dynodes, which involves a chain amplification of electrons that are first generated from the photocathode when a single photon arrived. Even though PMT provides good sensitivity with low noise, it needs a cooling system to reduce the dark count rate [93] and has a fragile and bulky design that is not possible to assemble into arrays. It can also be affected by radio frequency (RF) interference causing small periodic peaks in fluorescence time-resolved data. Furthermore, this configuration is often limited by several factors, including the limited photon bandwidth resulting from the limited number of TCSPC channels, the limited sampling rate caused by dead time and photon pile-up prevention, and the large size, complexity, and high cost of the entire system.

Recent advancements in 40 nm CMOS fabrication technology have enabled the implementation of large-scale arrays of SPADs and TCSs in a pixelated sensor chip. This approach allows for independent parallel processing of pixels and an increase in photon bandwidth. Additionally, SPADs provide the benefit of low dead time, resulting in a higher overall data acquisition rate, with sampling capabilities up to the GHz level [94]. The SPAD also allows compact experimental setup with low power consumption, and these enable the possibility of constructing an integrated system [95]. However, one drawback of this approach is the low fill factor, as a significant portion of the pixel area is allocated to electronic circuit components [47], [96].

SPAD is a photodiode that detects single photons with high efficiency. The working principle of SPAD is described by the current and voltage plot in Figure 4.1. It comprises a reverse biased p-n junction at high voltage with an excess bias voltage of V_{EX} above the junction breakdown voltage (V_{BD}). In case of no arrival photon, the SPAD characteristic is similar to a typical diode, which blocks reverse current flow across the p-n junction. This situation is called “off-state” indicated by Figure 4.1(A). The SPAD moves to “on-state” when a single photon arrives in Figure 4.1(B). Due to the strong internal electric field, the single arrival photon can create an electron-hole pair, which can trigger a self-sustaining avalanche of secondary carriers resulting in the generated current suddenly rising within sub-nanosecond

time, until the whole volume of the diode is activated. The current continues until bringing the bias voltage down to or below the breakdown voltage through the quenching circuit until the carriers are no longer accelerated by the electric field as shown in Figure 4.1(C). The SPAD will be able to detect the new arrival photon when it is re-biased again above the breakdown. During the quenching and re-biased process, the SPAD cannot detect the new incoming photon.

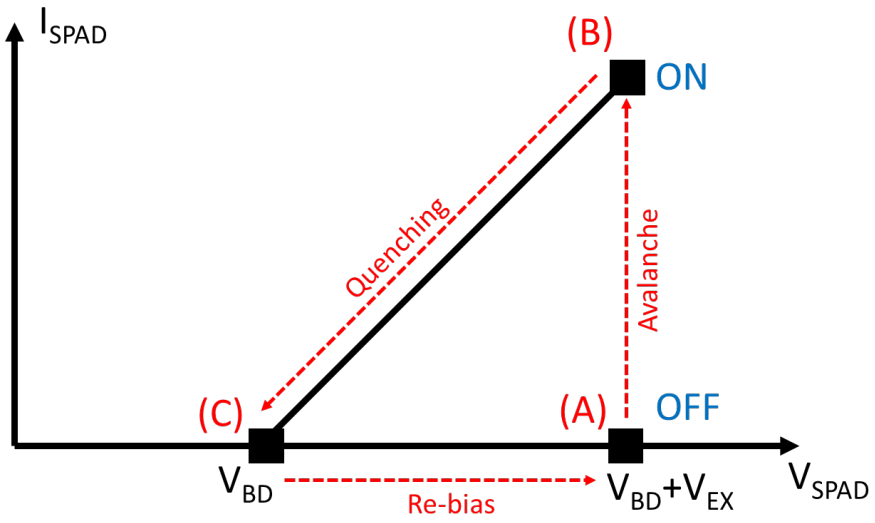

Figure 4.1 Current-voltage characteristic of the SPAD showing the working operation between on- and off-state as a cycle. The process begins from (A) where the SPAD is reversely biased with $V_{BD}+V_{EX}$ indicating the off-state of the SPAD. After single photon absorption, the avalanche has been triggered, which moves the SPAD to (B) the on-state. The quenching circuit brings the V_{SPAD} to (C) once the timing electronic has sensed the avalanche current. The next incoming photon can be detected after the SPAD has been re-biased to (A).

Single photon counting detectors are a crucial component in fluorescence lifetime measuring applications. These detectors use timing electronics to convert photons into a time difference between the laser trigger signal and the arrival time of the photon. In this particular study, a 192x128 TCSPC SPAD imager array, utilising STMicroelectronics 40-nm CMOS technology, was used to capture single photons and construct fluorescence decay. The sensor was configured as a megapixel detector, which operates in a cycle of detection and reset, allowing for the simultaneous detection of 24,576 photons in parallel. Despite this', the sensor's performance is limited by factors such as high dark count rates, bad pixels, and non-uniform timing. As a result, sensor calibration was performed prior to measurement.

4.2 The SPAD camera

In this section, the multi-channel TCSPC camera designed for wide-field FLIM will be modified for the FCM measurement. The camera components and characterisation are described later below in order to verify the compatibility with the developing lifetime FCM system.

4.2.1 The SPAD chip

The SPAD array sensor used in this work is manufactured by STMicroelectronics [47]. The chip design is based on a 192x128 pixel array of SPAD with a 12.4% fill factor. Each pixel is integrated with a 5.4 µm diameter SPAD with built-in TDC, while the pixel pitch is 18.40 µm x 9.20 µm contributing to a 3.2 x 2.4 mm total sensor area (Figure 4.2). This SPAD has been reported as having a peak sensitivity of 34% at 560 nm. The device is designed to amplify the single photon count and convert it to an electric signal. The sensor has two modes of operation (1) photon counting mode (PC mode) which measure intensity, and (2) time-correlated single photon counting mode (TCSPC mode) which measures the arrival time of incoming single photon.

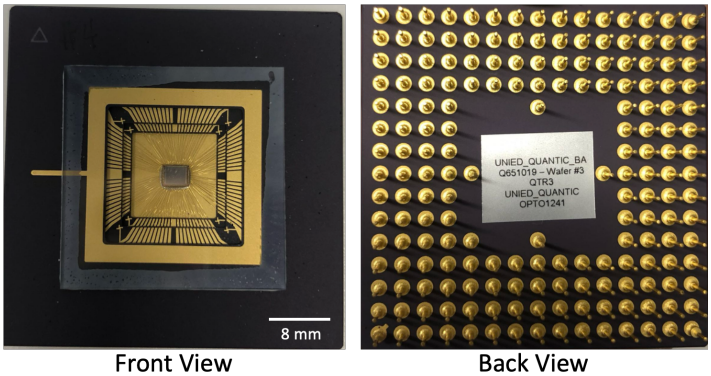

Figure 4.2 Front and back view of the sensor array

4.2.2 Camera component

The camera is composed of three main components: FPGA board, printed circuit board (PCB) and SPAD chip (Figure 4.4). The PCB is a bridge between the SPAD chip and the FPGA in the communication and power supply of the chip. The PCB consists of 6 layers with 148 mm x 103 mm outer dimensions. A 15x15 pins IC socket is used to mount the SPAD chip, while two 80-pin ports on the backside connect to FPGA. The FPGA board (XEM6310-LX150, Opal Kelly, USA) requires a 5V supply cable for operation and a fast USB 3.0 cable for PC communication. The PCB and sensor power are supplied from the FPGA. The SYNC port is configured to accept NIM pulse from the laser driver through an SMA-BNC-Lemo00

adapter and delay generator. The NIM pulse standard is a digital signal described by 0 V for the low state and -1 V for the high state. The TDC voltage is set to 1.2 V to adjust the TDC resolution (bin width) to 39.7 ps (Figure 4.3).

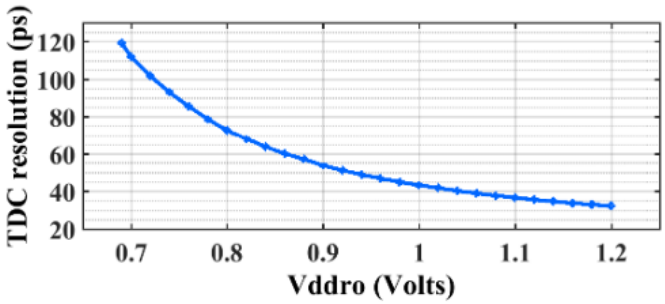

Figure 4.3 TDC resolution against supplied voltage, reported from [47], [97]

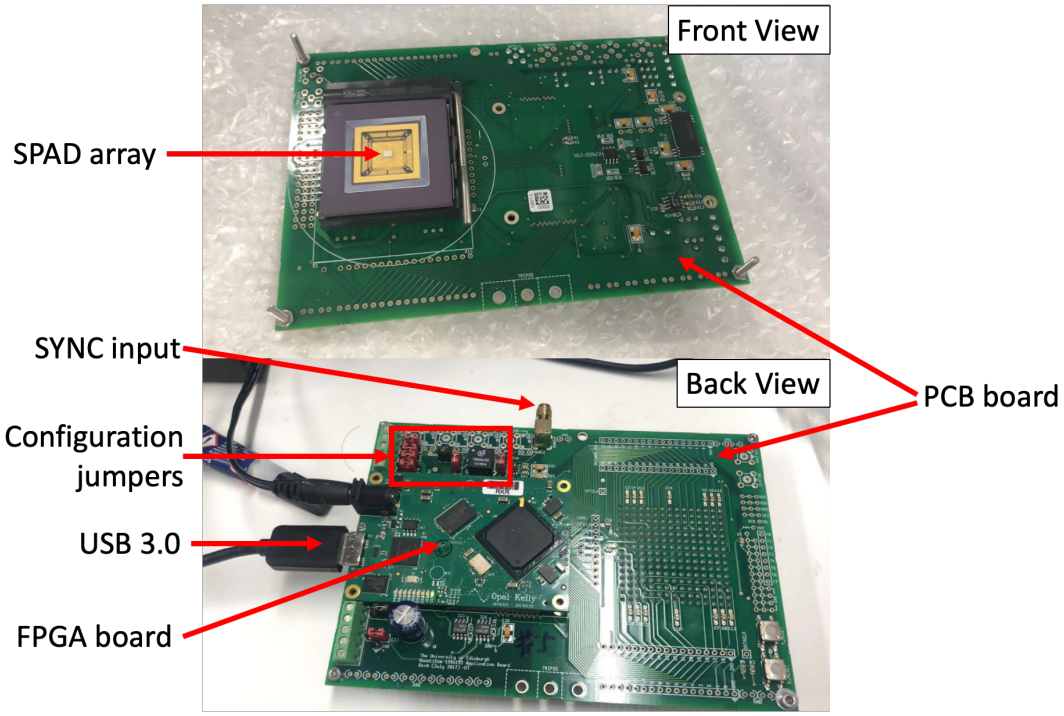

Figure 4.4 Front and back view of the SPAD camera with 192x128 SPAD array implemented with 12-bit TDC image sensor.

4.2.3 Sensor operation

The SPAD uses firmware, which serves as a bridge between the camera and MATLAB code, which was originally developed by a collaborator at Edinburgh University [47]. All pixels are read and reset in a global shutter mode. The camera is designed for real-time detection with a tuneable measurement speed of up to 54 µs per frame, excluding data transfer and analysis time. In TCSPC mode, a STOP pulse is synchronised with the external trigger signal provided

by the laser driver box. Signals in the camera are distributed to the entire array through a clock tree as shown in Figure 4.5. A single frame is defined as the measurement performed in the exposure period. The WINDOW signal is enabled during short sub-periods of the laser cycle to provide an electrical masking signal to control overall exposure or global shutter. The S signal indicates the enable signal for the TDC (0 = TDC off, 1 = TDC on), which only operates when the rising edge of the SPAD pulse is located within the high-state period of the WINDOW signal. The S signal is reset on every rising edge of the STOP signal. Additionally, only the first photon that meets these criteria will be captured within an exposure period, which refers to the period between frames.

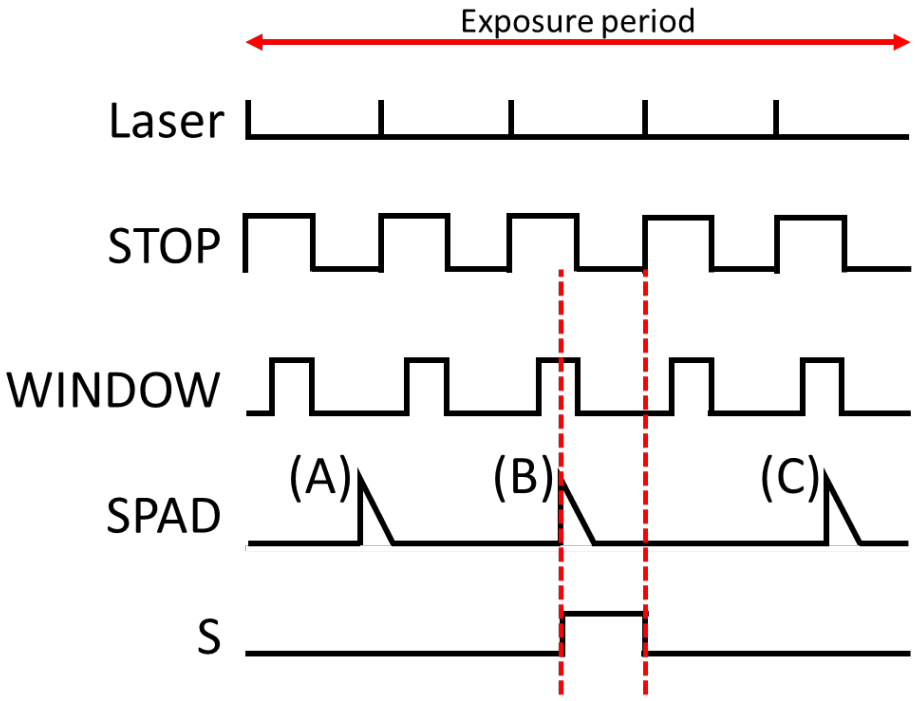

Figure 4.5 Clock diagram showing the sensor operation in TCSPC mode within the exposure period where (A) is a photon appearing outside the WINDOW, (B) is the first photon in the WINDOW that starts the TDC, and (C) is the subsequent photon incoming photon in the same exposure period, which is ignored. Laser is the signal provided externally by the laser driver. The rising edge of the STOP signal is synchronised with the Laser signal, which is used to reset the TDC state back to 0. The WINDOW signal is an electrical mask for controlling the acquisition time for detecting a photon between laser pulses. SPAD signal indicates the SPAD current when the avalanche is triggered. S signal indicates the status of TDC where the sensor only records the data when S is 1.

4.2.4 Data format

The SPAD camera utilises USB 3.0 communication and firmware implemented on an FPGA chip to connect with a PC. However, it also has limited capabilities for flow cytometry applications as it can only extract data from a single frame and the data is encoded and uncalibrated. Thus, modifications and characterisation of the SPAD sensor are necessary to achieve optimal settings for lifetime measurement applications.

After the sensor performs a measurement, the sensor readout is a 2D matrix containing the time bin number of the single detected photon. However, the data is required to convert from encoded to readable values. The sensor readout format is in 16-bits per pixel, but the TCSPC data word is only within 12-bit least significant bits (LSBs) of the 16-bit data. The other 4-bit most significant bits (MSBs) are neglectable and not related to TCSPC data. This data processing is a step-by-step process including hex-to-binary digit conversion, removing MSBs, and binary-to-decimal digit conversion, respectively.

4.3 Megapixel integration

We have developed new methods to improve the performance of the SPAD cameras for FCM applications, called megapixel integration, which greatly improves the photon bandwidth and reduces the number of data acquisition of the sensor. Figure 4.6 is a diagram showing the idea of the megapixel integration method. The default configuration of SPAD cameras is designed for imaging, where each pixel functions as a single photon detector with a bandwidth of one photon per measurement. However, this configuration may not be suitable for FCM applications that require maximum photon bandwidth without the need for images. To address this limitation, the megapixel method is performed by combining all pixels into one large pixel with a large bandwidth of 24,576 photons per measurement and known arrival times of each photon. Despite the large photon bandwidth, the TDC in each pixel may exhibit different response times, noise levels, linearity, and gains due to manufacturing uncertainties. These are non-linear characteristics related to dark count rate, after pulse, integration time, jitter and optical crosstalk [98]–[102]. To overcome this challenge and generate more accurate TCSPC data, each pixel must be aligned using its peak position of the IRF and bad pixels must be masked out. The system only requires a one-time calibration, where all calibrating parameters are saved as predefined values for later rapid calibration.

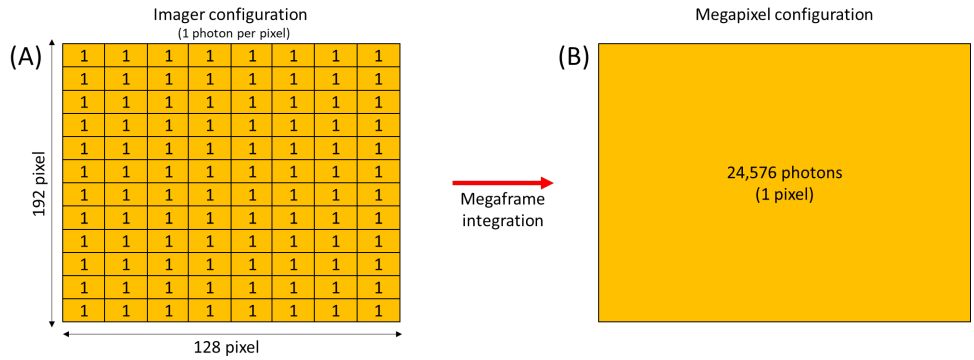

Figure 4.6 Megapixel integration principle. (A) The SPAD array is configured as an imager where each pixel separately counts the single arrival photon. (B) The SPAD array is configured as a megapixel which integrates every pixel into one pixel with a bandwidth of 24,576 photons.

4.3.1 IRF measurement and time alignment between pixels

The response of electronic devices was characterized using a 640 nm pulsed laser (DD-635L, Horiba, UK) driven at a 10 MHz repetition rate. The laser beam fully covers the area of the SPAD through a 3.0 ND filter, as shown in Figure 4.7. The SPAD camera is configured in TCSPC mode, with an exposure time of 1 ms, and 30,000 frames were recorded. All frames are combined to accumulate enough photons per pixel to generate the fluorescence decay for each pixel. Only photons with arrival times between the 2000th to 4000th bins are counted to reduce the amount of data in this analysis.

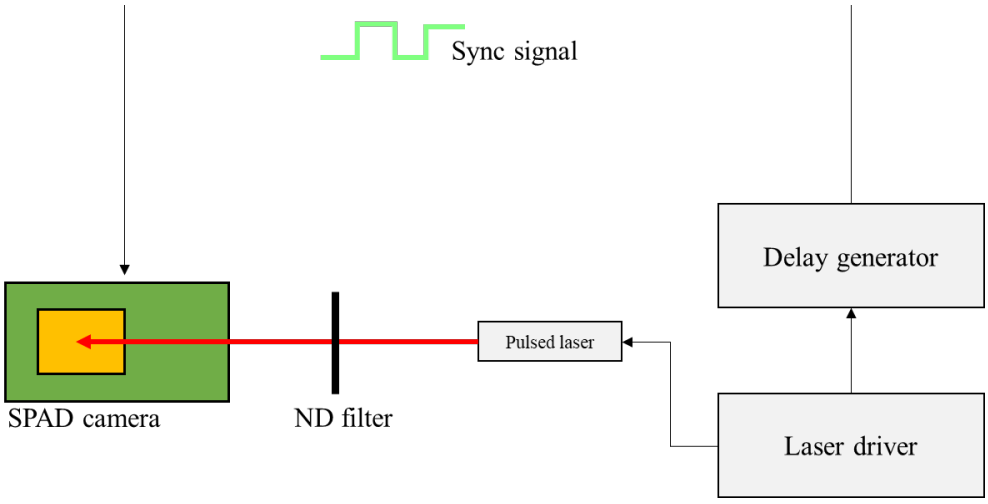

Figure 4.7 Experimental setup for the time-alignment process. All pixels are illuminated by a pulsed laser through a natural density (ND) filter to prevent the overflow effect from intense light. The response time of each pixel is measured from the time difference between the signal from SPAD and the sync signal from the laser driver.

As shown in colour-coded Figure 4.8(A), the SPAD array's pixels exhibit varying response times, with the top-right area having a faster response time (indicated by the blue colour) compared to the bottom-left region (indicated by the red colour). To further illustrate this, Figure 4.8(B) displays the normalised time-resolved data of five randomly selected pixels from the top-left, bottom-left, centre, top-right, and bottom-right regions. The fastest response pixel was found at coordinates (x = 91, y = 11) with a peak position of 2053rd bin, while the slowest response pixel was located at (x = 4, y = 178) with a peak position of 2838th. The difference in response time between these two pixels is 785 bins or 31.16 ns, indicating that integrating multiple pixels will result in a broadening of the overall time-resolved data.

In order to achieve identical response times for all pixels in the SPAD array, a time alignment process is necessary. This can be accomplished through the use of a custom MATLAB code that utilises a shift map, where the value is calculated by subtracting 2735 from the peak position of each individual pixel (as shown in Figure 4.9(A)). The number 2735 corresponds the time bin when the stop signal reaches the camera. The shift map is represented by Equation 4.1, where *i* and *j* represent the pixel position.

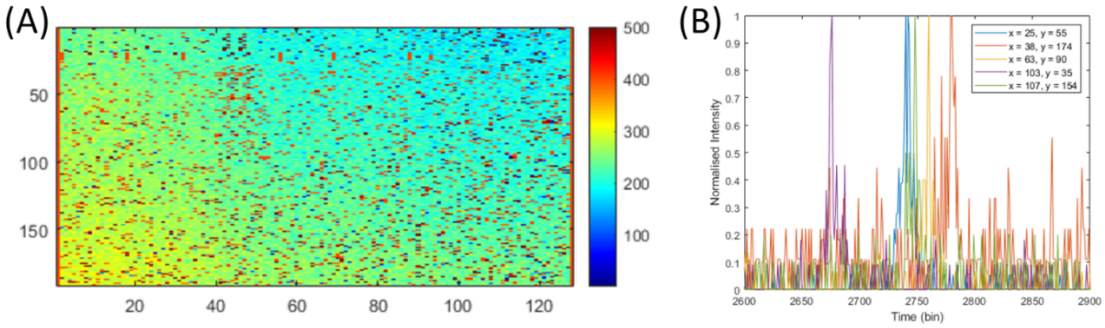

Figure 4.8 (A) is a colour-coded image of the peak position of time-resolved data recorded from the SPAD camera. The peak position is ranging from 2600th (blue) to 2900th (red) bin. The black pixel indicates the pixels without observed response function peak. (B) normalised time-resolved data acquired from five random pixel from top-left (x = 25, y = 55), bottom-left (x = 38, y = 174), centre (x = 63, y = 90), top-right (x = 35, y = 103), and bottom-right (x = 107, y = 154).

$$shift\ value\ (i,j) = 2735 - peak\ position(i,j) \tag{4.1}$$

The time alignment process is implemented by adjusting the time-resolved sensor readout for each individual pixel, as illustrated in Figure 4.9(B). Positive values in the shift map indicate that the corresponding pixel has a fast response time, and a positive time delay will be added to shift the time-resolved data to the right. Conversely, negative values indicate a slow

response time and a negative time delay will be added, resulting in a left shift of the time-resolved data. After the alignment process, a uniform response time across the sensor is observed, as indicated by the response function peak position shown in Figure 4.9(C). The colour-coded image generated from the response function peak after the time alignment shows that the majority of the response function peaks are centred around the 2735th bin.

As depicted in Figure 4.10, the IRF of a megapixel detector was analysed before and after time alignment. The results indicate a significant improvement in the IRF profile following alignment. Specifically, the peak of the IRF was observed at the 2720th bin with 59,823 counts and a full width at half maximum (FWHM) of 3.02 ns prior to alignment. However, after alignment, the peak of the IRF was observed at the 2735th bin with 171,801 counts and an FWHM of 0.44 ns. The aligned IRF exhibits a more delta-function-like profile, as opposed to the uncalibrated one. This can lead to a reduction in the complexity when performing fluorescence lifetime analysis [2].

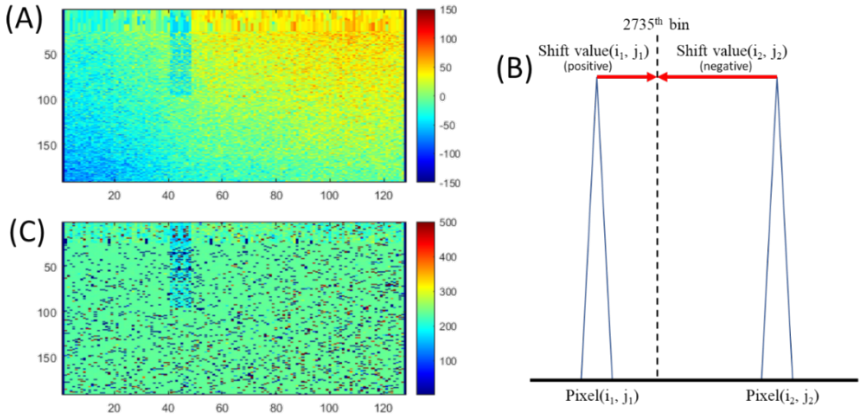

Figure 4.9 (A) shift value map of the SPAD array and (B) colour-coded image of the peak position of time-resolved data recorded from the SPAD camera after time alignment.

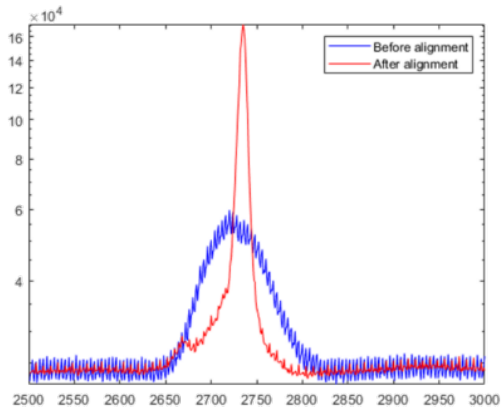

Figure 4.10 IRF of megapixel from the single frame before and after alignment.

4.3.2 Bad pixel removal

Although time alignment has been applied all-over the SPAD arrays, there are still some pixels randomly displaying not calibrated response time. Moreover, some pixels also do not function properly on intensity and time measurement. These bad pixels in SPAD arrays can affect the accuracy of time and intensity measurements. The origin of the bad pixel can be described by defects in the semiconductor material, issues with the fabrication process, or damage to the device during use. In order to perform megapixel integration, data from bad pixels must be ignored. In this study, bad pixels are categorised into three types: dead, hot, and noisy pixels, which are characterised by measuring dark counts or measuring a known lifetime reference dye such as fluorescein. Dead pixels cannot detect photons or have very low sensitivity, hot pixels always show detected photons even without any light source, and noisy pixels have high background appearing in every time bin, decreasing the precision of measurement. Good pixels, on the other hand, are normal pixels that can detect photons with correct time-resolved data. In this section, we aim to generate a bad pixel mask which can remove the signal from the bad pixel as much as possible by using dark counts (background measurement) and reference dye measurement.

4.3.2.1 Background measurement

To locate hot pixels in an SPAD camera, the camera is placed in a dark room and connected to an external NIM sync signal that provides a 10 MHz trigger signal. The camera is then set to TCSPC mode, and a measurement is taken for 100,000 frames. The intensity of each pixel is calculated from all photons that appear in bins 2001 through 4000. A colour-coded intensity image of the background measurement (Figure 4.11A)) is generated, with black pixels indicating low-intensity levels, red pixels indicating a low-mid level of detected photons, and yellow and white pixels indicating hot pixels that always or often show detected photons even in the background measurement. An intensity histogram (Figure 4.11(B)) is generated from the intensity image, revealing two majority groups of pixels: those with very low intensity (below 20,000 counts) and those with always high photon counts (more than 80,000 counts). To identify hot pixels, a threshold of 20,000 background counts from 100,000 measured frames or a detection rate of more than 20% in background count is used. A hot pixel mask (Figure 4.11(D)) is then created, indicated by yellow-coloured pixels. After the

mask is applied, the hot pixels are mostly removed, as shown in the final image (Figure 4.11 (C)). Overall, 2,488 hot pixels are found which is 10.12% area of the SPAD camera.

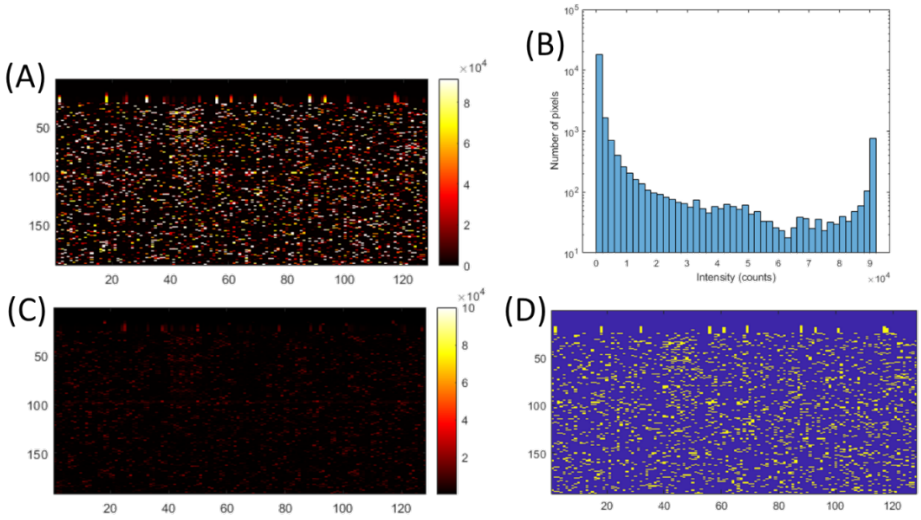

Figure 4.11 Background intensity image before (A) and after (C) applying hot pixel mask. (B) Background Intensity histogram and (D) hot pixel mask

4.3.2.2 Reference dye measurement

However, there are also other types of pixels such as dead and noisy pixels that can influence the lifetime precision and accuracy. In order to find these pixels' positions, a fluorescence lifetime measurement of fluorescein dye, as a standard fluorophore, is performed to characterise the SPAD camera. This dye exhibits a high quantum yield, mono-exponential with a 4 ns fluorescence lifetime [8], [103].

4.3.2.2.1 Reference dye preparation and characterisation

Prior to this measurement, the fluorescein solution was prepared by dissolving fluorescein powder in distilled water to obtain a concentration of 10 µM. The appropriate excitation and emission wavelengths were selected based on the colour-coded emission profile, which was measured using the Flurolog-3 fluorescence spectrometer and analysed using Origin 2021 software. The fluorescence intensity profile of the fluorescein solution was obtained using the 3D measurement mode of the Fluorolog-3 spectrometer. This mode allows for continuous measurement of the intensity while varying the wavelength of excitation and emission. The fluorescence intensity profile of fluorescein, as shown in Figure 4.12, reveals that the emission intensity reaches a maximum value of 10^7 counts per second (cps) in the range of

480 nm to 495 nm for excitation and 510 nm to 525 nm for emission. This highlights the optimal range for excitation and emission for this fluorescein solution.

The reference lifetime of fluorescein dye can be measured using a Horiba DeltaFlex fluorescence lifetime spectrometer (Figure 4.13). In this case, a 10 µM solution of fluorescein is excited by a 482 nm pulsed laser operating at a 25 MHz repetition rate. The emission is collected through a 505 nm long-pass filter for 29.57 seconds in order to achieve 10,000 peak counts. The lifetime analysis is performed using DAS6 software by fitting the fluorescence decay with a mono-exponential model, which yields a lifetime of 4.06 ± 0.02 ns with a $\chi 2$ value of 0.97. However, it should be noted that this analysis process is tail fitting, which is performed by neglecting the instrument response function (IRF) due to the fluorescein decay being affected by laser leakage and radio frequency (RF) interference, as evidenced by a small periodic peak in the decay plot.

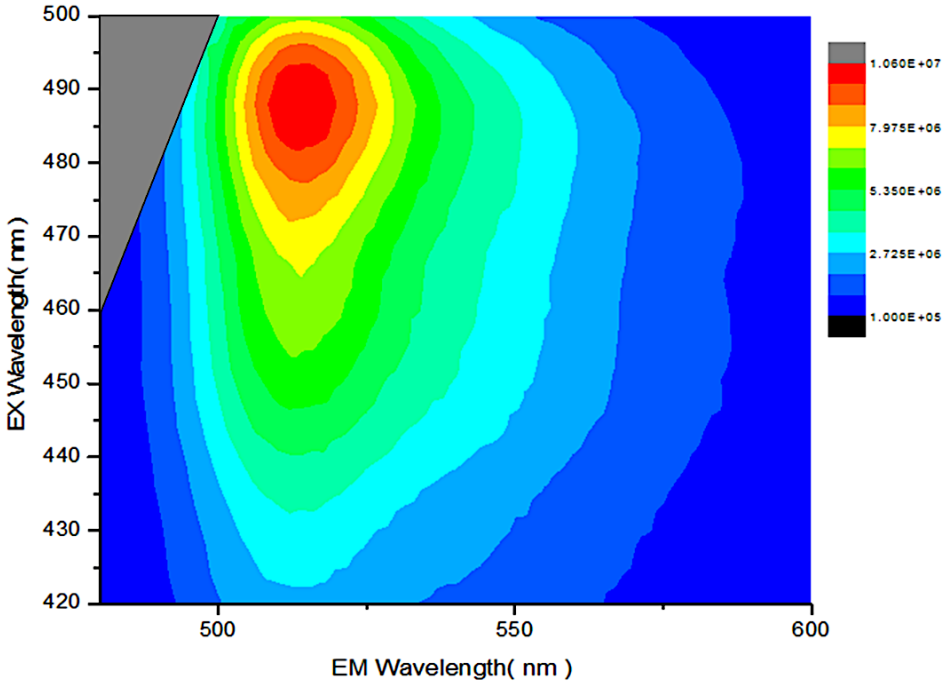

Figure 4.12 A map displaying color-coded fluorescence emission intensity in relation to the fluorescence emission (x-axis) and excitation wavelengths (y-axis) of fluorescein, measured using Fluorolog-3.

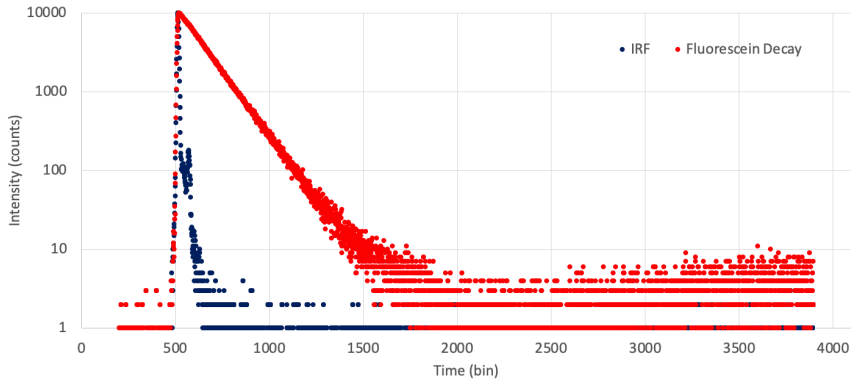

Figure 4.13 IRF (blue) and fluorescence decay of fluorescein (red) measured from Horiba DeltaFlex

4.3.2.2.2 Reference dye measurement using SPAD camera

Figure 4.14 illustrates the experimental configuration utilised for the determination of the fluorescein lifetime using a SPAD camera. The sample solution, consisting of fluorescein, is contained within a 4ml plastic cuvette and positioned at a 90° angle relative to the direction of excitation. Excitation of the fluorescein is achieved through the utilisation of a pulsed laser, operating at a wavelength of 470 nm and a repetition rate of 10 MHz. The fluorescence signal is then collected by the SPAD camera via a 505 nm long pass emission filter. To acquire a sufficient number of photons per pixel for the calculation of the fluorescence lifetime, the measurement was performed by integrating 10,000 frames with an exposure time of 1 ms.

Figure 4.16 illustrates the experimental results of the fluorescein sample, showing both the (A) intensity and (B) lifetime measured from the SPAD camera. An analysis of the data reveals that the majority of the pixels within the array exhibit fluorescence intensities ranging from 2,600 to 3,800 counts per pixel and a lifetime of 4 ns. For analysis of individual pixels, the fluorescence decay of each pixel is divided into two sections (Figure 4.15). Background window is a window of 500 bins from 2201st to 2700th bin before raising edge of the fluorescence decay to ensure that the signal appearing in this window is only from dark counts. Background value is calculated from the average number of photons per time bin in the background window, which indicates how much noise each pixel has. The fluorescence lifetime analysis was performed by applying the time-alignment technique previously mentioned to all pixels and performing CMM analysis within measurement windows of 400 bins from bins 2911 to 3310, beginning at the decaying peak, which corresponds to four times the expected lifetime of fluorescein, which is minimum measurement window width required by CMM with LUT (Equation 2.9). The lifetime error value is determined based on

the standard deviation of the lifetime distribution across all pixels. Furthermore, the analysis reveals the presence of abnormal pixels within a T-shaped region (y = 1 to 20 for any x position, and y = 21 to 96 for x = 41 to 48), which displayed abnormal lifetime characteristics and weak intensities. Additionally, it is observed that the pixels located in the middle row (y = 97 and 98) display a higher sensitivity with correct lifetime values, as indicated by the red horizontal line of intensity levels between 5,500 to 7,000 counts. In contrast, the pixels located at the right (x = 1) and left (x = 128) edges exhibit the least sensitivity, with the ability to detect incoming photons at levels of less than 1,000 counts, as depicted by the dark-blue vertical line in the intensity image.

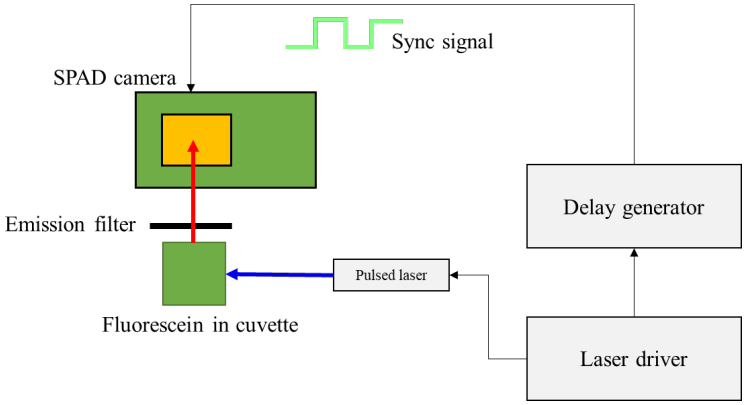

Figure 4.14 Experimental setup for finding bad pixels. The SPAD array measures the fluorescence signal through an emission filter from fluorescein in a 4 ml standard cuvette excited by a pulsed laser. The fluorescence decay of each pixel is generated and analysed by the CMM method.

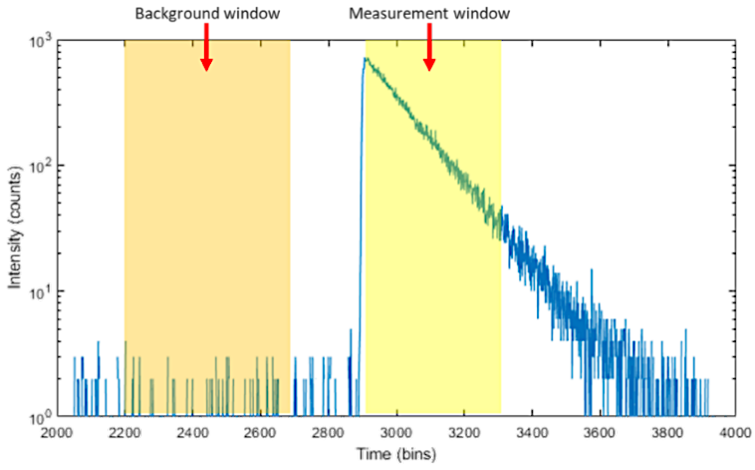

Figure 4.15 Fluorescence decay of fluorescein from a single pixel showing the decay peak position at 2911th bin. The yellow area is the measurement window from the 2911th to 3310th bin. The orange area is the background window from the 2201st to 2700th bin.

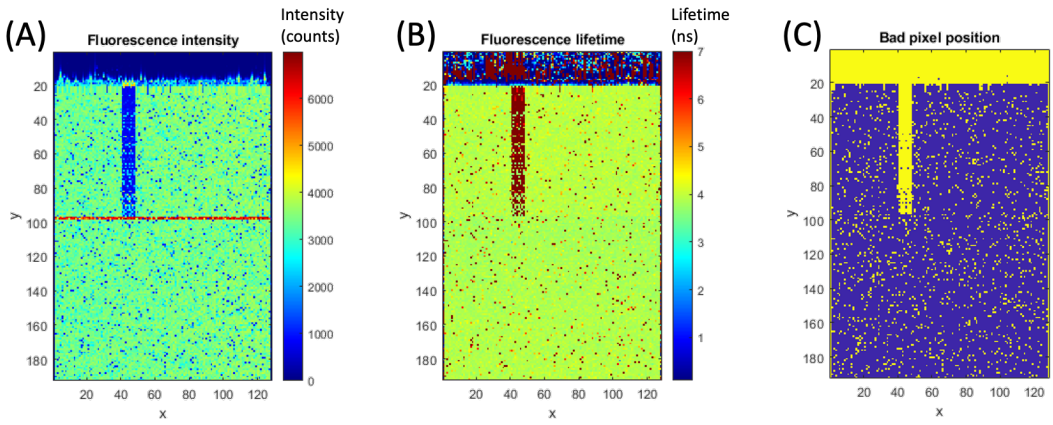

Figure 4.16 Information from the SPAD array analysed by the CMM method. (A) colour-coded fluorescence intensity image where red is high, while blue is low intensity. (B) colour-coded fluorescence lifetime image where red is long, while blue is a short lifetime. (C) Bad pixel mask where yellow pixel indicates the bad pixel position

Figure 4.17 illustrates the relationship between various evaluation parameters, including fluorescence intensity, lifetime, and colour-coded background, as generated from the fluorescein dye measurement depicted in Figure 4.16. Overall, there were 19,394 good pixels out of a total of 24,576 pixels, representing 78.91% of the total SPAD area. A good pixel is defined as a pixel with a lifetime between 3.6 and 4.2 ns, an intensity greater than 2,600 counts, and a background less than 1.5 per bin per pixel, as depicted in Figure 4.17(B). Pixels that do not meet these criteria are considered to be bad pixels. There were 1,449 hot pixels (Figure 4.17 (A)), which are clearly visible in the high intensity and short lifetime region. These pixels also exhibit abnormal time-resolved data due to malfunctioning TDC. Figure 4.17(D) confirms that the 381 pixels at the left and right edges are unable to detect any fluorescence decay and consistently exhibit a noisy signal. 2,021 dead pixels, with intensities less than 100 counts, appear randomly throughout the sample and are insufficient for histogramming and lifetime calculation. The remaining 1,328 pixels are considered to be noisy pixels, with a background greater than 1.5 per bin per pixel. The CMM process is sensitive to noise and is affected by the high noise level in noisy pixels, resulting in an increased lifetime, as shown in Figure 4.17(C). By combining the bad pixels acquired from the reference dye measurement with the bad pixels from the background measurement (Figure 4.11(D)), a bad pixel mask can be generated, as depicted in Figure 4.16(C). In total, there were 5,182 bad pixels, indicated by yellow-coloured pixels, distributed throughout the SPAD sensor.

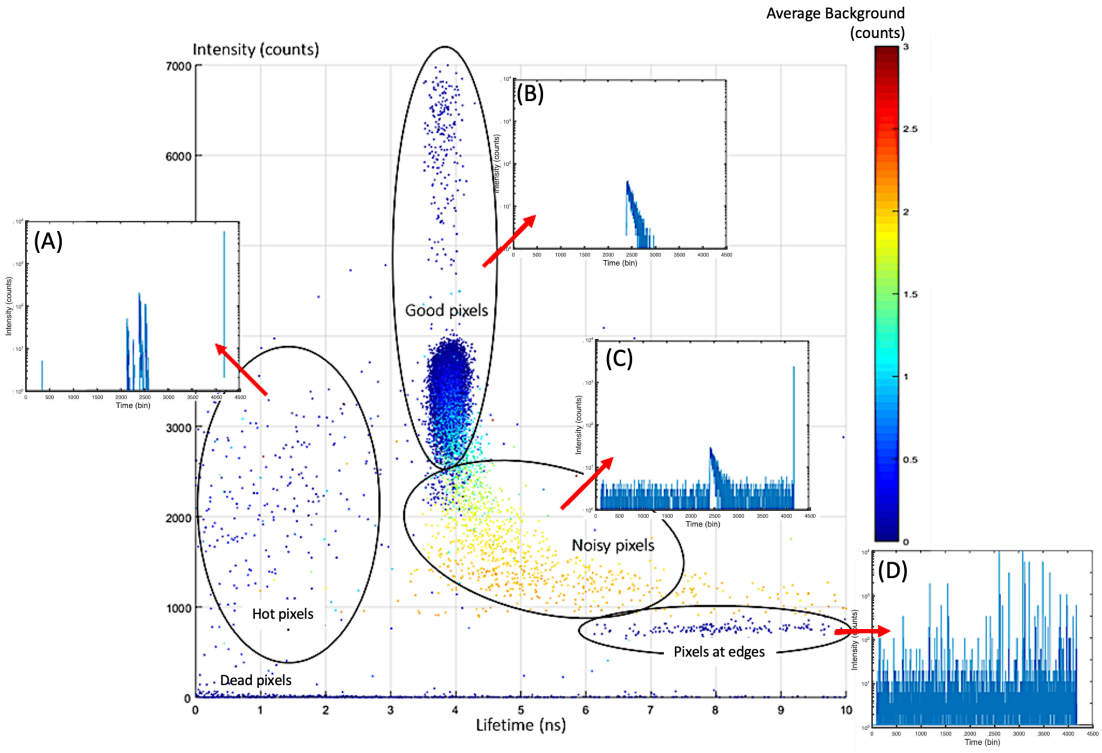

Figure 4.17 A plot of three parameters where the y-axis indicates fluorescence intensity, the x-axis shows fluorescence lifetime and the coded colour shows the average photon per bin calculated from the background window. Pixels can be categorised into four types: (A) hot pixel, (B) good pixel, (C) noisy pixel and dead pixel. The plots of (A - D) are fluorescence decay where y-axis is intensity (count) and x-axis is time (bin). Due to manufacturing defects, the pixel at the left and right edges are damaged and cannot detect any signal (D).

4.3.3 Relation between background level and the exposure time

As shown in Figure 4.17(C), a noise level exceeding 1.5, indicated by a colour range from green to red, can significantly affect the accuracy of fluorescence lifetime detection, leading to significantly prolonged lifetimes. Specifically, the lifetime of fluorescein can be overestimated by as much as 6 ns when the noise level is high. This highlights the sensitivity of CMM to noise level and measurement window width [54], as the signal-to-noise ratio (SNR) is inversely proportional to the square root of the number of detected photons [59]. To improve the accuracy of fluorescence lifetime estimation in megapixels, a background subtraction process is necessary. This can be achieved by determining the background value of the megapixel within the background window and subtracting this value from the overall measurement. The SPAD sensor should be placed in a dark room to measure dark counts, and the exposure time is varied from 0.5 to 3 ms. Additionally, the sensor is configured as a megapixel using TCSPC mode with an internal stop signal, and the STOP trigger signal

should be provided from the internal circuit of the camera. Figure 4.18 is the amount of average background measured from 1,000 continuative frames after the bad pixel mask and the response time alignment have been applied. The exposure time is set to 0.5, 1.0, 1.5, 2.0, and 2.5 and 3.0 ms giving the background level of $0.34 \pm 3.9\times10^{-4}$, $0.55 \pm 7.9\times10^{-4}$, $0.72 \pm 27.20\times10^{-4}$, $0.86 \pm 30.32\times10^{-4}$, $0.98 \pm 12.82\times10^{-4}$, and $1.08 \pm 22.62\times10^{-4}$ counts, respectively. The amount of background in the megapixel image can be directly compared to the exposure time setting, providing a clear understanding of how to optimise the background subtraction process to improve the accuracy of fluorescence lifetime estimation.

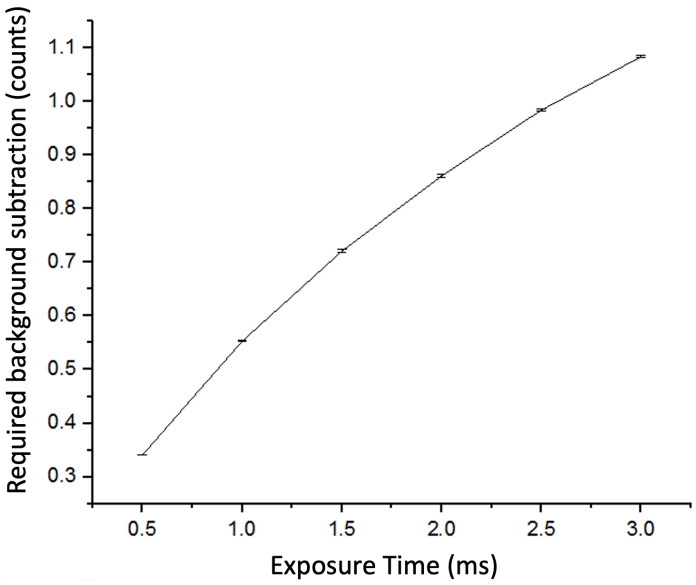

Figure 4.18 Amount of required background subtraction of megapixels compared to the exposure time.

4.4 Comparing fluorescence decay before and after the correction process

We have developed a correction method that allows us to have high confidence in the accuracy and precision of the sensor, enabling us to obtain reliable and high-quality data from the SPAD camera. The correction process composes of three steps described in earlier sections including (1) artificially making the ideal response time of the SPAD array, (2) filtering out the signal from bad pixels, and (3) subtracting the background to improve lifetime calculated by CMM method. This calibration process is performed only once, involving the collection and analysis of various parameters that are specific to the SPAD camera being used. The resulting calibration data is then saved as pre-set parameters for the correction process, which will be applied to all output obtained from the camera.

In this study, an experimental setup from Figure 4.7 is used to measure the IRF of a megapixel camera using a pulsed laser with wavelengths of 470 nm and 640 nm. The

measurements are conducted using 1,000 frames for each laser, which is enough to cover all samples used in the project. The resulting IRF measurements were displayed in Figure 4.19, which demonstrated a very narrow FWHM of 357 ps and 437 ps for the 470 nm and 640 nm laser, respectively, after correction. Additionally, to ensure the megapixel camera's ability to provide accurate TCSPC data, a measurement of fluorescein was conducted using the same experimental setup as outlined in Figure 4.14, which acquired 10,000 frames of fluorescein data from the megapixel. The results of this measurement were compared before and after correction, as depicted in Figure 4.20(A). The correction process led to a clear improvement in the fluorescein decay profile, with a clear rising edge and fewer abnormal high peaks caused by bad pixels. Moreover, an analysis is conducted on the uncalibrated and calibrated TCSPC data of fluorescein obtained from the megapixel, utilising the CMM method calibrated by IRF from the 470 nm laser. The lifetime error value is determined based on the standard deviation of the lifetime distribution across all detected events of megapixel. The results are presented in Figure 4.20(B), which described the lifetime distribution showing a lifetime of 4.75 ± 0.08 ns for the uncalibrated data and 3.85 ± 0.07 ns for the calibrated data. This demonstrated that the calibrated data yielded a measured lifetime that was in close range with the previously reported value of 4 ns[103] and 4.02 ± 0.02 ns from the reference dye measurement using Delta Flex. Furthermore, the calibrated megapixel is able to display the phasor plot of fluorescein on the semi-circle, indicating a mono-exponential decay profile (Figure 4.20(C)). In contrast, the uncalibrated megapixel camera displayed the position inside the semi-circle, suggesting a non-mono-exponential decay profile.

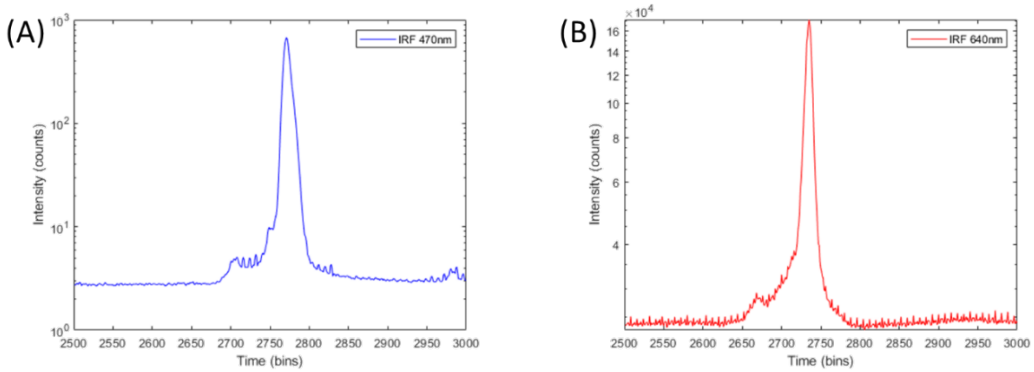

Figure 4.19 Calibrated IRF from the pulsed laser with (A) 470 nm and (B) 640 nm peak wavelength, driven at 10 MHz.

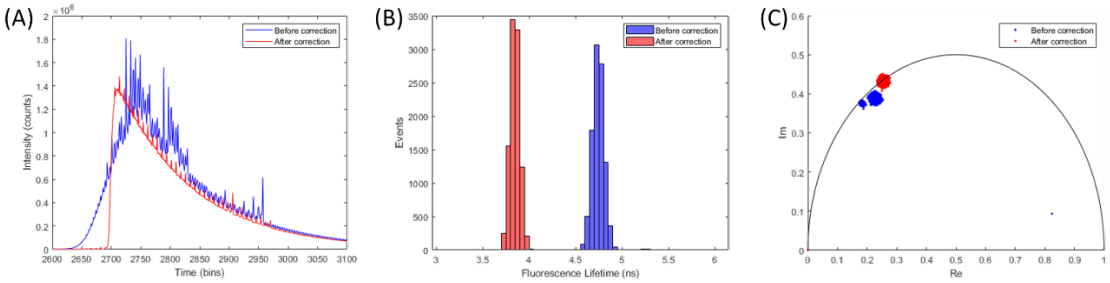

Figure 4.20 Fluorescence lifetime analysis of the fluorescein before (blue) and after (red) the correction process including (A) Fluorescence decay (B) Fluorescence lifetime calculated by CMM and (C) Phasor plot.

4.5 Conclusion

Overall, we have described the working principle of the SPAD arrays and how it is assembled into a camera, which requires multiple processes to get precise and accurate measurements. The novel development in this chapter is megapixel integration which combines every pixel into one (pixel) to generate a fluorescence decay profile and this greatly improves the photon bandwidth. However, due to the manufacturing defect, each pixel has its own timing response and some pixels are bad pixels. Therefore, a multistep correction process has been developed including a data decoding process, timing alignment, bad pixel mask and background subtraction. Furthermore, the calibrated SPAD camera has been tested with a reference dye showing a good agreement with the previously reported lifetime.

Chapter 5 Study and development of hydrodynamic focusing of FCM system

5.1 Introduction

In order to achieve single-particle detection and minimise the presence of multiple particles in a flow cytometer, a variety of parameters must be taken into consideration, such as particle density, viscosity, flow channel dimensions, and flow rate. To ensure that only a single particle is passing through the interrogation point, various methods for focusing or directing the flow of fluids or suspended particles can be employed. These methods include fluidic, acoustic, electric field, and magnetic field-based approaches, which allow for more precise data collection. One such method is dielectrophoresis, in which an electric field is used to move and focus particles or cells [104]. This effect is based on the particles' polarizability, which causes them to experience differing forces in the electric field, leading to the possibility of cell separation and purifying. Another method is acoustic focusing, in which sound waves generated from piezoelectric material are used to create pressure gradients that can be used to focus or direct the flow of particles or cells. This technique is often implemented in microfluidic devices for cell-sorting applications [105]. Magnetic focusing is another approach, in which the microfluidic channel is placed on a permanent magnet bed and the focusing effect is enabled by balancing magnetic and fluidic drag forces [106]. In comparison to other methods, hydrodynamic focusing has various advantages, such as it is less selective and does not require special properties of the sample. It is often simpler, less expensive, and can handle higher flow rates and larger fluid quantities [107]. However, the fluid's viscosity and other physical characteristics can have an impact on its ability to focus particles or cells of various sizes or densities.

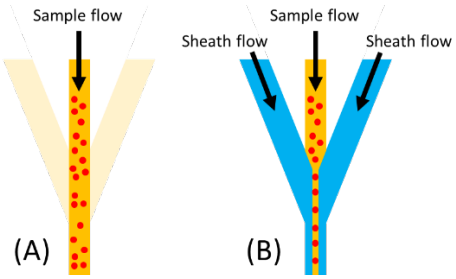

Figure 5.1 Hydrodynamic focusing effect when (A) no sheath fluid (B) with sheath fluid. By driving the sheath fluid, the sample is confined into a narrow stream with a dimension comparable to the cell dimension.

Hydrodynamic focusing is a technique to control a sample stream to deliver one particle or cell at a time passing the sensing volume where the measurement is performed. This is the principle behind the FCM by flowing two sheath fluids simultaneously with the sample at different speeds and the width of the centre cell stream is reduced to the cell diameter range. Figure 5.1 shows the hydrodynamic focusing effect where the fluidic input contains three inlets. The focusing effect occurs inside the enclosed flow cell where the sample and fast-flowing sheath fluid are injected. In the absence of the sheath fluid, the particle stream travels with the width of the flow cell and this can decrease the possibility of particles being detected (Figure 5.1(A)). In contrast, the stream is narrowed down to the particle's diameter by introducing the sheath fluid (Figure 5.1(B)). The narrowing effect is achieved by the side flow, which typically consists of water, PBS, or a control solution for squeezing the central flow. This can result in higher particle detection efficiency [22], [108]. There are several benefits of hydrodynamic focusing: (1) High-resolution and improved accuracy by precisely controlling the movement and position of the particles by adjusting flow rate (2) Particle separation for single particle detection and high-throughput application (3) Miniaturisation that the hydrodynamic focusing can be implemented in microfluidics devices enabling small, portable and easy to use system design (4) Hydrodynamic focusing is cost-effective and relatively simple and requires inexpensive technique.

Recent advancement in microfluidics technology allows the production of the compact, portable, and inexpensive flow cell of flow cytometry, where the fluidics channels are fabricated with a dimension of a few hundred microns [107]. This technique is necessary for high throughput applications for analysing and sorting DNA, proteins, or single cells in biomedical and clinical research such as drug delivery and discovery studies [109]. This method is also has been applied to environmental monitoring such as analysing microorganisms or pollutants [23] and testing food and beverage products [110].

The development of the fluidic system in the time-resolved flow cytometry has been described in this chapter including the design of the flow cell, implementation of hydrodynamic focusing, and characterisation with various fluorophores and fluorescent beads. Through investigations, the fluidics system can produce the hydrodynamically focused sample stream and the relation between sample and sheath flow rate can be determined. Furthermore, the performance of hydrodynamic focusing will be evaluated using fluorescent beads to confirm its ability to enhance the particle count rate. A discussion on the experimental setup, characterisation process, and results will be presented in the following sections of this chapter.

5.2 Flow cell

The flow cell in flow cytometry serves as the primary measurement chamber where individual cells or particles are detected. The flow cell is typically equipped with three inlet channels, including a sample channel and two sheath fluid channels for maintaining balance. Throughout the flow cell development, various configurations have been fabricated and used, including the double sheath chamber, the stream-in-air nozzle, the thin-walled capillary chamber, and the flow-through cuvette [22]. Currently, the flow cuvette with a rectangular cross-sectional design (Figure 5.2(A)) has established itself as the standard in the commercial benchtop flow cytometry field , as it offers a more compact design in comparison to the stream-in-air nozzle design, which requires a significantly larger and complex experimental setup. The stream-in-air is a technique employed for introducing a sample into a small, vertical downward stream in the air through a nozzle (Figure 5.2(B)), without using the flowcell. Additionally, this method has the advantage of very high speed and can be equipped with electrodes, facilitating the sorting of charged particles to different exits. Although, there are some advancements in using 3D-printed technology that can reduce the cost the rest of the flow cytometry system is still complicated [111].

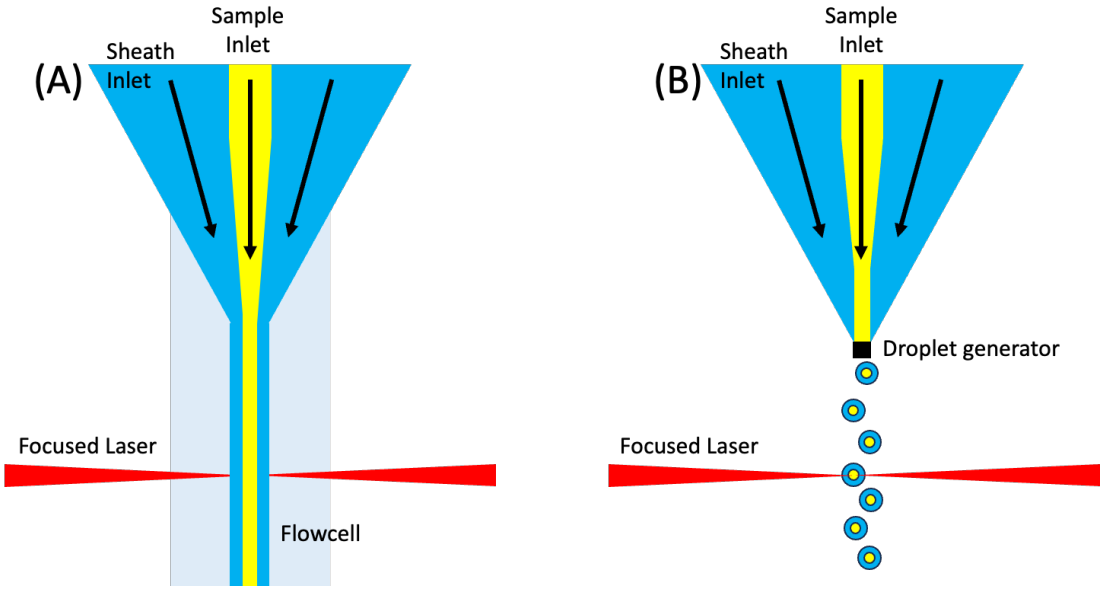

Figure 5.2 Two designs of fluidics system for FCM (A) flowcell design and (B) stream-in-air design

5.2.1 Flow cell design

In this study, the flow cell design is the cuvette-based design which exhibits a lower degree of scattering, further enhancing its utility in comparison to the stream-in-air design. Although the stream-in-air is compatible with a higher detection rate, the observation of the measuring

volume through the flat side cuvette wall is more efficient and has less distortion which can increase measurement precision. Our design includes two flow cell designs which are cuvette-based designs, based on Design I: quartz flow-through cell (Flyfiresci) and Design II: microfluidic chip (MicrofluidicChipshop). Both designs are connected to a syringe pump (NE300, Jaytee, UK) and a peristaltic pump (Multiflow, Lambda Instrument, Switzerland) to simultaneously inject sample and sheath fluid, respectively, to the flow cell establishing the focusing effect.

In this project, Design I is used to studying the introductory principles of FCM and hydrodynamic focusing. This design is based on a sheath flow electrolysis approach, which has been adapted from prior literature [112] and modified to accommodate a fluorescence lifetime cube (Horiba) and an optical breadboard with a 3D-printed support holder (Fablab). As illustrated in Figure 5.3(A), the design features a schematic representation of the flow cell. The flow cell itself is a 250 x 250 µm square quartz channel (Fireflysci) that has been modified to attach commercial fluidic connectors at both ends (Figure 5.3(B)). A 30° cone-shaped hole has been drilled at the input side to minimise the potential for turbulent flow. A cross-connector assembly (P-634, Kinesis) is connected to the inlet of the flow cell, while the remaining three nuts connect to the two-sheath inlet and sample inlet capillaries. A tee-connector assembly (P-701, Kinesis) is utilised to collect the waste at the outlet. To improve sealing, the sheath tube is tightened using stainless steel tubing (U-101, Kinesis), and the capillary is tightened using a polymer sleeve (F-237, Kinesis).

Design II is more compact and can be used with any wide-field microscope. This design is based on commercial fluidics components purchased from Microfluidic ChipShop. Figure 5.4 shows a schematic diagram of Design II based on a microfluidic chip (Fluidics 162). The chip is composed of one sample inlet in the middle channel with a cross-section dimension of 210 x 70 µm, and two sheath inlets surrounding the sample with 40° to the sample inlet. All inlets and outlets are attached with a Male Mini Luer fluid connector (10000081), which connects to the PTFE tube (10000032) through a silicone sleeve (10000032) to improve the sealing. Unused channels are blocked with Male Luer plugs (10000231). The chip is mounted on a handling frame (10000043) for mounting with a wide-field microscope. Moreover, this Design II also allows performing cell sorting in further development with the sorting microfluidic chip (Fluidics 381).

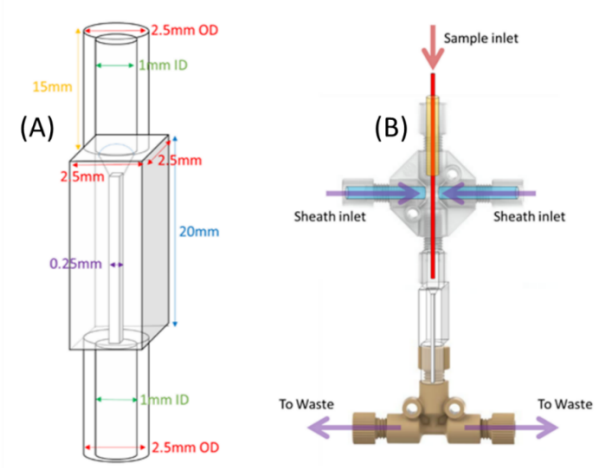

Figure 5.3 (A) schematic diagram of the flow cell Design I and (2) schematic diagram of the flow cell when connects to the commercial fluidics connectors

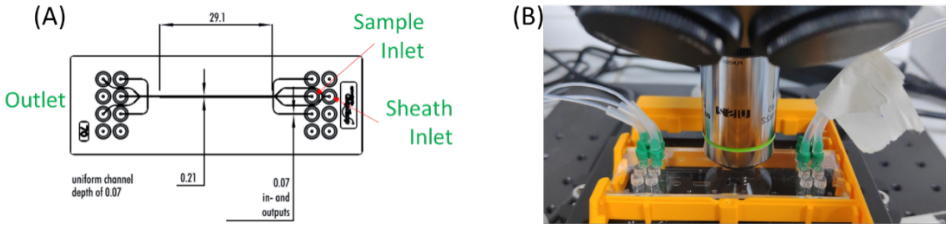

Figure 5.4 (A) schematic diagram of the flow cell Design II [113] and (B) photo of the real experimental setup

5.2.2 Reynolds number

The most important factor for hydrodynamic focusing is the flow inside the flow cell must remain laminar flow defined by an orderly smooth flow of fluid with no turbulence or mix between layers of fluid. All fluids are assumed to be Newtonian with the same density. Reynolds number is a dimensionless quantity that defines the flowing profile where laminar flow occurs in the flow cell when the Reynolds number is less than a critical value of 2300, while the transition to turbulent flow happens when the number is larger than 2300 [22], [114]. The Reynolds number is given by Equation 5.1.

$$Re = \frac{\rho v d}{\eta} \tag{5.1}$$

where ρ and η are the mass density and viscosity of the fluid, v is the flow velocity of the fluid, and d is stream diameter. However, hydraulic diameter is used due to the rectangular shape of the flow cell. This diameter is utilized in fluid calculations for non-circular tubes or flowing channels and can be treated similarly to the normal diameter of a circular tube in

fluid equations. Our developed systems are equipped with a rectangular microchannel and use distilled water and PBS as suspending media and sheath fluid. The velocity is precisely controlled by the syringe and peristaltic pumps, and the Reynolds number can be determined with a value ≈ 10 confirming the flow is laminar.

5.2.3 Focused central stream diameter calculation

The keystone of flow cytometry is to pass a single cell through the laser interrogation area, followed by fluorescence and light scattering generated from the cell. The core must be in the range of the cell's diameter, typically cells have a diameter in the range of 15-25 μm [115]. The principle of mass conservation is used to find the focused sample stream describing that the total volume of liquid flowing through the output channel equals the total volume of fluid supplied through the sample inlet and sheath input channels (Figure 5.5). Therefore, the sample diameter can be controlled by the ratio of sample to sheath flow rate. The diameter calculation has been described by Robinson in Equation 5.2 [114].

$$d_{sample} = \sqrt{\frac{f_{sample}}{f_{sheath}}} d_{flowcell} = \frac{d_{flowcell}}{\sqrt{\alpha}} \tag{5.2}$$

where d_{sample} is focused sample core width, $d_{flowcell}$ is flow cell width, f_{sample} and f_{sheath} are sample and sheath flowrate respectively, and α is flow ratio defined by $\alpha = f_{sheath}/f_{sample}$.

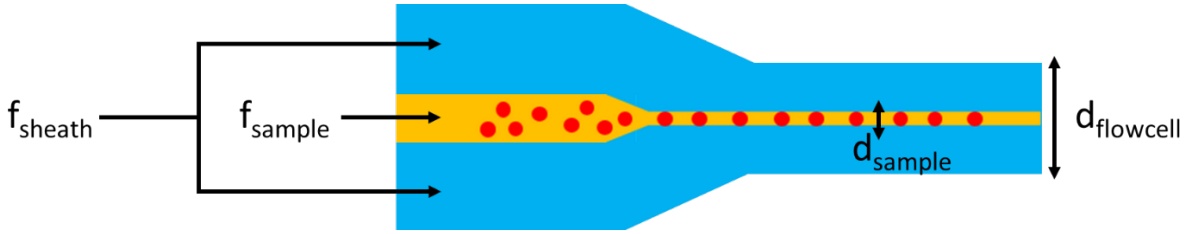

Figure 5.5 Schematic diagram of hydrodynamic focusing adapted from [114]

5.3 Investigating the relation of flow rate ratio to the focused stream width

The simultaneous injection of the sample and sheath fluid into the flow cell enables hydrodynamic focusing, resulting in a significantly reduced sample stream for single-cell analysis. The behaviour of hydrodynamic focusing can be observed through the variation of inlet flow rates, and this is accomplished using a commercial camera equipped with a CMOS sensor to generate fluorescence intensity images.

5.3.1 Sample preparation

Before experiments with valuable fluorescent beads, nanoparticles and sensitive biological samples, the hydrodynamic focusing effect inside the flow cell needs to be characterised by a

fluorescent dye and water as a central and surrounding fluid, respectively. In this work, we study the hydrodynamic focusing effect by injecting a fluorescein dye into the centre of the flow cell with distilled water as the sheath fluid. Fluorescein powder and PBS tablet were purchased from Sigma-Aldrich, respectively. Fluorescein has been previously measured in Chapter 4 and previous literature has reported its high quantum yield and suitability for fluorescence intensity imaging [103]. A stock of 10 mM fluorescein solution was prepared by suspending the powder in a PBS buffer following a protocol outlined online [116]. This high concentration was chosen as it is suitable for observation of the hydrodynamic focusing effect using a commercial DSLR camera.

5.3.2 Peristaltic pump calibration

To observe hydrodynamic focusing, the flow cell is injected with reference dye and sheath fluid at a varied flow rate. The syringe pump pushes the sample from a 1 ml syringe (Turemo). The sample flow rate is controlled by a syringe pump and depends on the syringe diameter and calibrated flow rate, as shown in the pump manual [117]. However, the peristaltic pump's calibration is necessary due to various factors that affect the flow rate, such as pump size, tubing size, pump speed, and fluid viscosity. In our design, the sheath fluid is drawn by a silicon tube (2.6mm OD, 1.6mm ID, Polymax), and the flow rate is proportional to an arbitrary number on the peristaltic pump (Figure 5.6(B)). Figure 5.6(A) is the relation of the number to the sheath flow rate calibrated by measuring the average weight of water at room temperature after pumping for a few minutes showing fitted data of the sheath flow rate (y) and pump speed (x) with function $y(x) = 2.06x + 42$ µl/min where $5 < x < 850$.

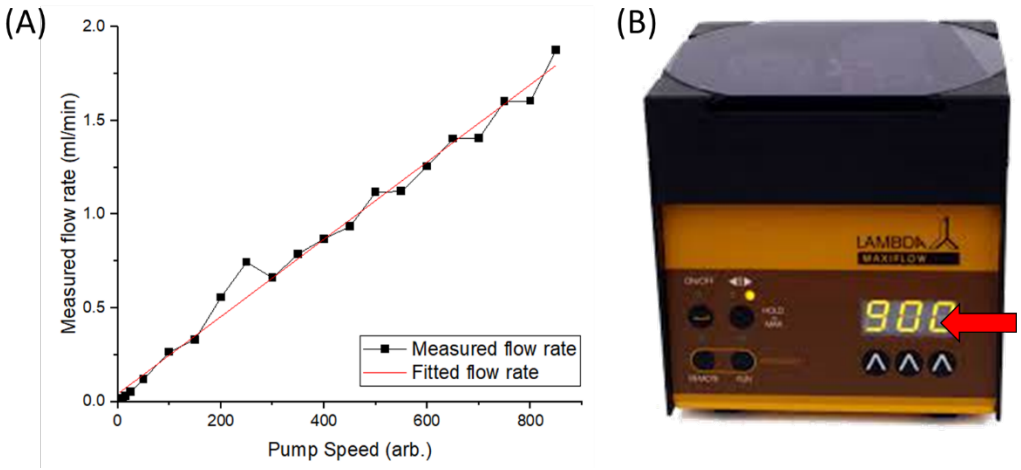

Figure 5.6 (a) Plot showing measured and linear-fitted flow rate of peristaltic pump, (b) pump speed number (arb.) indicated by the red arrow

5.3.3 Experimental setup

To observe the relation between the flow rate ratio and the focus stream width, two experiments are conducted for each flow cell design separately. Figure 5.7(A and B) shows the experimental setup for flow cell Design I and II, respectively. In the experiment for both flow cell designs, the fluorescein dye and distilled water are injected into the central and side flow channel, respectively. The measurement is performed in a completely dark room, therefore only the fluorescein stream could be imaged when it is excited by a UV lamp. Due to space, design and compactness limitations, the focused stream of Design I is imaged by Canon 60d with Canon-EF 50mm micro lens with pixel size 2.5 µm/pixel, while Design II is imaged by BX-61 Olympus microscope equipped with Nikon D3100 through 4x objective lens (N.A. = 0.16) with pixel size 5 µm/pixel. The fluorescence intensity images are taken in manual mode with a 30-second exposure time to reduce noise. The images are analysed by ImageJ software and the width is determined at FWHM of the intensity images.

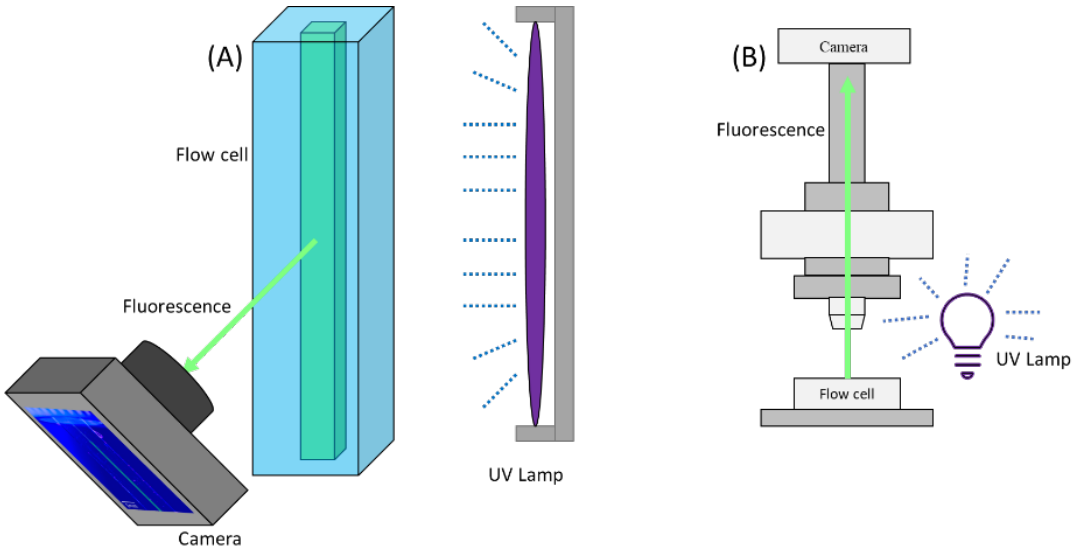

Figure 5.7 Experimental setup of finding focused fluorescein stream for (A) Design I and (B) Design II

5.3.4 Focused stream width determination

According to Equation 5.2, the width of the focused stream depends on the flow cell's geometry and the sample-sheath ratio (α) with decreasing values resulting in a narrower central flow diameter. Therefore, the fluorescence intensity images are taken from various α ratios of Design I and II.

For Design I, the measurement is performed under a fixed sample flow rate of 20 µl/min, and for Design II constant flow rate of 10 µl/min. The sheath flow rate is varied between 0.09 -

0.87 ml/min for Design I and 0.05 - 0.09 ml/min for Design II to adjust the desired α ratio. As shown in Table 4 and Table 5, fluorescence intensity images show the hydrodynamic focusing effect within α = 4 - 43 for Design I and α = 4 - 10 for Design II. To determine the hydrodynamic focusing phenomena, the width of the focused stream is measured at a distance of 1 mm from the intersection of the inlets. The velocity inside the flow cell is calculated by the total volumetric flow rate giving a velocity between 5.34 – 237.28 µm/ms for Design I and 11.34 – 117.53 µm/ms for Design II, while the excess flow rate can cause leakage. Under the given flow rate parameters above, the focused sample stream diameter is extracted into an intensity profile plot along the x-axis, where the diameter is calculated from the FWHM as demonstrated in Figure 5.8 and Figure 5.9, using ImageJ software.

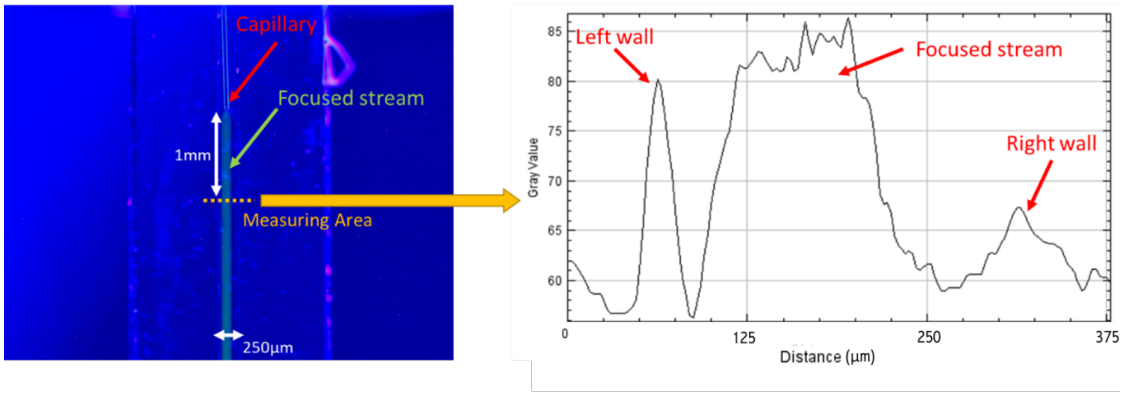

Figure 5.8 Photograph of the focused fluorescein (left) inside the flow cell Design I and the corresponding intensity profile measured from a horizontal line (dash orange line) across the flow cell (right)

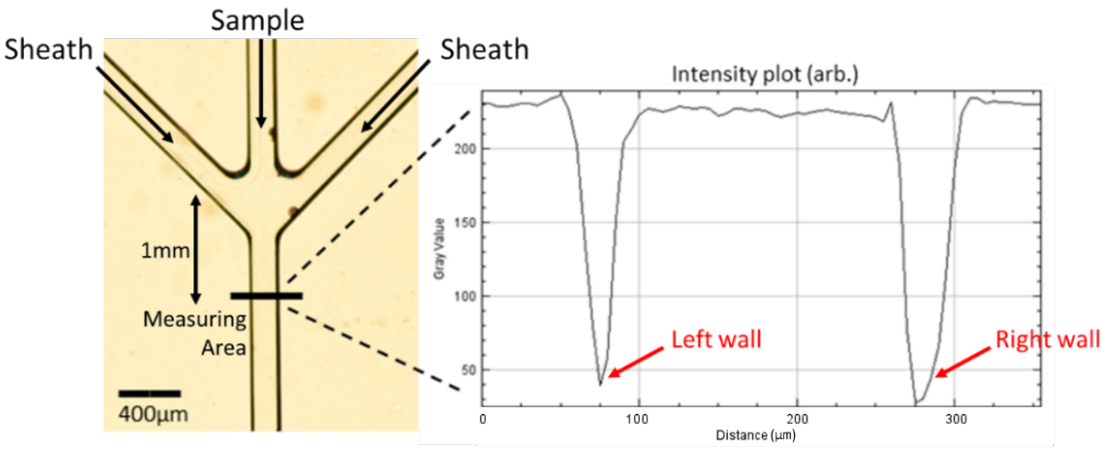

Figure 5.9 Photograph of the bright field image (left) of the flow cell Design II and the corresponding intensity profile measured from a horizontal line (black line) across the flow cell (right)

Table 4 The photograph of the focused fluorescein stream inside the flow cell Design I with the corresponding flow rate ratio (α), intensity profile and fluorescein stream width calculated from its FWHM.

Flow ratio	Image	Intensity profile plot (arb.)
4.673	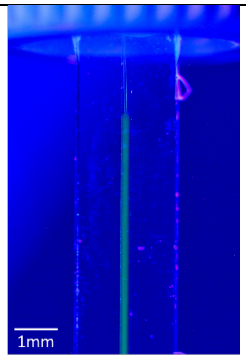	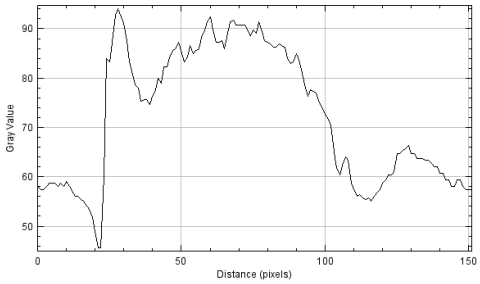 Core diameter = 139 ± 17 µm
7.246	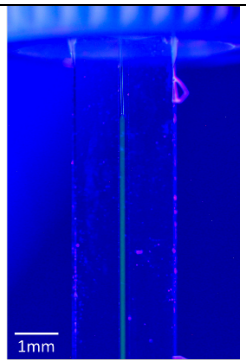	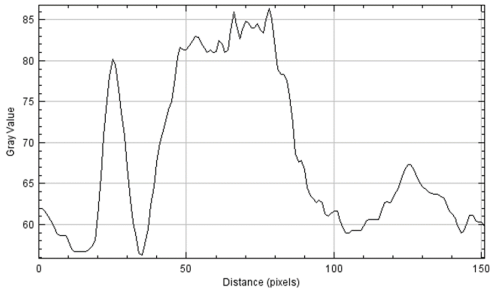 Core diameter = 108 ± 7 µm
12.346	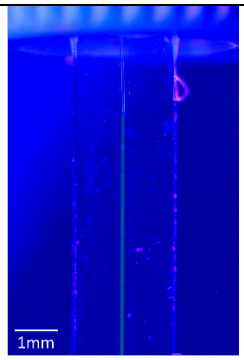	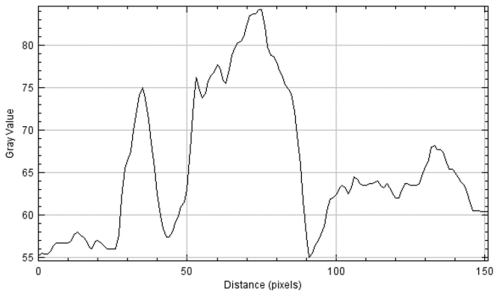 Core diameter = 88 ± 4 µm
22.727	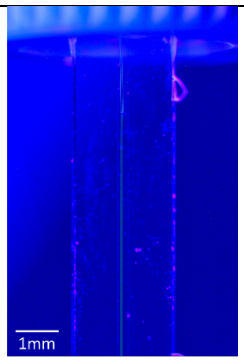	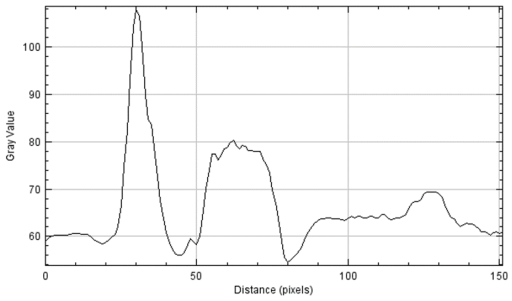 Core diameter = 54 ± 4 µm

33.333	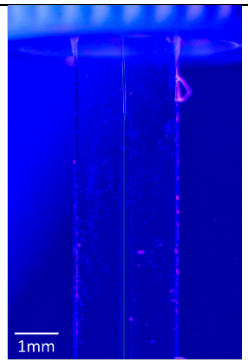	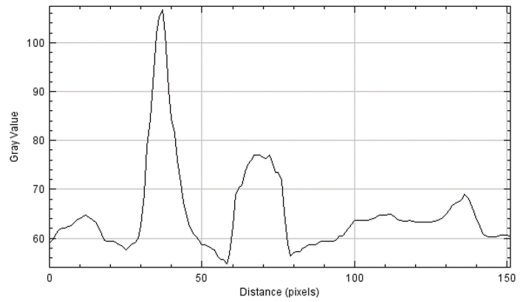 Core diameter = 44 ± 1 µm
43.478	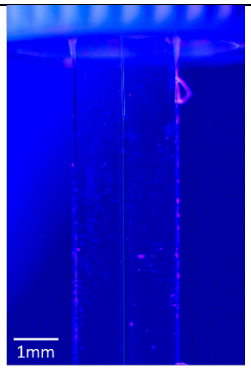	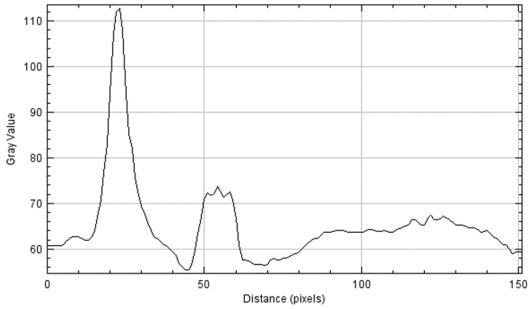 Core diameter = 34 ± 4 µm

Table 5 The photograph of the focused fluorescein stream inside the flow cell Design II with the corresponding flow rate ratio (α), intensity profile and fluorescein stream width calculated from its FWHM.

Flow ratio	Image	Intensity profile plot (arb.)
5.236	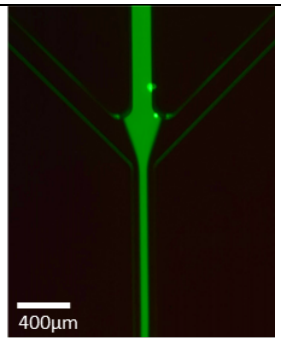	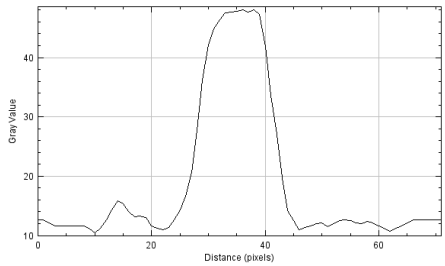 Core diameter = 69 ± 5 µm
6.250	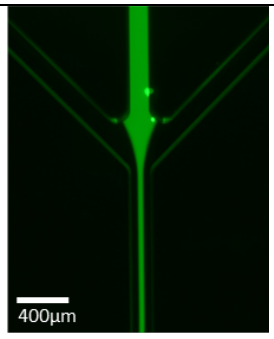	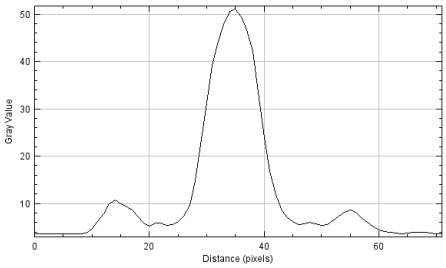 Core diameter = 55 ± 1 µm

8.333	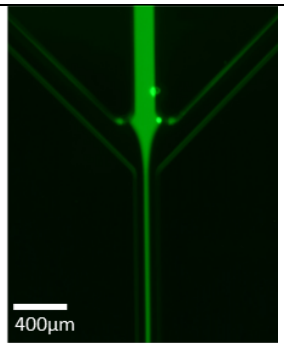	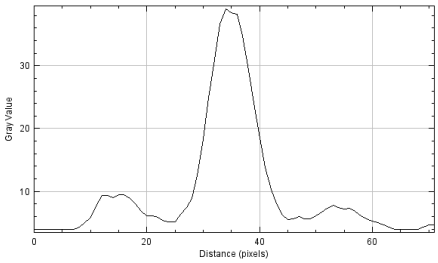 Core diameter = 47 ± 2 µm
9.346	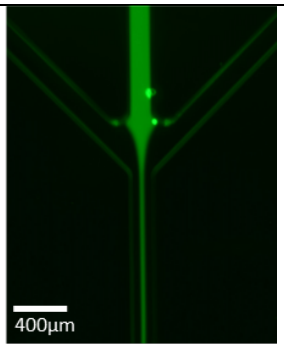	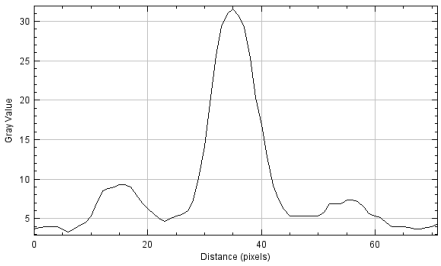 Core diameter = 51 ± 3 µm

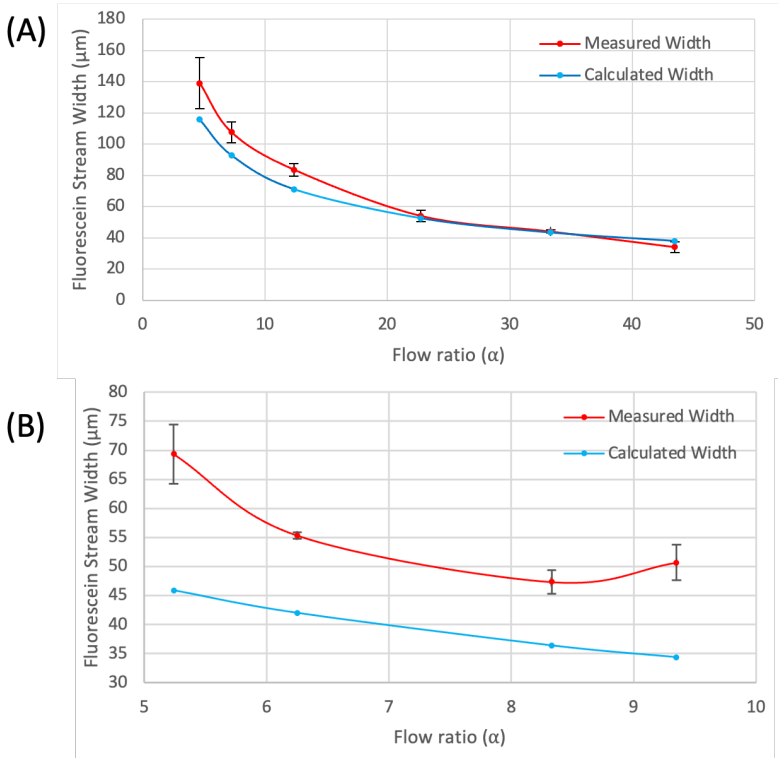

Figure 5.10 The measured sheath fluid compared to the flow ratio (α) of (A) Design I and (B) Design II.

As illustrated in Figure 5.10, both flow cell designs demonstrate a correlation between the focused stream width and the α ratio. The focused stream diameter decreases as the flow ratio increases, with a minimum sample stream diameter of 34 ± 4 µm and 47 ± 2 µm for Design I and II, respectively. When the ratio exceeds 33.33 for Design I, a slight improvement in narrowing is observed. Beyond this value, there is a negligible impact on the focused stream width. However, a value of α greater than 10 for Design II may result in liquid leakage. The measured fluorescein stream width from Design I is consistent with the calculated value from Equation 5.2, however, the measured width from Design II is greater than the calculated value. This discrepancy can be attributed to the pulsating nature of the peristaltic pump, which uses a squeezing and un-squeezing process to drive the sheath fluid into the flow cell, resulting in fluctuations in the sheath flow rate. The fluorescein width fluctuates roughly between 47.8 – 106.4 µm with α = 6.25, which is captured by a 30-frame-per-second (fps) video recorded by the camera in video mode (Figure 5.11). Although the 30-second exposure period can significantly reduce the noise in the photo, it may also contribute to the blurring of the fluorescein stream due to the pulsation, leading to an unclear edge and affecting the width determination of the fluorescein stream. This phenomenon is not present in Design I due to its larger cross-section area, which can stabilise the overall flow rate against fluctuations in the input flow rate.

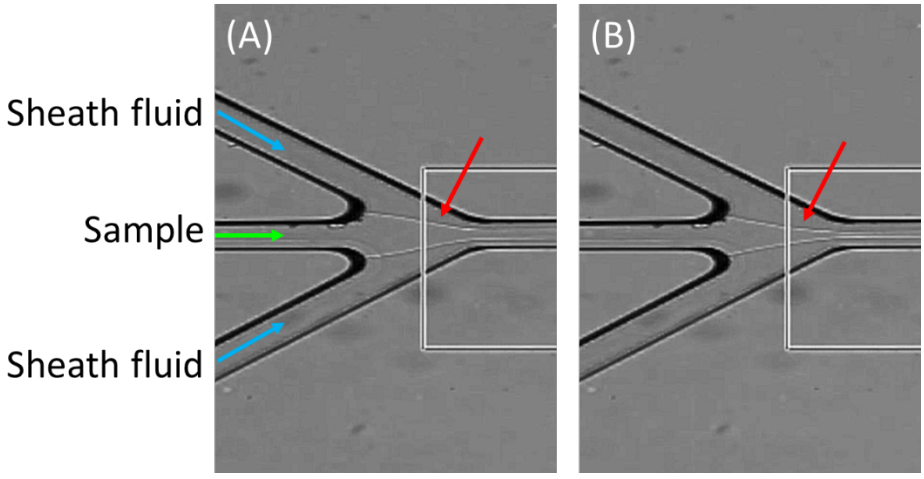

Figure 5.11 Pulsating behaviour of the peristaltic pump that affects the focused stream width with α = 6.25 when (A) before and (B) after the pressure pulse from the pump

The difference of minimum α, smallest sample diameter or speed between Design I and II depends on the flow cell's geometry and fluidics viscosity. In comparison, Design I offers fluorescence detection at 90° to the excitation line, better hydrodynamic focusing and sealing that enables less excitation signal, speedy measurement and stability when connects with

high flow rate pumps, however, one obvious drawback arises when the α value is excessively low or high, it may result in flow instability due to sample or sheath flow entering unintended inlets causing flow stability issue [118]. This can also alter the focused stream position in the sample injecting capillary in Design I, potentially affecting the measurement accuracy. In contrast, Design II demonstrates a smaller sample width at the same α ratio compared to Design I, leading to a slower overall flow rate and reducing the possibility of miscounted particles. Design II is based on a compact, compatible microscope microfluidic chip with a smaller cross-section area that only supports slow flow rates. It features a fixed sample injector that provides stable focused flow compared to Design I. Furthermore, the 2D rectangle array of SPADs in Design II allows for the creation of images of flowing samples and holds potential for future fluorescence lifetime imaging in flow cytometry.

In conclusion, the analysis of flow cytometry design reveals that Design II is superior to Design I in several key aspects. Design II has a smaller sample width with the same α value, which leads to a slower overall flow rate compared to Design I, resulting in increased particle detection rates and improved stability of the focused flow. On the other hand, Design I presents a number of drawbacks, including the potential for flow instability and effects on measurement accuracy, especially when the α value is excessively low or high. Therefore, future studies will use Design II to optimise the results of flow cytometry experiments.

5.4 Fluorescence intensity and lifetime determination in a focused stream

Our findings demonstrate the possibility of observing the hydrodynamic focusing effect using a commercial DSLR camera. However, this camera is not suitable for FCM applications due to its low speed and commercial firmware that restricts the use of custom software for analysing fluorescence intensity and lifetime data. In light of these limitations, the commercial DSLR camera was replaced with a SPAD camera and MATLAB-based software was developed for communication, measurement and data analysis purposes. Therefore, an extra hydrodynamic focusing observation is required to ensure that the SPAD measuring area fully covers the focused sample stream.

5.4.1 Sample preparation

The sample of this study is hpDNA labelled with Cy5 taken from the final product of nanoprobe synthesis. The hpDNA is injected into the flow cell without sheath and with sheath fluid (α = 8.33). Suitable excitation and emission wavelength are selected from spectroscopic data from Fluorolog-3 (Figure 5.12).

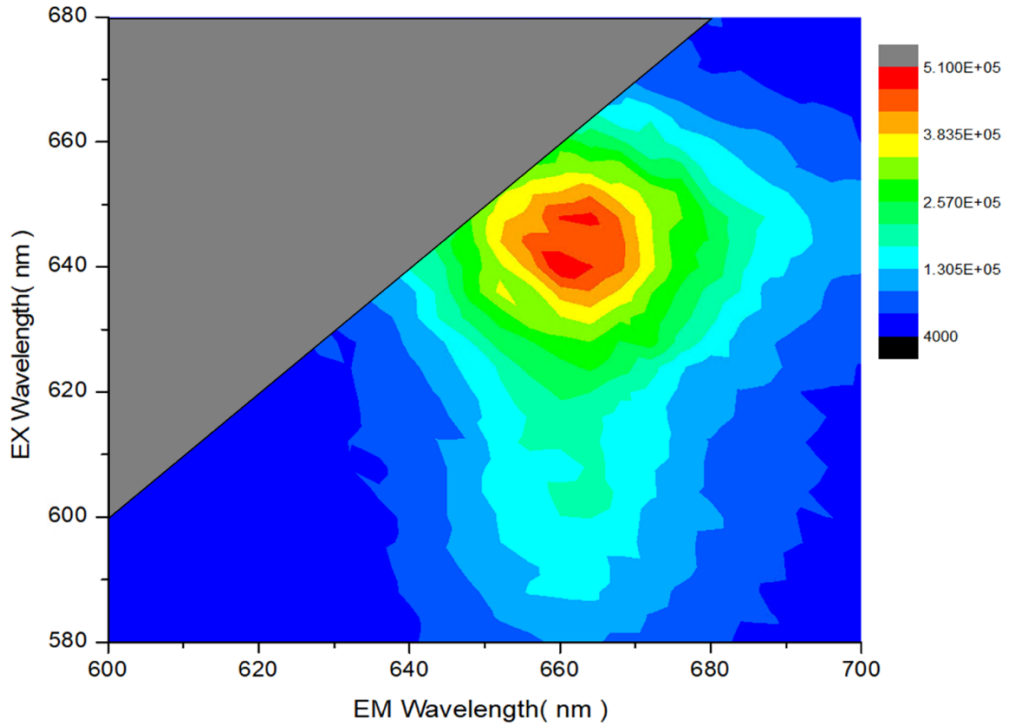

Figure 5.12 A map displaying color-coded fluorescence emission intensity in relation to the fluorescence emission (x-axis) and excitation wavelengths (y-axis) of hpDNA-Cy5, measured using Fluorolog-3.

The reference fluorescence lifetime of hpDNA-Cy5 was obtained using the DeltaFlex system with Data Station software. A 4 mL cuvette was filled with 1 mL of the hpDNA-Cy5 and 2 mL of distilled water. The sample was excited by a 640 nm laser operating at 1 MHz, and the fluorescence signal was collected through a monochromator with a 32 nm window width centred at 670 nm. The fluorescence was recorded until it reached a peak of 10,000 counts. The lifetime analysis was performed using the DAS6 software (Figure 5.13), which applied a least square fitting method with a 3-exponential model. The three-lifetime components were found to be $\tau_1 = 0.04 \pm 0.00$ ns, $\tau_2 = 1.06 \pm 0.02$ ns, and $\tau_3 = 1.48 \pm 0.01$ ns, with relative contributions of 2.84%, 32.25%, and 64.91%, respectively. These components resulted in an average lifetime of 1.30 ± 0.01 ns, which is longer than the reported free Cy5 lifetime in water (0.90 – 1.00 ns) [90], [103] due to the sample being a remnant from nanoprobe synthesis, which is affected by the solution's environmental parameters and conjugation with the DNA that show increased Cy5 lifetime up to 2.38 ns [119].

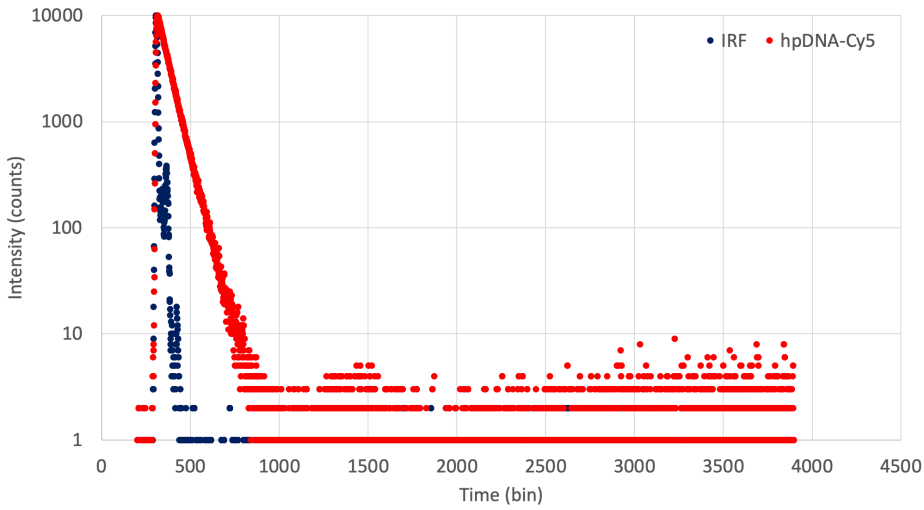

Figure 5.13 Fluorescence decay where blue and dots are IRF and fluorescence decay of hpDNA-Cy5, respectively. The system contains 4096 bins with 26 ps bin width.

5.4.2 Experimental setup

The experimental setup is shown in Figure 5.14. The detector is replaced with the SPAD camera to image the flow cell placed under the objective lens. A dichroic mirror reflects a 640 nm pulsed laser (Horiba), operating at 10 MHz, to the sample and allows the fluorescence signal to travel to the SPAD camera through a 665 nm long pass emission filter. With a 20x objective lens (N.A. = 0.4), the FOV is a rectangle shape of a 192 x 128-pixel array covering an area of 85.96 x 57.31 μm^2. The sample is injected at 10 µl/min, while the sheath fluid is driven at $\alpha = 8.33$ flow ratio.

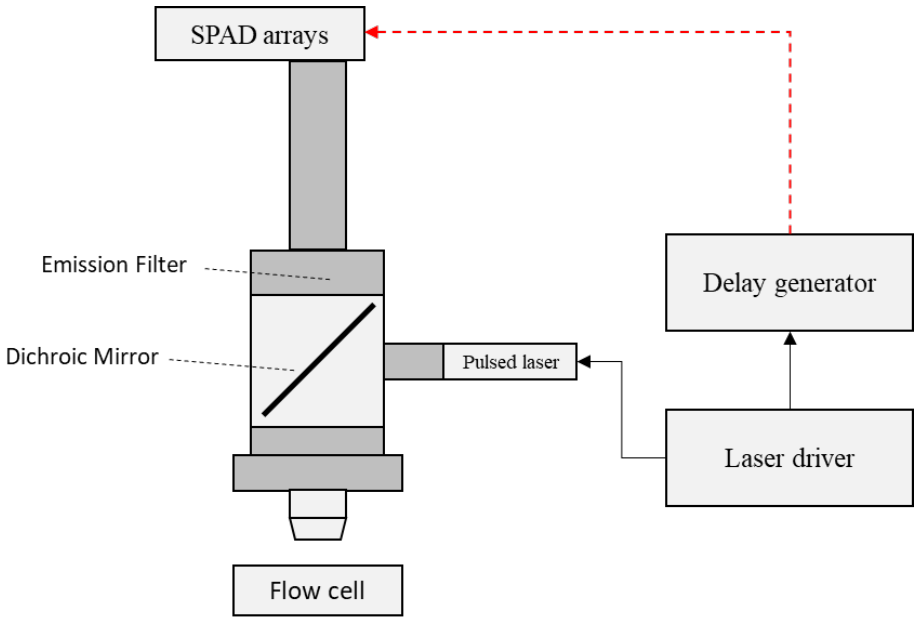

Figure 5.14 Experimental setup for observing focused fluorescein stream.

5.4.3 Fluorescence intensity and lifetime measurement

The fluorescence intensity images shown in Figure 5.15 are colour-coded representations of fluorescence intensity measurements taken using a SPAD camera. Each measurement was taken with an exposure time of 3 ms. In the absence of sheath fluid, the sample completely fills both flow cells, as seen in Figure 5.15(E). The introduction of the sheath fluid results in a reduction of intensity over time, as shown in the plot from Figure 5.15(D-A), which also indicates a decrease in stream diameter. The sheath fluid begins to be driven at t = 10 seconds with an α of 8.33 and the sample diameter becomes fully focused at t = 70 seconds.

A non-uniform illumination issue is observed in the wide-field microscope setup, with the top right measurement area appearing brighter than the bottom left area. This is clearly indicated in the colour-coded image of Figure 5.15(E), where red represents pixels with an intensity greater than 400 counts and blue represents pixels with an intensity less than 100 counts. This issue makes it difficult to estimate the focused stream diameter of the hpDNA-Cy5.

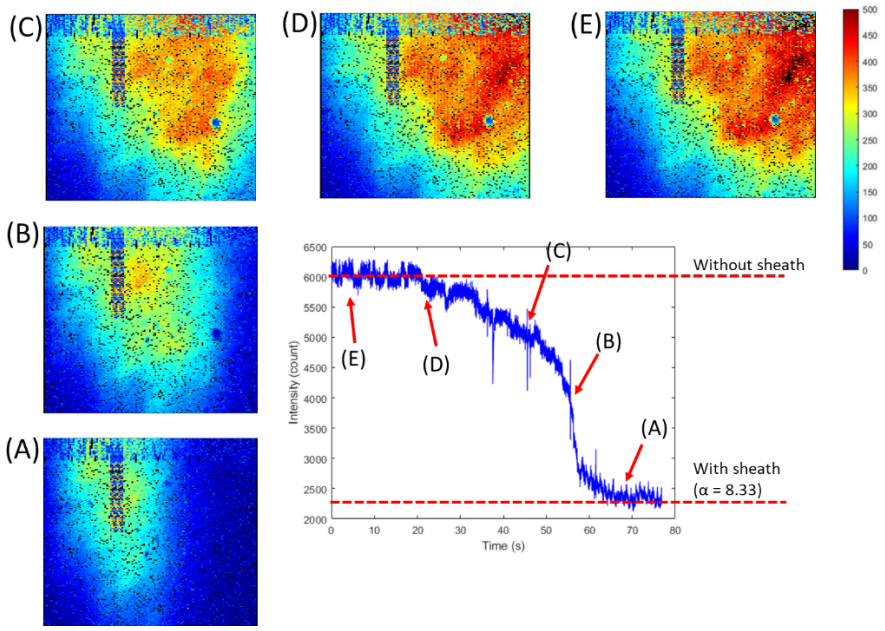

Figure 5.15 Fluorescence intensity plot over the time and corresponding colour-coded intensity image (A-E), where (A) when the sample fully focused at t = 70 sec, (B) t = 55 sec, (C) t = 40 sec, (D) t = 20 sec and (E) before introducing the sheath fluid. The sheath is driven at t = 10 sec.

Fluorescence lifetime images can provide focused stream information with better contrast. Unlike the fluorescence intensity image, the lifetime image is independent of the variation of fluorophore concentration and excitation intensity. The boundary of the sample contacting

the sheath fluid tends to have less brightness due to concentration change due to the dilution effect.

In TCSPC data from the SPAD array, each pixel is capable of detecting a single photon per frame. A total of 1,000 continuous frames were captured to gather enough photons for lifetime calculation. The lifetime of each pixel was determined using the CMM method and a 200-bin measurement window, with a lower intensity threshold of 80 photons. Pixels with less than 80 photons are assigned a lifetime of zero, appearing as black in the resulting FLIM images. Figure 5.16 presents FLIM images of flowing hpDNA-Cy5 with and without sheath fluid. The results show that the lifetime is consistent and uniform around 1 ns in the absence of the sheath fluid, but more background pixels become apparent when the sheath fluid narrows the hpDNA-Cy5 stream, revealing the flow of non-fluorescent surrounding water. The width of the sample stream was measured from coordinates y = 20 to 100, excluding bad pixels and pixels that did not pass the intensity threshold, as indicated by the red arrow in Figure 5.16. The stream width was determined to be 80 pixels, equivalent to 36 µm. This measurement of the focused stream width from the lifetime image is narrower compared to that observed from a commercial camera. This is possibly due to the dilution effect at the sample boundary, which reduces the intensity and causes pixels to fall below the intensity threshold.

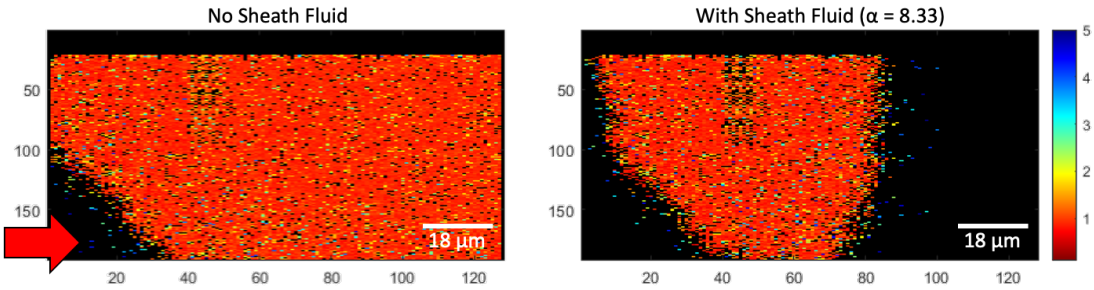

Figure 5.16 Colour-coded fluorescence lifetime image of flowing hpDNA-Cy5, with (left) and without (right) sheath fluid, captured from SPAD camera with 3 ms exposure time for 1,000 frames. The lifetime is calculated from the CMM method with 80 counts lower intensity threshold. The red arrow indicates pixels that did not pass the intensity threshold due to the non-uniform illuminating area

5.5 Enhancing particle detection rate by a focused stream

One reason for implementing hydrodynamic focusing in FCM is to improve detection efficiency by driving as many single particles as possible through the detection volume. The particles are usually suspended in a non-fluorescent media such as PBS or distilled water and

injected into the flow cell. The fluorescence signal can be only detected when the particle appears in the measuring volume, which is much smaller than the flow cell. Without sheath flow, the particles can appear outside the measuring volume. This can reduce the number of detected events.

5.5.1 Sample preparation

Crimson fluorescent latex microspheres (C-bead, FluoSpheres™, ThermoFisher) have been purchased from Thermofisher (F8831, UK). The stock solution with a density of $3.6x10^6$ beads/ml is diluted 10 times to get $3.6x10^5$ beads/ml in suspending media. The media is prepared from 20% glycerol with 15 µl of 0.2% SDS to slow down or prevent the sedimentation process of the bead. The suitable excitation and emission wavelength are determined by Fluolog-3. Figure 5.17 shows the excitation and emission profile from the 3D mode measurement showing the peak excitation is 640 nm, while emission is 660 nm.

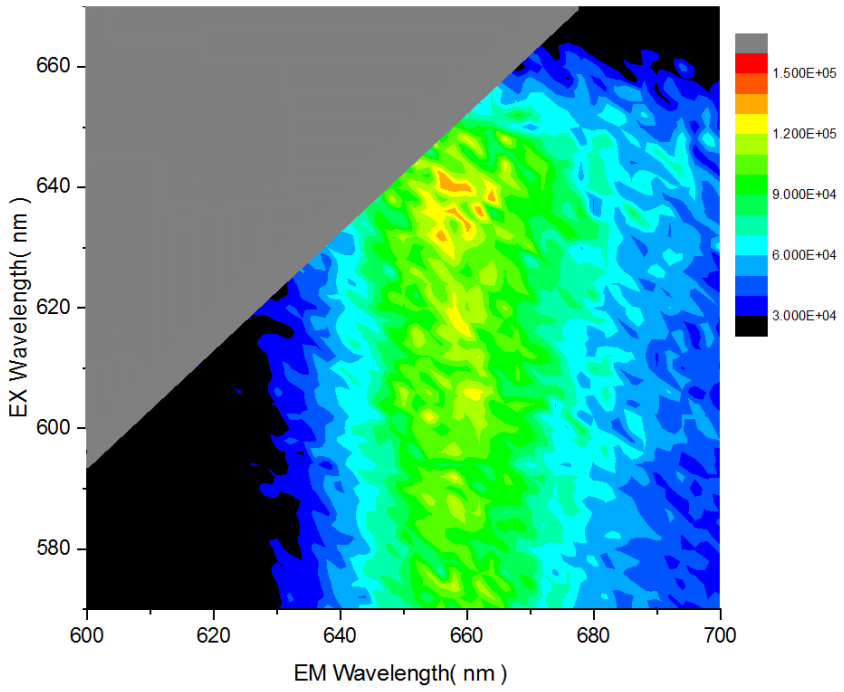

Figure 5.17 A map displaying color-coded fluorescence emission intensity in relation to the fluorescence emission (x-axis) and excitation wavelengths (y-axis) of C-bead, measured using Fluorolog-3.

5.5.2 Experimental setup

As shown in Figure 5.18, the suspended C-bead particles, with a density of $3.6x10^5$ beads/ml, are injected into the central channel of flow cell Design II with a flow rate of 10 µl/min. Distilled water is used as sheath fluid with varied rates to achieve the α ratio of 6.25. The

flow cell is placed under a 20x objective lens (N.A. = 0.4) of a wide field microscope equipped with the ultra-fast SPAD camera in order to detect the fluorescence intensity of the flowing particle individually to acquire the data within a 3 ms exposure time. 5,000 continuous frames (16.15 seconds total time, including data transfer to the PC) have been recorded. This measurement is performed with and without sheath fluid for focusing the central stream to minimise the miscount particle possibility.

To demonstrate that the particle stream is narrowed down in the measuring area, photon stream measurement has been performed to observe the enhancement of the particle detection efficiency. In this measurement, the SPAD camera continuously measures fluorescence intensity from the measurement area and the recorded data is plotted over time. However, suspended particles are different from dye solution in that not every captured frame contains a fluorescence signal. Therefore, the intensity peak in photon stream data is indicating a single particle that passes through the measurement area, while low-intensity frames indicate frames with only sheath fluid and the bead suspension fluid with no beads.

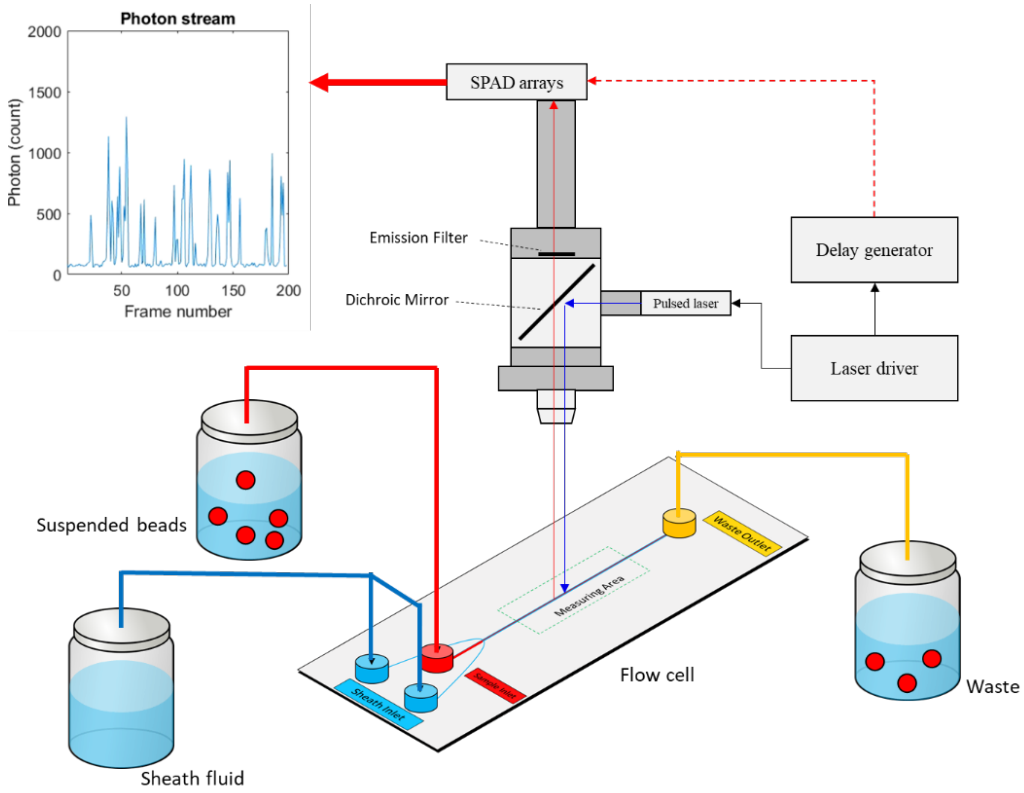

Figure 5.18 Experimental setup for observing C-bead particle in a focused stream.

5.5.3 Effect of hydrodynamic focusing on the number of detected particles

Figure 5.19 illustrates the photon stream plot obtained from 5,000 consecutive measurements conducted over a period of 16.15 seconds. A minimum intensity threshold of 400 counts is employed to identify bead events within the measurements. The number of detected bead events is 568 and 724 in the cases with ($\alpha = 6.25$) and without the sheath flow, respectively. This demonstrates that the introduction of the sheath flow results in a focused particle stream, increasing the number of detected events by 27.46% compared to the case without sheath flow.

The fewer detected events in the absence of sheath flow can be described as a miscounted bead scenario, where beads go undetected because they either appear outside the measurement area or partially within it. Furthermore, some peaks in the plot exhibit a significant decrease in intensity due to a lack of focusing effect. This effect not only compresses the particles into the centre of the flow cell along the x-y plane but also stabilizes their movement in the focal plane (z-axis).

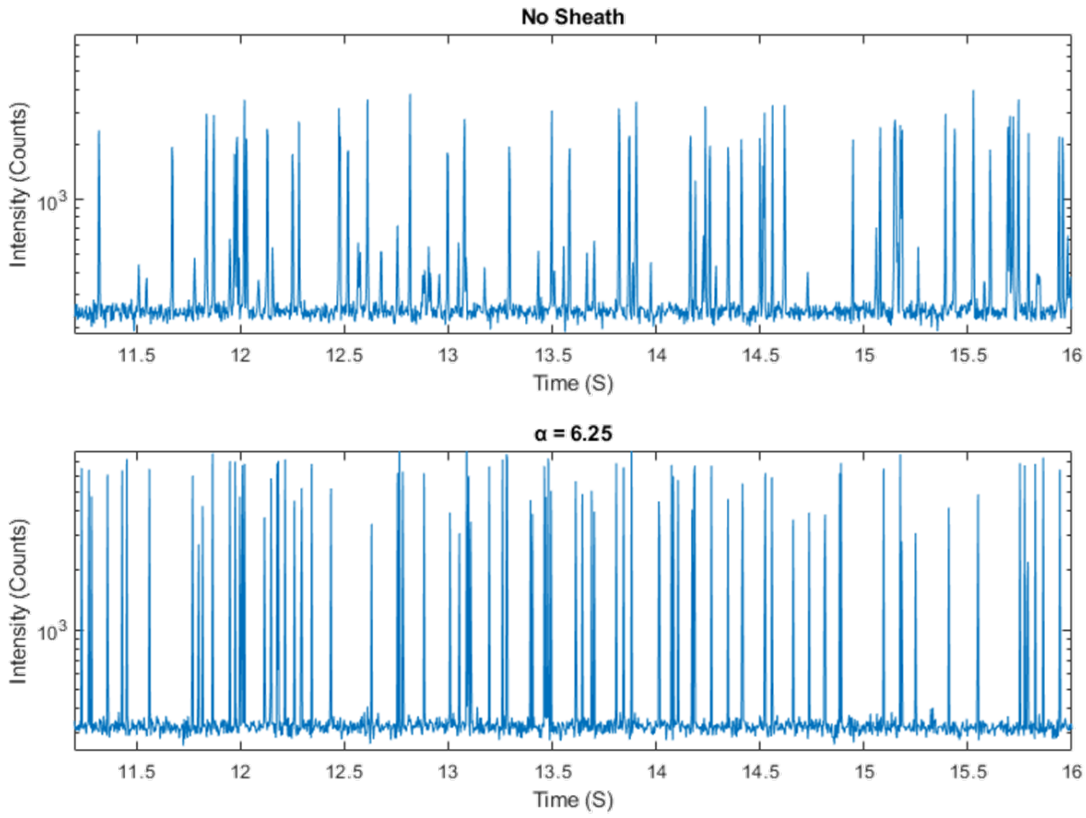

Figure 5.19 Fluorescence intensity (with and without sheath fluid) plot against the measurement time taken from t = 11 sec to t = 16 sec.

5.5.4 Effect of exposure time on the number of detected particles

Our experiment has revealed the advantages and limitations of using sheath flow in particle detection. By using sheath flow, the number of particle detections within a given measurement period can be significantly increased. However, the exposure time is a critical factor that influences the detection results. A shorter exposure time allows for a higher chance of capturing individual particles, but it also increases the dead time between frames, which can result in a reduction of the overall number of detections. The dead time will be later discussed in Chapter 6. On the other hand, longer exposure times decrease the dead time between frames by reducing the amount of data transfer to the PC but also increase the likelihood of detecting multiple particles, leading to a lower number of particle detections. To further explore these findings, this experiment is repeated with the same C-bead density of 3.6×10^5 beads/ml and a range of exposure times. The C-bead is injected with a 10 µl/min flow rate, while the sheath flow is established to get $\alpha = 6.25$. This allowed us to observe the impact of different exposure times on the number of detections and the trade-off between dead time and detection accuracy.

The SPAD camera was configured to the TCSPC mode in order to measure the number of detected events in particle detection experiments utilising sheath flow. The exposure time is set to 100 µs, 500 µs, 1500 µs, 3000 µs, and 5000 µs with the corresponding number of measured frames of 1216, 1216, 832, 494, and 302, respectively, to maintain similar total measurement time around 1.6 seconds. In order to accurately count the number of events, the lower intensity threshold is adjusted separately for each exposure time setting. The minimum photon counts were set to 30, 80, 230, 300, and 400 counts, respectively. This intensity threshold is determined by the background value for each measurement to distinguish between the background and the peaks. By analysing the results (Figure 5.20), it was found that the exposure times of 100 µs and 5000 µs resulted in the lowest detected events, with 21 and 32 events, respectively. On the other hand, the exposure times of 500 µs, 1500 µs, and 3000 µs resulted in the optimal event numbers, with 56, 65, and 62 detected events, respectively. These findings indicate that the choice of exposure time can have a significant impact on the results obtained in particle detection experiments using sheath flow. Therefore, it is important to carefully consider the exposure time when performing such experiments to ensure accurate results.

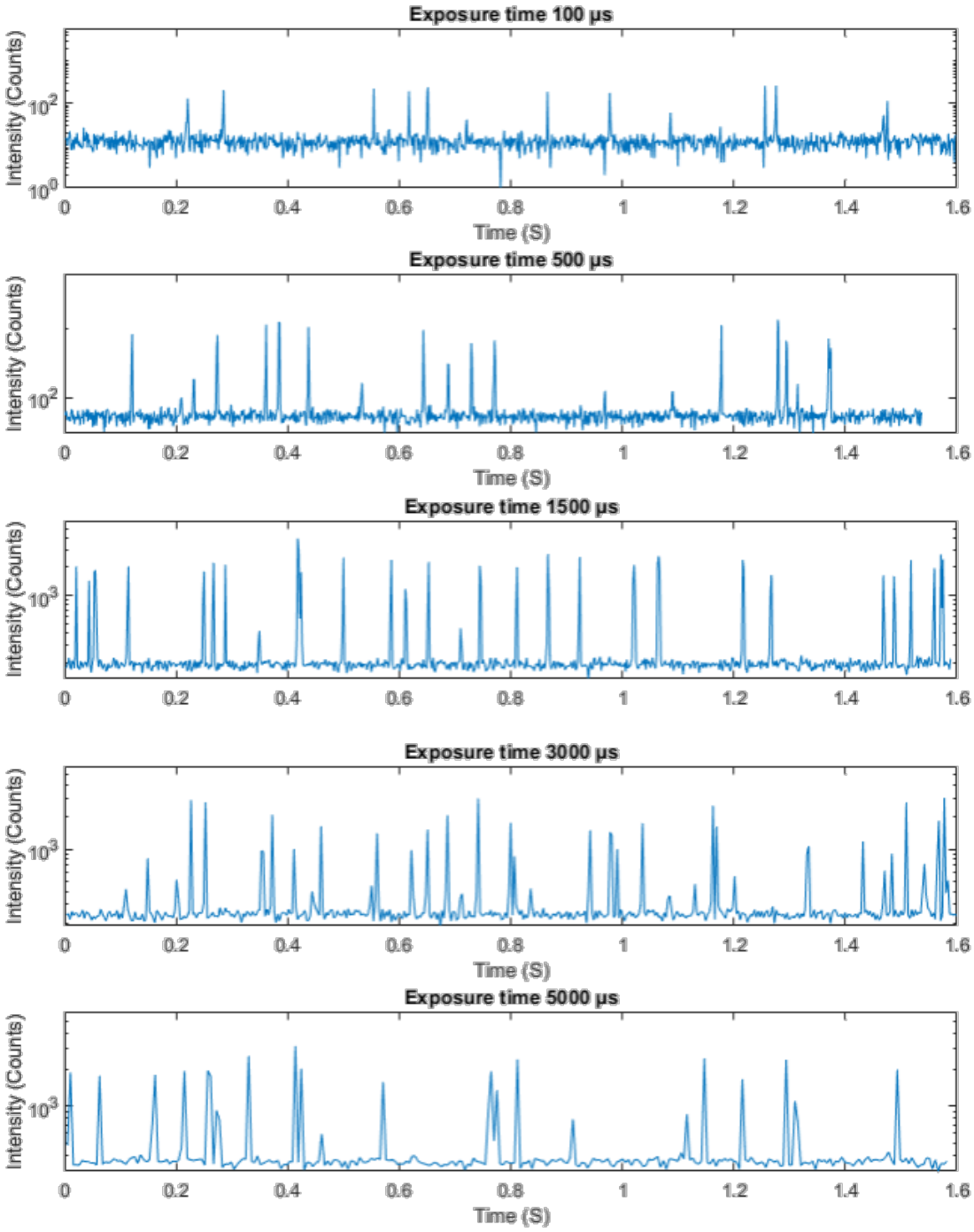

Figure 5.20 Fluorescence intensity against time plot when varied the exposure time of 100 µs, 500 µs, 1500 µs, 3000 µs and 5000 µs with the corresponding number of measured frames of 1216, 1216, 832, 494, and 302, respectively, to maintain similar total measurement time around 1.6 seconds.

5.6 Conclusion

Overall, two design of flow cell that enable hydrodynamic focusing phenomena has been described. The narrowed sample stream width is established by controlling the α ratio calculated from the sheath/sample flow rate. Our current setup can vary the focused sample stream width between 139 – 34 μm for Design I and 69 – 47 μm for Design II. The hydrodynamic effect in the flow cell is observed by various measurements including fluorescence intensity, FLIM, and photon stream. The system also shows the capability of fluorescence lifetime measurement by using the CMM method which is required for further study in lifetime-based FCM.

In a later study of this thesis, the author has chosen flow cell Design II. Although Design I shows smaller sample stream width, it requires high overall speed, however, it is too fast for the current SPAD detector and this can make the flow unstable. With the same α, Design II shows better performance that can narrow the central stream more than Design I. In addition, Design II operates at a slower speed which allows data transferring to the PC and real-time analysis. The drawback of Design II is not suitable for a high flow rate. Leakage is found when the total flow rate is more than 100 μl/min. Improved sealing can be considered for future studies for higher speed detection.

Chapter 6 Fluorescence lifetime detection of Flowing Particles and Cells

6.1 Introduction

Nowadays, cancer diagnosis methods have been developed using various techniques as cancer is a chronic illness which has more mortality at later stages. The current diagnosis involves a combination of methods to confirm the test result such as biopsies, imaging tests, molecular diagnostics, endoscopy, and liquid biopsies [120]. Biopsies provide a definitive diagnosis but can be invasive because a small amount of tissue from the area where cancer may be present is taken out. This diagnosis is based on cell morphology and protein expression from a part of tissue removed from the sample [121]. Imaging tests including X-rays, computed tomography (CT) scans and magnetic resonance imaging (MRI) also offer detailed information about tumours but may require further investigation for conclusive results. Moreover, this mass analysis may result in information loss by failing to uncover rare genetic cancer subgroups that may influence therapy decision paths. Molecular diagnostics such as polymerase chain reaction (PCR) analyse genetic alterations but can be limited by availability and cost. Endoscopy allows for direct visualisation but carries risks of bleeding, adverse reaction, infection and overdiagnosis [122]. Liquid biopsies are non-invasive but their sensitivity and specificity depend on the tumour type [120] and can produce false positives or negatives [123]. Therefore, a comprehensive approach considering multiple factors and diagnostic methods is crucial to accurately diagnose cancer and this should help the routine cancer study.

Among these methods, the novel nanoprobe based on GNR for detecting cancer biomarkers has shown its promising performance in target RNA detection [17]. It has been developed with an excellent performance in distinguishing between cancer and healthy cell by using fluorescence intensity and lifetime. The Cy5 in nanoprobe incubated with PC3 has shown a longer fluorescence lifetime than that incubated with the HEK293 cell line [29]. Moreover, the use of lifetime as the indicator brings the advantages of the lifetime to cancer detection, especially concentration independence and distinguishable from scattering and background signal, which can improve reliability and accuracy. However, the current detection method for this nanoprobe incubated with cell lines is based on FLIM, which can cause user bias by selecting a few areas from the microscope slide rather than measuring every single cell, and

this also increases the chances of missing a rare cancer cell among healthy cells. Moreover, the slide preparation process involves multiple steps and is time-consuming.

To address the limitations associated with the current detection methodology, the usage of the FCM with fluorescence lifetime detection capabilities has been investigated. FCM is a technique used to analyse and quantify various characteristics of individual cells or particles within a heterogeneous mixture. FCM involves suspending cells in a fluid medium and passing them through a flowcell, where the cells are illuminated by lasers as they flow in a focused stream one by one. Detectors capture the fluorescence emitted by the cells, generating data that can be analysed to determine cell populations and specific markers of interest. This approach offers the ability to rapidly detect every single cell within large cell populations, based on fluorescence detection. In contrast to FLIM, fluorescence lifetime-based FCM enables the analysis of sub-populations and rare events, with the ability to simultaneously detect and analyse multiple parameters. Additionally, FCM offers the potential for cell sorting and purification, further helping in clinical applications. These advantages make fluorescence lifetime-based FCM a compelling alternative to the current methodology, with the potential to overcome the limitations of observer bias and time-consuming slide preparation.

In this chapter, we assemble the SPAD camera, hydrodynamic focusing system, and the developed MATLAB code, which have been discussed in Chapters 4, 5 and 3 respectively, together to create the FCM system for measuring the fluorescence lifetime of flowing cells or particles. We show the prototype of a time-domain fluorescence lifetime flow cytometry platform on a compact wide-field microscope setup. A 192x128 TCSPC SPAD array [47] is calibrated and configured to a megapixel with 24,576 data channels to increase photon bandwidth. Our analysis software has a GUI that includes CMM lifetime analysis and phasor plot, which enable real-time lifetime estimation and promising capability to differentiate lifetime population. The developed system is subjected to intense evaluation using fluorescent beads with weak and strong intensity to mimic negative and positive samples, respectively, for RNA nanoprobes. This testing aimed to assess the system's sensitivity, specificity, and accuracy in detecting and quantifying the target RNA. Following the successful completion of the validation phase, the system will be applied to investigate the incubated PC3 and Hek293 cell lines with the nanoprobe. This subsequent analysis will provide valuable insights into the gene expression profiles of these cell lines, contributing to a comprehensive understanding of their molecular dynamics and potential implications for cellular physiology.

6.2 System design

We have developed a prototype system from scratch to achieve our research objectives. The system comprises both hardware and software components. For the hardware part, we assembled the system containing a SPAD camera, fluidics system, optical path and a laser module and integrated them into a functional setup. To facilitate real-time data analysis, we developed our own software part using MATLAB. The software system is designed to acquire and process TCSPC data from the SPAD camera in real-time and includes modules for signal processing, data visualisation, and statistical analysis. One of the main challenges in developing the software part was ensuring its compatibility with the hardware components and optimising its performance to enable real-time data analysis. To address these challenges, we used a combination of hardware and software optimisations to achieve high-speed data acquisition and processing of a reference sample such as fluorescent beads.

6.2.1 Hardware development

Figure 6.2 and Figure 6.1(B) show the photograph of the FCM system which is based on the wide field microscope setting. The platform composes of three main parts: fluidics, optics, and electronics. For fluidics, the sample and sheath fluid are simultaneously injected into a microfluidic chip by a syringe pump (NE300, Jaytee, UK) and a peristaltic pump (Multiflow, Lambda Instrument, Switzerland) to establish hydrodynamic focusing, which narrows down the sample stream to pass the laser illumination area uniformly [22]. The sample flow rate is set to 10 µl/min. The flow cell follows a 210 x 70 um microfluidic chip (Figure 5.4), manufactured by microfluidicChipShop (Jena, Germany).

For optics, Figure 6.1(A) shows the system and optical path based on a wide-field microscope setup equipped with the SPAD sensor. A pulsed laser system (Deltadiode, Horiba) with a wavelength of 640 nm and a repetition rate of 10 MHz, is employed to excite the sample within the flowcell, which is placed in the field of view (FOV). The excitation is passed through a combination of a dichroic mirror (Dichroic 660 nm, Edmund Optics), which reflects the pulsed laser, and a 20x objective lens (PLN20X, NA = 0.4, Olympus) that focuses the laser beam onto the sample. The excitation pulse width is controlled to be less than 200 ps to ensure precise temporal excitation. Subsequently, the fluorescence signal emitted by the sample is collected through the same dichroic mirror, along with a long-pass emission filter 665 nm.

In electronics, a 192x128 TCSPC SPAD imager array (STMicroelectronics 40-nm CMOS technology) captures the single photon and builds up the fluorescence decay. The sensor is configured as a megapixel (combine data read out of all pixels into a single fluorescence

decay), therefore one captured frame detects 24,576 photons that work in parallel. 3 ms and 0.5 ms exposure time are selected for long and short exposure time setting. As shown in Figure 5.20 and Figure 6.10, the optimal setting for the highest detection rate is 3 ms, while 0.5 ms is ideal for image generation, offering low motion blur and still maintaining a high detection rate. The acquisition time is set to 3 ms and 0.5 ms for long and short exposure times, respectively. The electronic design of the array was reported in [47]. However, the sensor still has limited sensing performance affected by a high dark count rate, bad pixels and non-uniform timing. Therefore, the sensor calibration has been run before the measurement. The electrical design and initial chracterisation of the SPAD has been reported in [47], [58]. The time resolution of the system is fixed at 39.7 ps. The sensor is controlled by our homemade software based on Matlab through firmware based on Verilog code from our collaborator at the University of Edinburgh [124].

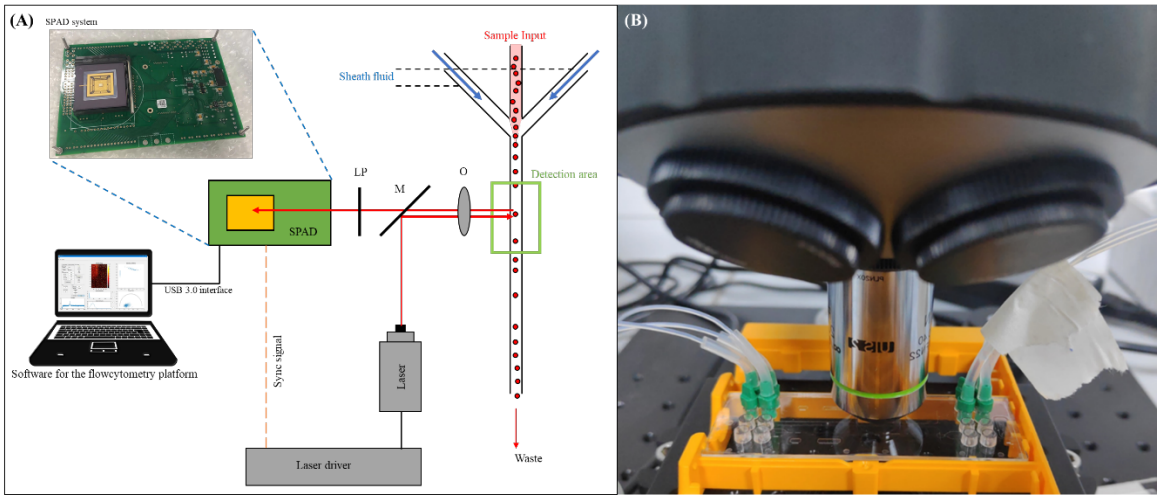

Figure 6.1 Overview of the FCM system. (A) The sample and sheath fluid is injected into the flow cell by syringe and a peristaltic pump, respectively. The optical path composes of an objective lens (O), dichroic mirror (M) and LP filter (LP). The laser driver triggers a pulsed laser to excite the sample and synchronise with SPAD. The measured multi-parameters are shown in the GUI. (B) Photograph of the experimental setup showing flow cell and objective lens that collects the fluorescence signal

Figure 6.2 Photograph of the lifetime FCM prototype.

6.2.2 Software development

A homemade interactive software based on MATLAB has been developed to perform real-time analysis including phasor plot, CMM, and intensity image for flowing cells or particles (Figure 6.3). The interface was drawn using the interactive GUIDE tools in Matlab, while the commands in each button were specifically written in the Matlab terminal. Additional software is required to operate the camera smoothly such as FrontPanel (Opal Kelly, US) for Windows' driver and C-complier (TDM-GCC) software for C-language Matlab operation.

To start using the software, the user is required to click the "Connect FPGA" button, which plays an important role in establishing a connection with the SPAD camera. This step is necessary for enabling communication between the software and the camera. Once this action is completed, the firmware will be written into the FPGA memory, enabling the software to interact with the camera. Subsequently, the user has the ability to customise various parameters, including: (1) selecting the internal or external trigger signal source; (2) choosing operation modes—photon counting mode for intensity imaging or TCSPC mode for lifetime FCM experiments; (3) defining exposure time, specified as the time period for each pixel to acquire the incoming single photon, with subsequent photons being neglected until the next exposure time period; (4) determining the measurement window, which starts from the (CMM start)th bin to the (CMM start + Window Width)th bin, where the width is four times the expected lifetime; (5) setting H and L thresholds as higher and lower intensity boundaries; any intensity values outside this range will be neglected; (6) using the "Save IRF" function to perform 1000 continuous frame measurements with samples for IRF measurement, such as

urea crystal, and saving the results as an IRF file for further use. This file can be loaded using the "Load IRF" button. By customising these settings, users can optimise the software's functionality to meet their specific requirements.

After the experimental parameters have been set, the users can use two measurement buttons to initiate the measurement process. (1) The “Realtime Measurement” area will perform the live imaging with real-time analysis where the data are collected for a certain number of frames (defined by the user), multi-parameter analysis and display at once to improve the measurement speed as MATLAB can be slowed down due to tasks related to graphical processes such as plotting graph and image processing. This feature allows the user to observe and analyse the data as it is being acquired. (2) The “Fast Measurement” is designed to maximise the number of events recorded per second. However, it lacks the capability to display real-time data during the measurement process. This mode will command the SPAD camera to continuously perform the measurement until the number of user-defined frames is reached, however, the number of frames must be n-times 500 frames due to the memory limitation on the SPAD camera. Moreover, the software offers the option to save the recorded data in “.FCS” format. This file format adheres to the standards set by commercial flow cytometers and is compatible with a wide range of paid and free software tools available for further data analysis [125] enhancing interoperability and facilitating collaboration within the scientific community.

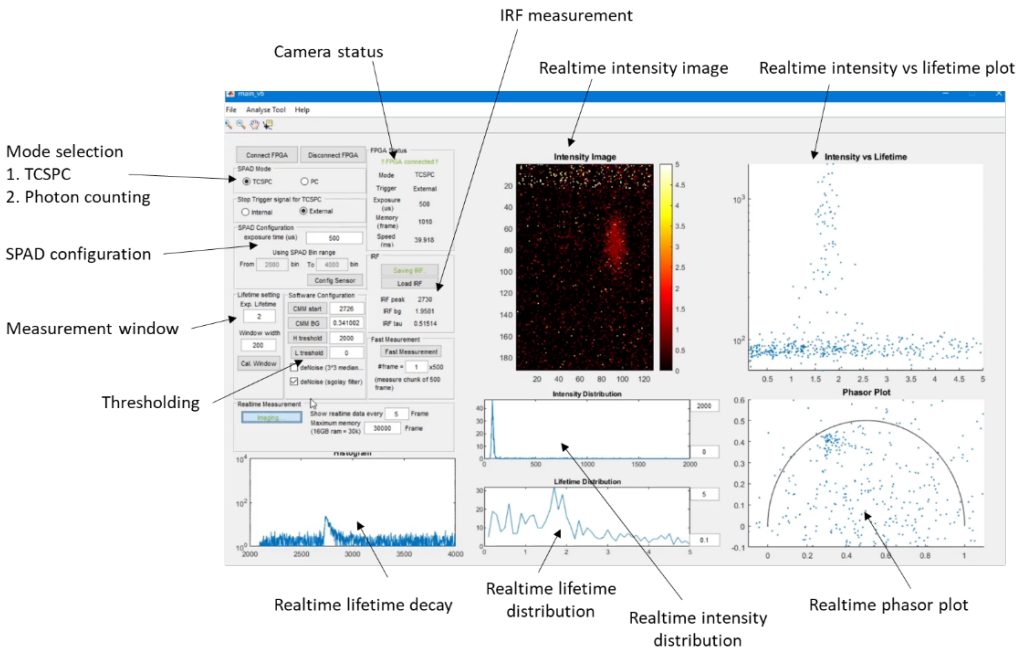

Figure 6.3 Screenshot of developed graphical user interface software showing the ability to control the camera settings and to display multiple real-time analyses.

The working cycle of the software is shown in Figure 6.4. After data feed from the camera that detects incoming emitted photons, a correction process has been performed before megapixel integration. The intensity of each frame is determined by the total photon in the measurement window. An intensity threshold is selected by the user to distinguish between frames with and without particles. The frame outside the threshold is neglected, while only the frame within the threshold is further analysed by CMM and phasor plot. The analysed data is temporally stored in the RAM of the PC and displayed in the GUI. The software also offers hand-free gated ROI for extracting rare events from phasor plots or fluorescence lifetime-intensity plots.

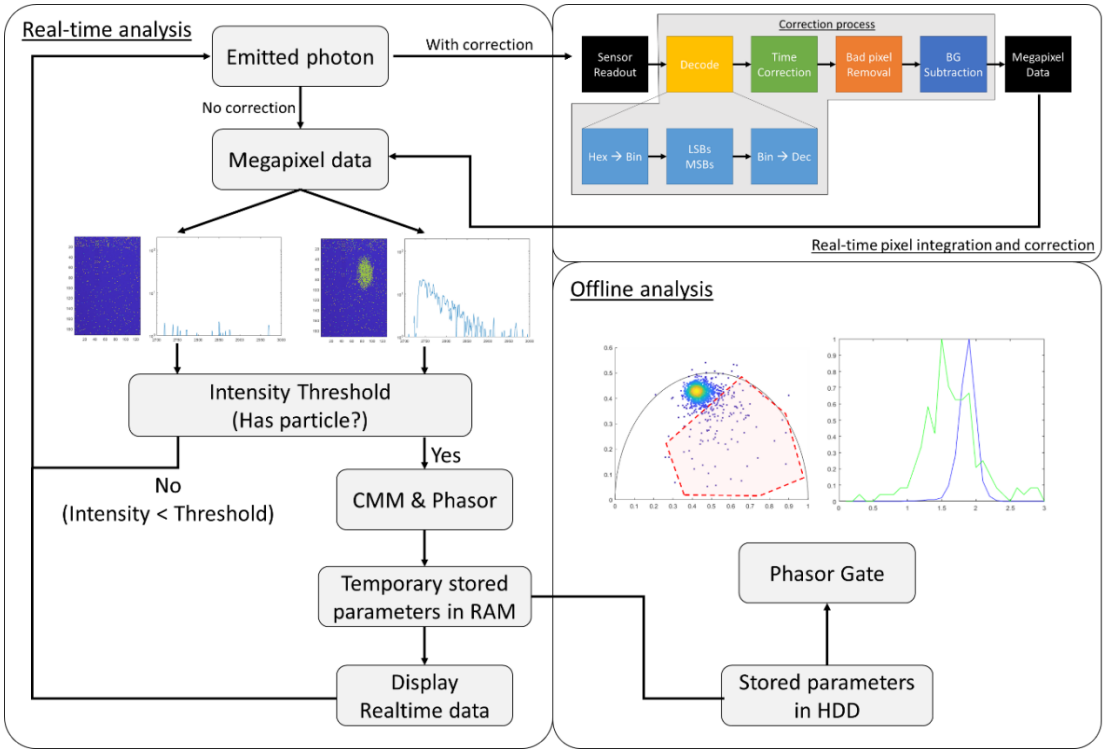

Figure 6.4 Working cycle of the platform.

6.3 Sample Preparation and reference measurement

6.3.1 Latex microsphere

Yellow-green (YG-bead) and crimson fluorescent beads were purchased from Thermofisher (F8831 and F8836, FluoSpheres™ Polystyrene Microspheres, 10 µm). The bead's diameter and density are 10 µm and 3.6×10^5 beads/ml, respectively. Due to the bead's density of 1.055 g/cm^3, which is heavier than water, it can precipitate to the bottom of the container after sometimes causing concentration changes during injecting process using a syringe pump. Therefore, the beads were suspended in a suspending media prepared from 20% glycerol solution to match the density and using viscosity to slow down the sedimentation process.

The reference fluorescence lifetime of the beads has been measured with FluoroCube (Horiba). A 640 nm pulsed laser (DeltaDiode, Horiba) is used as an excitation pulse operating at a 10MHz repetition rate, while the fluorescence emission is collected at 90° to the excitation through a polariser at the magic angle using a monochromator at 670 nm with 32 nm width and a PMT (Horiba). The beads are filled and measured in a 100µl quartz cuvette. The IRF is obtained by measuring colloidal silica solution (LUDOX® AS-40, MERCK) with an ND filter and without an emission filter. The fluorescence lifetime is calculated by the deconvolution process using commercial lifetime analysis software (DAS6, Horiba). The fluorescence decay of the C and YG beads is shown in Figure 6.5. For C-bead, the lifetime fits well with the two-exponential fitting with $X^2 = 1.16$. τ_1 and τ_2 values are 1.08 ± 0.02 and 2.84 ± 0.01 ns, while A_1 and A_2 are 46.52% and 53.48%, respectively. The average lifetime is 2.02 ± 0.01 ns calculated by weighted relative amplitude using Equation 6.1. For YG-bead, the fitting process has been performed using the three-exponential model with $X^2 = 1.02$ with τ_1, τ_2 and τ_3 values of 0.01 ± 0.00, 0.62 ± 0.01, and 2.87 ± 0.01 ns, respectively. The average lifetime is weighted by relative amplitude of $A_1 = 34.89\%$, $A_2 = 25.52\%$, and $A_3 = 39.59\%$, giving the value of 1.30 ± 0.01 ns.

$$\bar{\tau} = \frac{A_1\tau_1 + A_2\tau_2 + A_3\tau_3}{A_1 + A_2 + A_3} \tag{6.1}$$

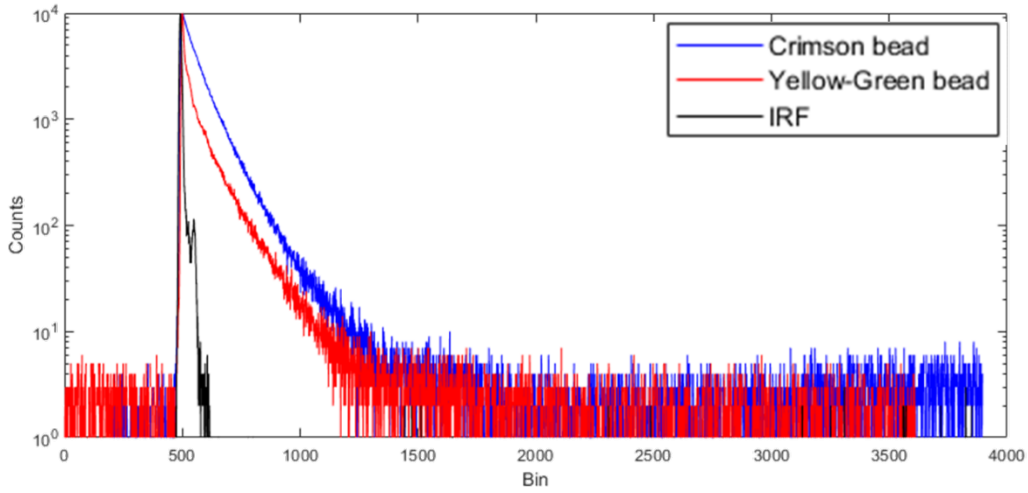

Figure 6.5 Time-resolved fluorescence decay of C-bead, YG-bead and IRF measured by FluoroCube. The excitation is 640nm Delta diode laser and

6.3.2 Finding the optimal exposure time

The lifetime measurement needs the appropriate intensity threshold and enough data acquisition time. However, there is an unavoidable compromise between exposure time and

flow speed. Higher flow speed can improve the FCM's throughput, but this will dramatically decrease exposure time which can increase statistical error. Therefore, it is important to find optimal experimental conditions to maximise the detected event number in minimum acquisition time.

6.3.2.1 Particle speed

The analysis of particle speed is crucial, and in this study, it was accomplished by employing image blur effect analysis [126]. This approach involves the registration of an image in movement, while the camera shutter remains open. Due to the movement of the bead, the bead TCSPC image is affected by motion blur causing the bead image to elongate along the velocity direction Figure 6.6. In this measurement, the C-bead particle was focused by injecting it into the flow cell at a flow rate of 10 µl/min, while the sheath fluid was driven at 62.6 µl/min to narrow down the sample stream diameter to 55 µm. The diameter of the C-bead was 10 µm, provided by Thermofisher. The flowing bead image was captured by a SPAD camera operating in TCSPC mode with a 500 µs exposure time, showing a 192 x 128 pixels image of the collected data consisting of the time bin number of the SPAD. This experiment aims to accurately estimate particle speed and provides valuable insights for the following measurement. The particle velocity (v) can be extracted using Equation 6.2 where $d_{particle}$ is particle diameter, t is exposure time, and D is the mode of the length of the blurry particle which is statistically determined from all detected events during the exposure time.

$$v = \frac{(D - d_{particle})}{t} \tag{6.2}$$

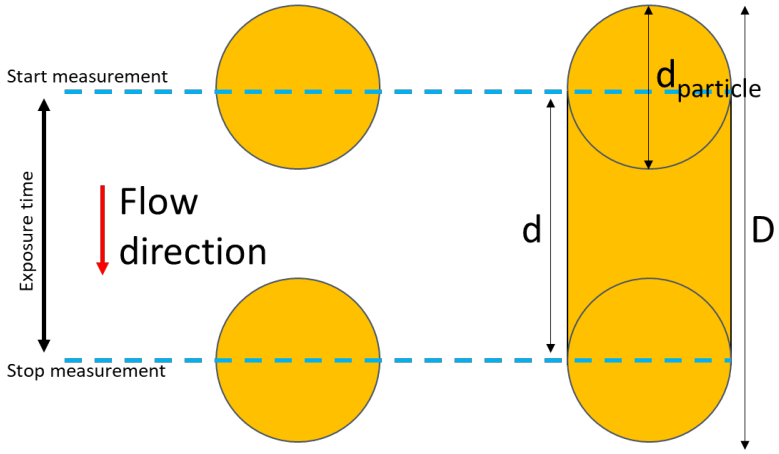

Figure 6.6 Schematic diagram showing the generation of blurry image

In this study, we present the results of our analysis of single particle tracking using TCSPC data obtained from a single frame of the SPAD camera as shown in Figure 6.7. Our analysis

focuses on the behaviour of a single particle, which appears as a blurry image in the acquired frames. We have performed 30,000 measurements and applied a time-gate and noise reduction using a median filter to filter out noise. After applying an intensity threshold of 1,000 counts to remove frames with half-particle appearing, we identified 440 events that passed the threshold. The length of the blurry particle was calculated to be 62 pixels or 27.90 µm, which can be converted to a travelling distance of 17.90 µm during the 500 µs exposure period. Based on this measurement, the velocity of the particle was determined to be 35.78 µm/ms. Furthermore, we found that the particle appeared in the field of view within 2.41 ms for vertical flow direction. Our results suggest that the use of TCSPC data from SPAD cameras, coupled with appropriate blurry image analysis techniques, can provide particle speed within a single frame.

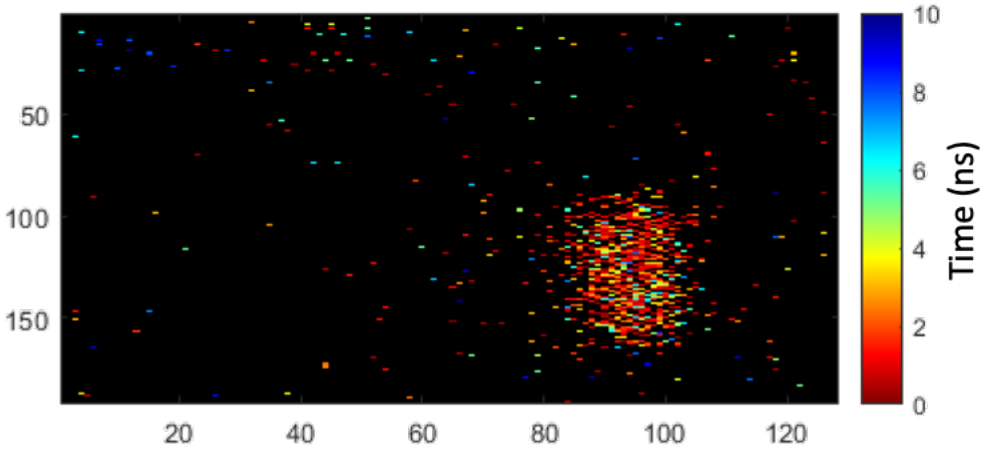

Figure 6.7 An image generated from a single frame from TCSPC mode of the SPAD array. The pixels are colour-coded indicating the time of the detected single photon.

6.3.2.2 Dead time

Another parameter needed to be considered is the dead time (ΔT) between frames where the SPAD camera cannot detect the new particle. This dead time is different from the dead time of the single photon counting process [59] but it involves limitations from data transferring and decoding between FPGA and PC, and the data analysing speed in MATLAB. In this study, two rapid approaches of lifetime analysis: CMM and phasor plot have been used in this study. The measurement speed of one frame is defined by the total time taken from the start of measurement until the end of the analysis (t_{total}), however, this time is always longer than exposure time ($t_{exposure}$). The dead time is defined by $\Delta T = t_{total}-t_{exposure}$, while $t_{exposure}/t_{total}$ is the sensing ratio that indicates the ratio of the detected event to the total amount of sample and a higher ratio ($t_{exposure}/t_{total} > 0.9$) implies most of the sample can be detected.

To characterise this ΔT, the SPAD camera is configured with various $t_{exposure}$ to measure dark count, while the t_{total} is measured from the built-in timing function in MATLAB. Then the ΔT is calculated by averaging the ΔT from the 2nd to 100th frame (the 1st frame always spend a significantly longer time due to the initialisation of the camera). Figure 6.8 shows the relationship where the value of ΔT is inversely proportional to $t_{exposure}$. The ΔT drops dramatically when the exposure time exceeds 1.5 ms and this greatly improves the detection rate. The exposure time for this work is set to 3 ms, which equals to 309 fps, corresponding to ΔT = 236 µs and $T_{exposure}/t_{total}$ = 0.927 to minimise miscounted particles. The platform could perform up to $T_{exposure}$ = 100 µs, which equals 1147 fps or T_{total} = 872 µs per frame of detection rate. However, this maximises dead time (ΔT = 0.772 ms) and reduces sensing time to only 11.5% ($T_{exposure}/ t_{total}$ = 0.115) of T_{total}.

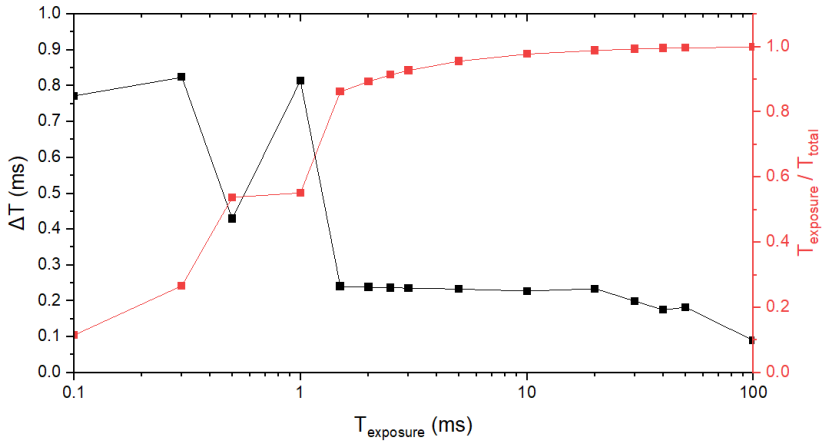

Figure 6.8 ΔT and $T_{exposure}/T_{total}$ measured in different exposure time setting

6.3.2.3 Recognising single or multiple particles presented in the FOV

In this study, we highlight the potential issue of multiple particles appearing in the field of view simultaneously due to the larger diameter of the focused stream. To address this, we develop an algorithm that extracts only frames with a single particle based on a technique introduced by Gonzalez [127]. The algorithm involves applying a 2D-median filter and a connectivity threshold to filter particle size, followed by counting the number of particles appearing in the TCSPC frame using the "bwboundaries" command, which is a built-in function in the MATLAB Image Processing Toolbox. By isolating frames with a single particle, we can improve the accuracy and reliability of our experimental results.

The testing has been first performed on a static C-bead measurement to demonstrate the algorithm. The experimental process involves the preparation of a C-bead microscope slide by a 10 µl drop of C-bead on a glass slide, followed by covering it with a circular cover slip.

The prepared slide is mounted in the flow cell position for analysis. A single TCSPC frame showing two static C-beads in the same FOV captured from the C-bead microscope slide has been selected, as shown in Figure 6.9(A). However, the determination of particle boundaries can be less accurate due to the presence of high levels of noise. To resolve this issue, a 2D median filter was applied to every pixel, whereby each output pixel contains the median value in the 3-by-3 neighbourhood around the input pixel. The resulting image (Figure 6.9(B)) exhibits clearer C-bead boundaries compared to the initial image (Figure 6.9(A)), with the yellow pixels indicating the C-bead particles. Lastly, the number of particles is determined by closed boundaries after applying the connectivity threshold (Figure 6.9(C)), which is defined by the number of neighbouring pixels surrounding the C-bead in every direction. For slow or static particles, the threshold is set to 300 pixels, while it can be up to 800 pixels for elongated particles due to motion blur.

In order to accurately recognise and quantify multiple particles in a flowing stream, an experiment was conducted using the setup depicted in Figure 5.18, both with and without sheath fluid. The experiment involved injecting C-Beads with $1.8x10^5$ beads/ml density at a flow rate of 10 µl/min, while the sheath fluid was driven at a flow rate of 62.6 µl/min. To minimise motion blur, the exposure time was set to 0.5 ms, while a 3 ms exposure time was used to minimise the dead time and increase the detection rate. The measurement was performed by capturing 30,000 continuous frames. This approach ensured that only single particles were captured and analysed. Moreover, we applied the algorithm on both short and long exposure times in the detection of particles with and without sheath flow, thereby allowing for a comprehensive analysis of the particle stream.

Figure 6.10 illustrates the results of the image processing procedure, wherein the 2D median filter was applied to a single frame of TCSPC mode. The yellow pixels in the figures represent the particle area. Specifically, Figure 6.10(A and C) show images captured with 0.5 and 3 ms exposure time, respectively, without the sheath fluid. Meanwhile, Figure 6.10(B and D) show the same images with the sheath fluid. To quantify the number of particles in the FOV, we used the developed algorithm and presented the results in a column plot in Figure 6.11. The plot shows that with a 3 ms exposure time, the developed algorithm detected 1,693 events (comprising 1639 single, 53 double, and 1 triple particle in FOV) without sheath flow and 1940 events (comprising 1910 single and 30 double particles in FOV) with the sheath flow. On the other hand, with a 0.5 ms exposure time configuration, the algorithm detected a lower number of particles, specifically 747 events (comprising 725 single and 22 double particles in FOV) without the sheath fluid and 761 events (comprising 757 single and

4 double particles in FOV) with the sheath fluid. The observed difference in the number of detected particles between the 3 ms and 0.5 ms exposure time configurations can be related to the dead time. Specifically, the longer exposure time in the 3 ms configuration leads to a higher probability of detecting more particles. However, due to the longer data acquisition time, there is also a higher chance of observing multiple particles appearing in the same FOV. Furthermore, the presence of sheath fluid also helps to detect more single particles. Without the sheath fluid, there are no forces to narrow down the sample stream, and multiple particles can appear in the image without any focusing effect. After introducing the sheath flow, a higher proportion of single particles can be observed. This is because the sheath fluid narrows down the sample stream and helps in focusing the particles, making it easier to distinguish individual particles in the captured images. Therefore, the use of sheath fluid in the experimental setup can significantly improve the accuracy and reliability of particle detection and analysis.

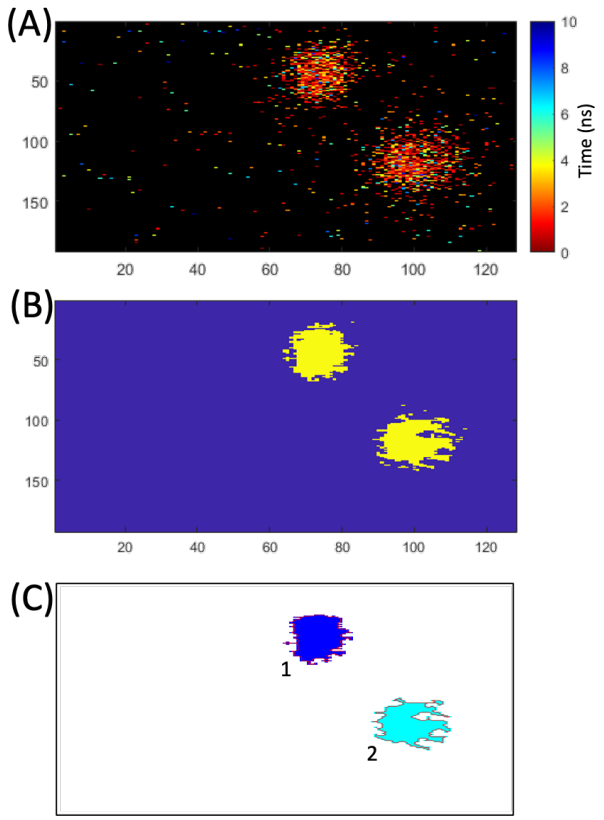

Figure 6.9 Static C-bead measurement to test distinguishability of multi and single particle of the algorithm (A) Colour-coded image from the single TCSPC frame showing the arrival time of the single photon in each pixel, (B) Particle mask indicated by the yellow colour pixel after applying the 2D medial filter, (C) Two closed boundaries from different particles determined from the algorithm indicated by dark- and light- blue colour.

This filtering method can be further used in other cases such as high particle concentration or varying sheath fluid viscosity, which affects the occurrence of multiple particles. The concentration of particles relates to the number of particles present per unit volume, while the viscosity of the sheath fluid refers to its resistance to the flow. Both factors can have a significant impact on the visual appearance of multiple particles in the system. The flow rate within the system is inversely proportional to the viscosity [128]. Consequently, if the viscosity of the sheath fluid does not match with the conditions under which the calibration was performed (typically using water at room temperature), the peristaltic calibration may yield inaccurate results, and this can lead to a not-focused sample stream. In the case of particle concentration, the prototype works with an approximate particle density of $2x10^5$ particles/ml, which is a common concentration observed in cells incubated with the RNA nanoprobe [29]. By increasing the concentration of particles, the probability of encountering multiple particles within the FOV also increases due to particle overlap or clustering.

Overall, this experimental approach provides a reliable and comprehensive method for quantifying and characterising multiple particles in a flowing stream. The developed algorithm presented in this study provides an effective means of distinguishing and quantifying multiple particles in the field of view. The use of a 2D median filter in the image processing step helped to reduce noise and improve the accuracy of particle detection. The results of our experiments demonstrate that the use of sheath fluid can significantly reduce the occurrence of multiple particles in a single field of view, while longer exposure times can increase the detection rate. Therefore, 3 ms exposure time combined with the algorithm will be used in further experiments to provide a maximum particle rate with the capability in distinguishing single particle events.

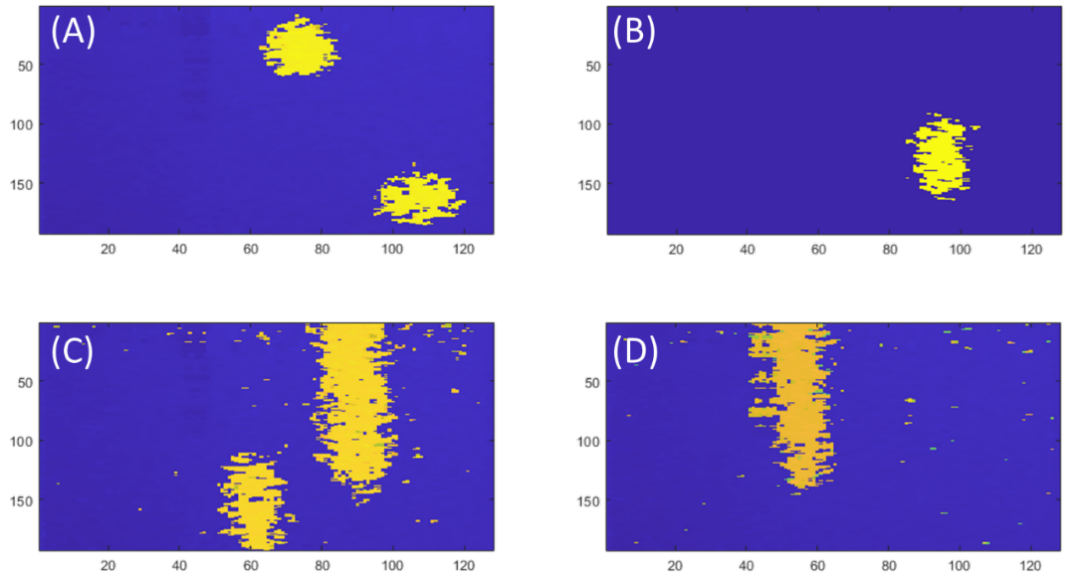

Figure 6.10 Particle mask image where the yellow pixels indicate the particle area. All images are generated by applying the 2D median filter on a single TCSPC frame. Each image is acquired from a different system configuration: (A) 0.5 ms without sheath, (B) 0.5 ms with sheath, (C) 3 ms without sheath, and (D) 3 ms with sheath.

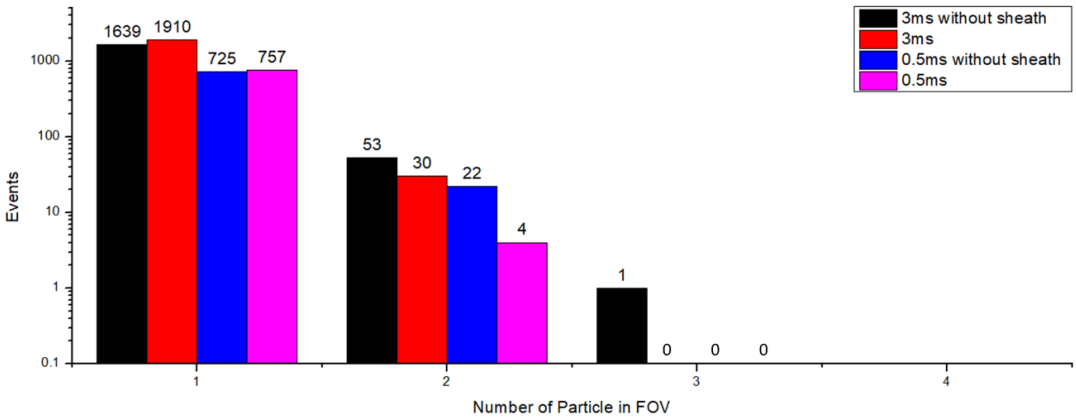

Figure 6.11 Distribution plot of the number of particles appearing in the FOV generated after applying the algorithm 30,000 TCSPC frames. The system was configured with 0.5 ms without sheath (blue), 0.5 ms with sheath (purple), 3 ms without sheath (black), and 3 ms with sheath (red).

6.4 Fluorescence lifetime measurement of flowing sample

6.4.1 Background measurement

In this study, a background measurement was conducted by analysing sheath fluid for 20,000 events. The experimental setup involved using a peristaltic pump to inject PBS buffer or

distilled water at a flow rate of 62 µl/min, with the syringe pump disabled during this measurement. The measurement initiates when the sheath fluid completely fills the flow cell.

A 640 nm Delta diode with a 10 MHz repetition rate served as the excitation source through a fiber optics cable. The background signal was collected through a dichroic mirror and an emission filter at 665 nm. The intensity was calculated based on the total photons in a 200-bin measurement window. The measurement revealed a low-intensity value of 253.59 ± 11.59 counts for PBS and 253.92 ± 58.76 counts for water.

6.4.2 Opened nanoprobe on a glass slide moved by a micrometre

Before proceeding to the precious sample, the developed system is tested with a static nanoprobe on a microscope slide. The primary feature that distinguishes this FCM development is its ability to measure both the fluorescence lifetime and intensity of the RNA nanoprobe within the cellular environment. Specifically, the system is designed to detect the opened nanoprobe, which is indicative of the presence of the target RNA. The initial test was performed using static nanoprobes mounted on a microscope glass slide.

To conduct this experiment, a volume of 15 µl of the nanoprobe with a concentration of 0.4 nM was incubated with cDNA for 2 hours. The hybridisation of cDNA with RNA nanoprobes opens the hairpin. The opened probe was dropped onto a glass slide and subsequently covered with a cover slip. The slide was then positioned under the objective lens. A total of 65,000 frames were taken using the developed software, and the SPAD was configured to have an exposure time of 3 ms, while the glass slide is being manually moved through a micrometre attached to the microscope stage to mimic the flowing of the nanoprobe.

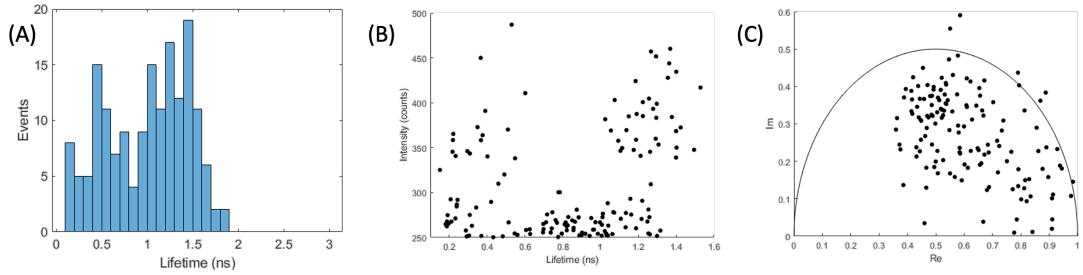

Figure 6.12 Schematic plots generated from the measured data of open-nanoprobe on a glass slide showing (A) fluorescence lifetime distribution, (B) fluorescence lifetime against fluorescence intensity plot, and (C) phasor plot.

Given the nanoprobe's small size [18], which is below the SPAD camera pixel size, and its concentration in the nM range, the collected fluorescence signal reflects the average signal from the entire field of view. The study demonstrates the lifetime distribution of a nanoprobe

on a glass slide, as shown in Figure 6.12(A). The calculated average lifetime of the nanoprobe is 0.90 ± 0.53 ns when using a lower intensity threshold of 250 counts. Figure 6.12(B) illustrates a scatter plot indicating two population groups with short lifetimes (< 0.5 ns) and long lifetimes (> 0.5 ns). The short lifetime population were recognised as the presence of air bubble or scattering from the gold. For the longer lifetime part can be classified as quenched Cy5 and unquenched Cy5 indicated by low fluorescence intensity (< 300 counts) and high fluorescence intensity (> 300 counts). The increase in the intensity is associated with a reduction in FRET efficiency, resulting in an increase in fluorescence lifetime and intensity, as expected when the hairpin opens [17]. Furthermore, a phasor plot is shown in Figure 6.12(C), where the position of Re > 0.4 within the semicircle indicates that the fluorescence decay from the nanoprobe follows a multi-exponential model. These findings suggest that the lifetime distribution and phasor plot analysis can provide insights into the behaviour and performance of the nanoprobe and can serve as a reference measurement to compare the performance of the nanoprobe inside the cell in further experiments.

6.4.3 Flowing Latex bead lifetime measurements

The most important feature of the FCM is rare event detection. This allows researchers to identify and quantify rare cell populations or events that may be critical in diagnosis and treatment. For example, rare tumour cells can be identified and studied using flow cytometry by differentiating fluorescence intensity from RNA nanoprobe [29]. In the real cell screening in conventional FCM, there are generally two types of samples which are positive and negative, that show different fluorescence or scattering profile. In this study, fluorescence lifetime is introduced as the new indicator for cancer cell screening using the RNA nanoprobe. To test the feasibility of the system to differentiate different populations, two types of fluorescent beads are used to mimic cancer and healthy cells incubated with the RNA nanoprobe. The C-bead exhibits a positive event which has high fluorescence intensity, while the YG-bead shows a weak intensity level representing a negative sample. After testing with a single type of bead, the system is then injected with the mixed bead solution to test the differentiation performance. The beads are excited by a 640nm 10 MHz pulsed laser, while the emission is collected through a 20x objective lens (N.A. = 0.4) and 665 nm long pass filter. To avoid the miscounted event and errors in counting, the flowcell is cleaned by flowing only sheath fluid for 15 minutes between samples.

6.4.3.1 Single-type particle (C-Bead)

Fluorescence lifetime detection of a single type of flowing bead is performed by injecting C-bead into the flow cell and focused by water into a single particle stream. Measured and

calculated parameters, intensity images, and data plots are displayed in real-time in the GUI. The measurement and calculation take 3.2 ms per frame. The intensity of each bead particle is determined by the total photon in the measurement window subtracted by the background value. The average intensity of the C-bead is 1,712 counts. An intensity threshold of 500 counts is used to distinguish between frames with and without beads giving 2,773 detected beads. This is comparable to 96.28% of the expected event number (N_{expect}) of 2,880 events calculated by multiplication of C-beads density (ρ), the injection rate (f_{sample}) and total injection time (t) as written in Equation 6.3. The fluorescence lifetime of the C-bead is calculated by CMM and phasor plot within a measurement window of 200 bins starting from the peak position of the decay. The C-bead shows a narrow lifetime of 1.90 ± 0.13 ns with FWHM 0.1 ns, which is comparable to our reference measurement and a previous report [58].

$$N_{expect} = \rho t f_{sample} \tag{6.3}$$

Figure 6.13 is the experimental result of flowing C-bead measured for 30,000 frames. Figure 6.13(E) shows a single flowing bead generated from a single frame where the coded colour indicates the time bin of the detected single photon of each pixel. Figure 6.13(A) is the fluorescence decay of the frame with and without C-bead generated from a megapixel, and this shows the platform is well calibrated and can generate the decay from only a single frame. However, the lifetime distribution relies on the photon counts and is broadened for low photon count frames, as shown in Figure 6.13(B). The C-bead lifetime is 1.93 ± 0.24 ns for intensity < 1,000 counts, and 1.89 ± 0.10 ns for intensity > 1,000 counts. Figure 6.13(C) is a phasor plot of measured data showing a clear single population with a multi-exponential lifetime indicated by the dot position inside the semicircle. Figure 6.13(D and E) are the intensity and lifetime distribution of the detected events with a lower intensity threshold of 1,000 counts.

6.4.3.2 Single-type particle (YG-Bead)

The YG-beads, having the same diameter as C-beads, demonstrate weaker fluorescence intensity and a shorter lifetime when excited by a 640 nm laser. To ensure accurate detection, an intensity threshold of 285 counts is applied to cut off the background, eliminating frames without the YG-bead presence. However, the resulting detection of 440 beads, corresponding to approximately 15.28% of the expected event number, indicates a low particle detection rate in the flowing YG-bead measurement. This can relate to the overlapping fluorescence intensity of the beads with the background intensity, which has the value of 253.92 ± 58.76 counts for water, and the threshold is not the clear cut-off value between the background and

YG-beads. This suggests that the applied intensity threshold is not suitable for precise counting of YG-beads. Further investigation and alternative strategies such as the usage of the microlens and sensor cooling system are planned to be used to improve the accuracy of YG-bead quantification in future studies.

Figure 6.14 shows the experimental results of flowing YG-beads measured for 30,000 continuous frames. Figure 6.14 (A) shows the fluorescence decay when the YG-bead appears in the field of view. Figure 6.14(D and E) are the fluorescence intensity and lifetime distribution plots which can be generated to the scattering plot as shown in Figure 6.14(B). This plot shows that the YG-bead generally have a weak intensity plot and the most lifetime ranging from 0.8 to 1.5 ns. The average intensity of YG-beads is measured to be 317.51 counts, while the average fluorescence lifetime value is determined to be 1.49 ± 0.66 ns. Moreover, this lifetime value is consistent with the phasor position where the plot appears in the short lifetime region in the bottom right corner of Figure 6.14(C).

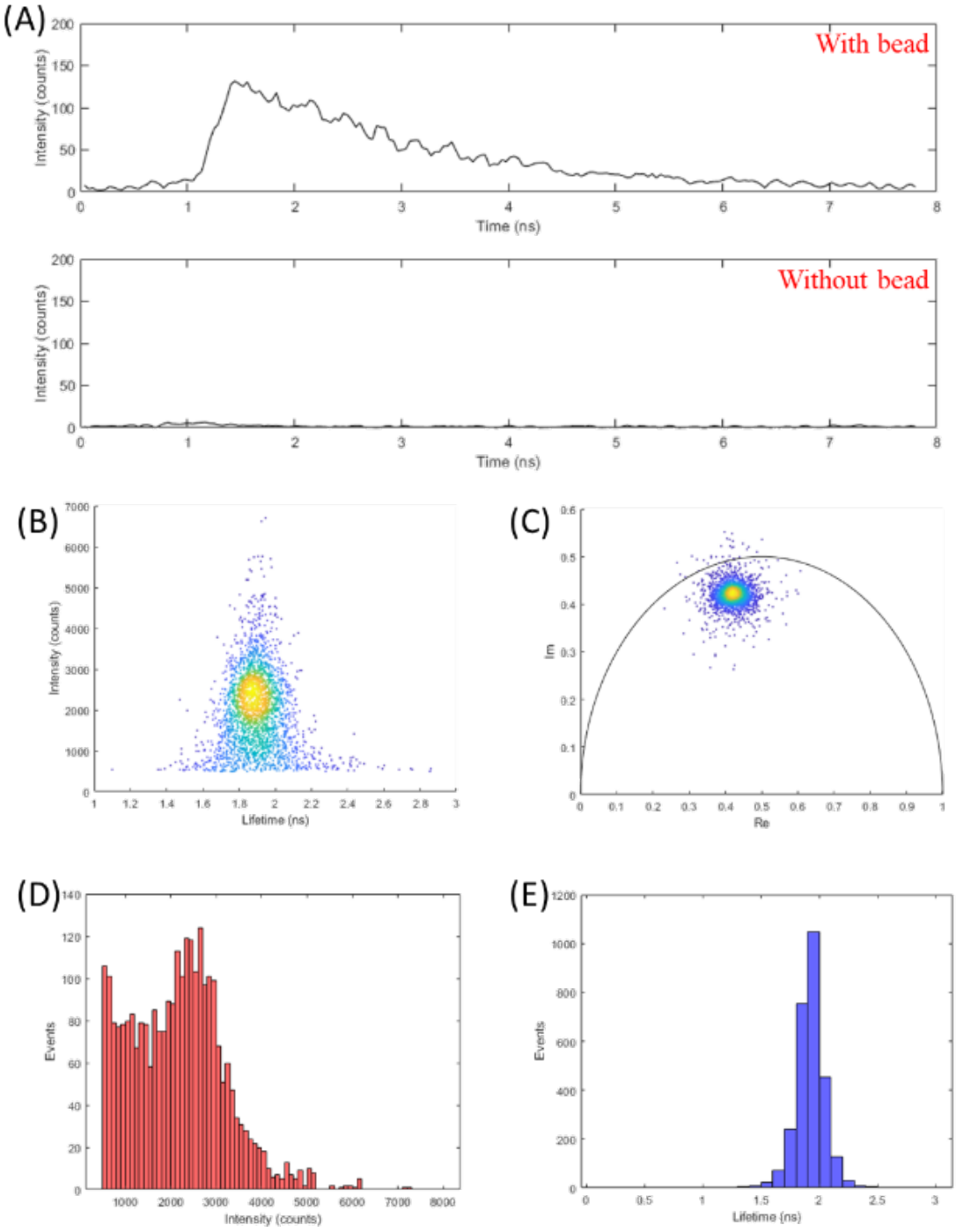

Figure 6.13 Experimental setup for flowing C-bead: (A) Fluorescence decay generated from a single frame with and without C-bead. (B) 2D scatter plot of lifetime against intensity. (C) Phasor plot generated from every detected event. In (B) and (C), the color-coded dots represent the density of the dots, with yellow and blue indicating high and low density, respectively. (D and E) are intensity and lifetime distribution plots, respectively.

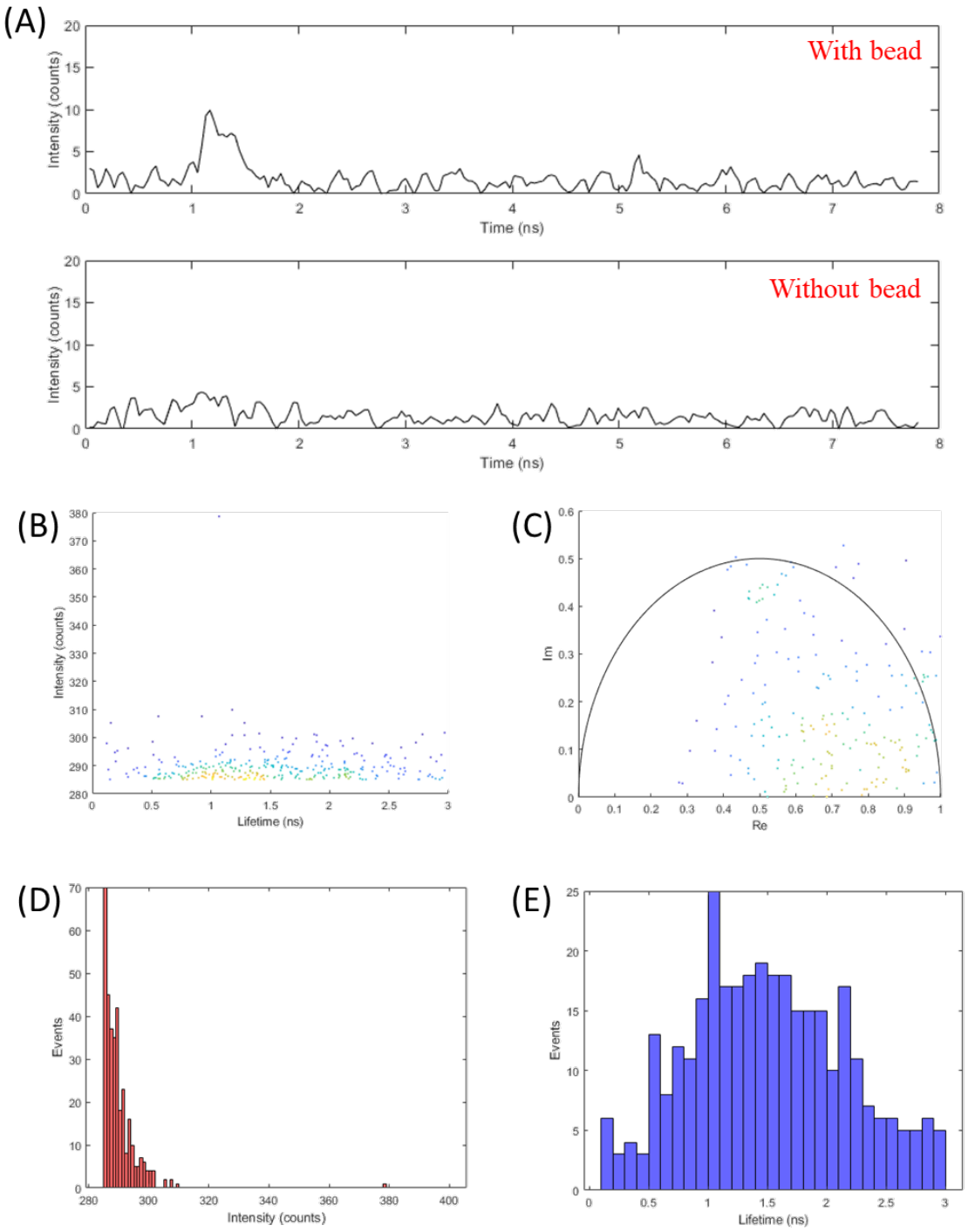

Figure 6.14 Experimental of flowing YG-bead. (A) Fluorescence decay is generated from a single frame with and without C-bead. (B) 2D scatter plot of a lifetime against intensity (C) Phasor plot generated from every detected event. In (B) and (C), the color-coded dots represent the density of the dots, with yellow and blue indicating high and low density, respectively. (D and E) are intensity and lifetime distribution plots, respectively.

6.4.3.3 Mixture of two types of fluorescent microspheres (C- and YG- Bead)

The developed system has shown the capability of detecting high and low-intensity fluorescent beads (C-bead or YG-bead, respectively). In the real world, FCM is used to identify and separate different populations of cells or particles in a mixed sample using their unique properties, for example, fluorescence lifetime and location of phasor plot. However, this detection is challenging due to the low number of rare events such as circulating tumour cells and the high level of background noise from other cells or particles present in the sample FOV. To overcome these challenges, data analysis techniques such as intensity threshold, phasor and lifetime time gate can be applied to quantify rare events in the FCM dataset of the mixed sample. In this experiment, a mixture of C- and YG- beads with a ratio of 1:1 and a total density of $3.6x10^5$ particle/ml is injected into the flow cell with a flow rate of 10 µl/min, while water is used as the sheath fluid and driven into the flow cell with the flow rate of 62.6 µl/min to focus the sample stream down to 55 µm. The data acquisition was performed for 30,000 continuous frames.

Figure 6.15(A and B) shows the overlapping plot between Figure 6.13 and Figure 6.14, which are single-type bead measurements. In order to distinguish the lifetime between these two types of beads, two intensities thresholds are set to filter YG-bead (285 – 500 counts) and C-bead (>501) counts, while the frame with intensity below 285 counts will be neglected. Moreover, the phasor position of the C-bead Figure 6.15(C) is used as a reference where the phasor position outside this area is counted as YG-bead as shown in the red area in Figure 6.15(B). By using these two gating conditions, the fluorescence lifetime of each can be extracted, as shown in Figure 6.15(C and D), showing 1.87 ± 0.13 ns and 1.64 ± 0.43 ns lifetime of C- and YG- beads, respectively.

This experimental observation highlights the importance of hydrodynamic focusing and the potential challenges related to accurately measuring the fluorescence lifetime of the weak fluorescence intensity sample within a mixed sample. The presence of strong fluorescence intensity species can introduce interfering factors. The fluorescence lifetime analysis of the C-bead, as extracted from the mixed sample data, exhibits a comparable value to that obtained when measuring only C-bead flowing. However, the fluorescence lifetime of the YG-bead in the mixed sample displays a significantly longer duration. The longer lifetime observed in YG-beads can be attributed to the relatively weaker fluorescence intensity emitted by the bead mixture. This weaker fluorescence intensity makes the YG-bead likely to be influenced by the signal from the C-bead when both types of beads are simultaneously present within the same FOV. Furthermore, the wide-field microscope configuration is used

allowing the excitation of C-beads outside the FOV, which enables the fluorescence signal to reach the objective lens through the internal reflection process within the flowcell. To improve the accuracy of the measured lifetime for the weak intensity sample, further investigation can be performed by improving the optics to increase local intensity and reduce laser spot size.

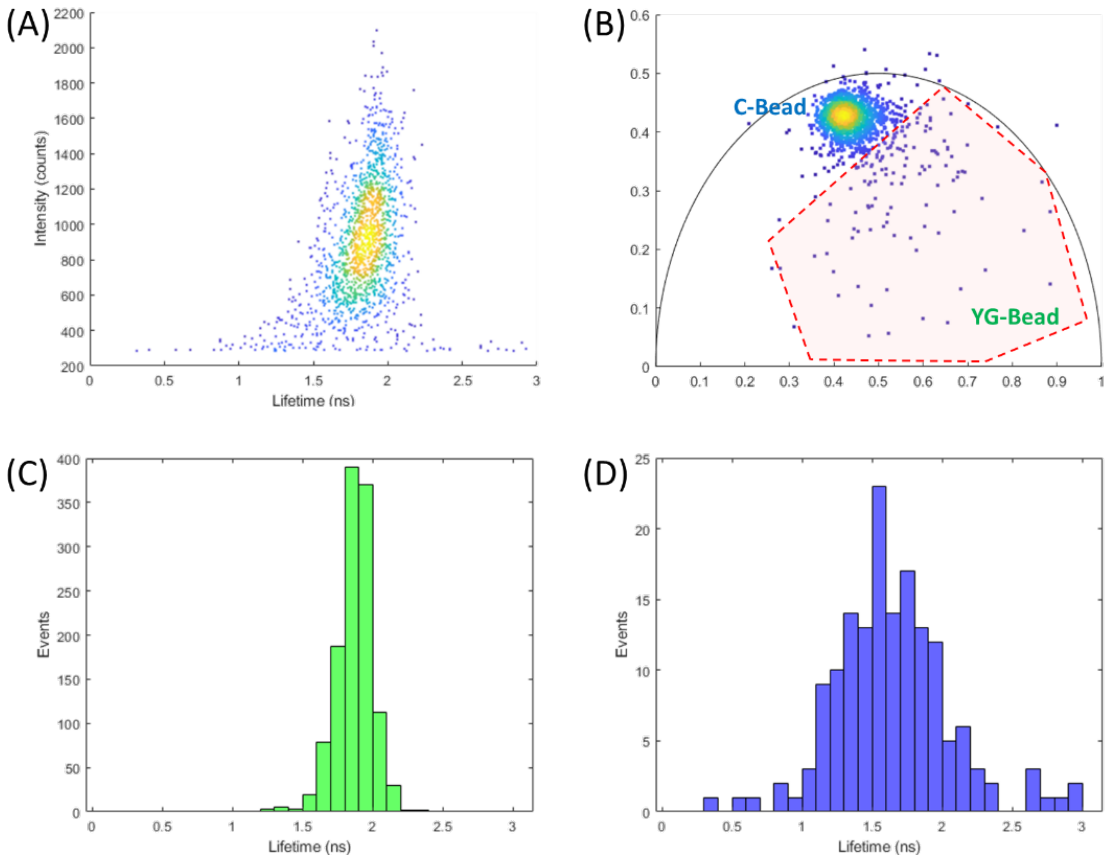

Figure 6.15 Experimental results of flowing mixed fluorescent bead, (A) Scatter plot between fluorescence intensity and lifetime, (B) Phasor plot where the YG bead plots appearing in the red area, (C) and (D) are fluorescence lifetime distribution of gated C- and YG- beads, respectively.

6.4.4 Flowing cell lines

The flow cytometry measurements were performed on the developed system equipped with a 640 nm Deltadiode laser driven at 10 MHz repetition rate. A dichroic mirror reflects the excitation laser to the sample, while the fluorescence signal is collected through the 20x objective (N.A. = 0.4) lens and 665 nm long pass emission filter. Before every measurement, the optical system is aligned by using C-bead to ensure that the flow channel is in the focal plane as indicated by clear TCSPC images of flowing C-bead (Figure 6.7). The incubated cell

lines are injected into the flowcell with a flow rate of 10 µl/min, while the PBS, which is used as sheath fluid, is driven at 62.6 µl/min. The data collection and real-time analysis were performed using the developed software to collect 200,000 events for each cell condition before gating the target cell population. The gating process has been performed separately using custom MATLAB code by using the intensity threshold and position of the phasor plot to extract the nanoprobe data. The intensity threshold is defined by the fluorescence intensity, while the phasor plot position is selected according to the position from the FLIM measurement described by Figure 3.12(G and H) in Chapter 3 and Figure 6.12(C), which represents the nanoprobe conjugating with the RNA.

6.4.4.1 Sample preparation

In this experiment, the objective was to detect the expression of target RNA in both healthy (HEK293) and cancer cells (PC3) in the solution phase. HEK293 and PC3 cell lines are cultured in cell media prepared from DMEM added with 10% FBS, 1% non-essential amino acid, 1% sodium pyruvate and 1% penicillin. The cell lines are de-attached using 500 µl of trypsin and seeded in a 6-well plate with a number of 250,000 cells per well, which was determined using a hemocytometer. The well plate with cell line is kept in a 37° incubator with 5% CO_2 overnight. Once the cell lines are settled, 0.4 nM RNA nanoprobe is added to each well for 4 hours. After incubation, the cells are washed with PBS, de-attached with 100 µl trypsin, and centrifuged at 1200 rpm for 5 minutes. The cells are re-suspended in 1 ml PBS buffer and loaded in a 1 ml syringe (Turemo) for the syringe pump of the FCM. All chemicals used in cell work are purchased from Merck. For the control sample, the cell lines are prepared through the same process without the RNA nano probe incubation.

6.4.4.2 Experimental result

For measurement configuration, the exposure time was set to 3ms to collect enough photons. To accurately measure control samples, it is essential to consider the phenomenon of autofluorescence from the cell. Typically, the excitation laser wavelength used for measurements is located far away from the chemical compounds responsible for autofluorescence, which fall within a specific spectral range [129]. This range is referred to as the spectroscopic window of human skin and is characterised by the low fluorescent intensity of control samples. Hek293 and PC3 control cells show average fluorescence intensity of 273.00 ± 18.31, and 263.53 ± 20.15 counts, respectively. This intensity range overlaps with the background signal measured from water and PBS and is hard to differentiate between the control samples and the background. Therefore, counting control cell lines is not possible. After the control sample measurement, the flow cell was cleaned using a flow

stream of PBS for 30 minutes to make sure there are no clogged cells in the microfluidics channel. The incubated cell lines are injected into the flow cell separately with PBS as the sheath fluid.

Figure 6.16(B and D) are the fluorescence lifetime distribution after extraction. Two gating conditions consisting of intensity threshold and phasor plot position are used for extracting the signal from the nanoprobe. To extract the positive cell, the lower intensity threshold is set to 285 counts to remove the background and cells without nanoprobes or with nanoprobes unopened due to low level of target RNA, which generally has only autofluorescence, while the phasor position is set according to the phasor for open RNA nanoprobe measured earlier as shown in the red area in Figure 6.16(A and C). The dense phasor plot at the top-left area is ignored as they originated from clusters of free hpDNA-Cy5 that remained from the nanoprobe synthesis process (These can be excluded by scattering gating). The measurement was performed for 200,000 continuous frames and 113 and 53 cells were counted for Hek293 and PC3 cell lines respectively. However, the number of cells is lower than expected due to the autofluorescence intensity from the cell being close to the background which is neglected, and not every cell uptake the nanoprobe or nanoprobe opened. Nevertheless, the platform can detect the longer fluorescence lifetime from the nanoprobe in PC3 with a value of 1.34 ± 0.34 ns, compared to HEK293 which is 1.14 ± 0.26 ns. This lifetime difference is also consistent with the lifetime observed in FLIM measurement where PC3 and Hek293 show a lifetime of 1.14 ± 0.43 ns and 0.90 ± 0.02 ns (Table 3), respectively.

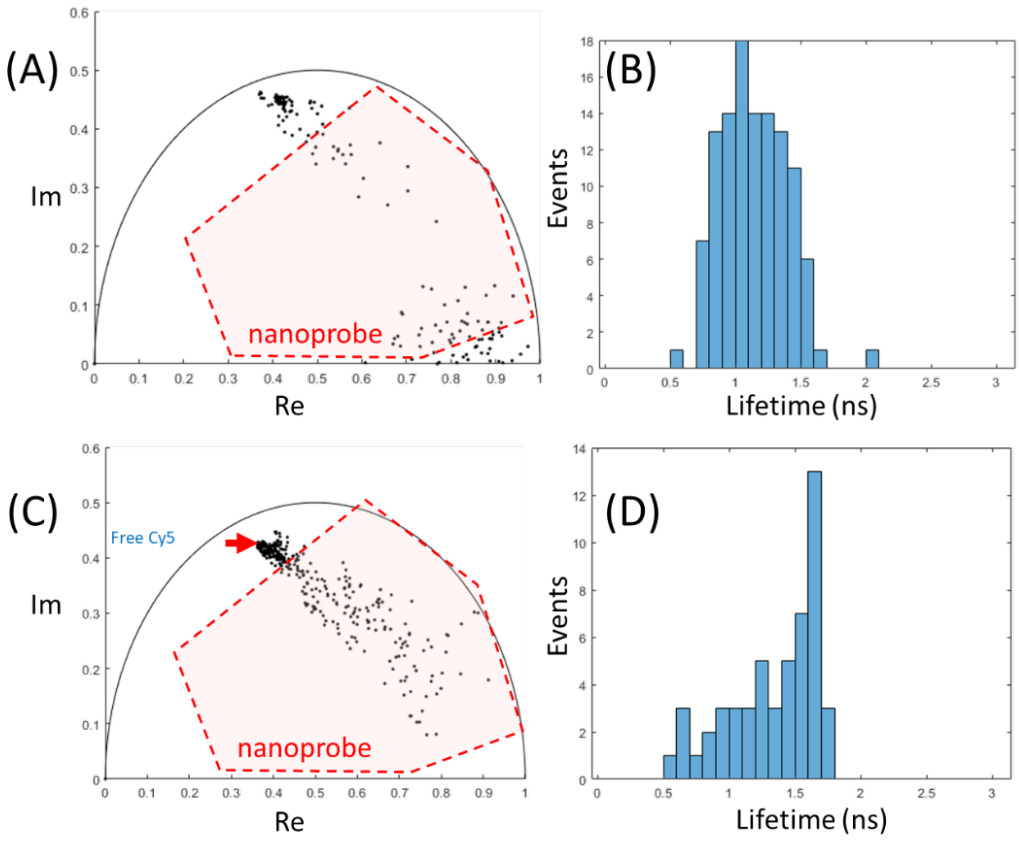

Figure 6.16 Phasor plot of flowing (A) Hek293 and (C) PC3 cell lines incubated with the RNA nanoprobe, while (B) and (D) are the fluorescence lifetime distribution.

6.5 Conclusion

We have developed and investigated the performance of the new prototype of a time-resolved fluorescence flow cytometer platform and its application for cancer cell analysis. The platform composes of four main parts: fluidics, optics, electronics and computer. The fluidics system consists of a syringe and peristaltic pumps, which are used to deliver the sample and focus the sample into a small stream at the centre of the flow cell. The optical system is based on a wide-field microscope equipped with a pulsed laser. The fluorescence signal is collected through a long-pass filter to eliminate the laser. For the electronics system in our work, the SPAD camera is configured to the Megapixel to maximise the photon bandwidth for the FCM application. For computers, we have developed software based on MATLAB to control the platform, rapidly analyse the data and display the data in real-time. The current version of the software can perform a maximum detection rate of 1147 fps on a typical office PC, while 309 fps is the optimal speed with the least miscounted particle possibility. The data can be temporarily stored on RAM for up to 30,000 frames. There is a limitation in that the sensor readout is in a 16-bit format that needs multiple processes of encoding and decoding before

the calculation, which requires a powerful CPU. Implementing the platform into FPGA will take less data communication and greatly improves the overall performance.

The performance of the system is evaluated by using flowing C- and YG- fluorescent microspheres as substitutes for positive and negative cell lines, respectively. Subsequently, we progressed to investigating the system's performance with real cell lines that were incubated with the nanoprobe, aiming to detect and analyse cancer cells in a more biologically relevant detection. The developed prototype of our platform has the capability to detect the fluorescence lifetime of flowing C- and YG-beads. When the beads are flowing separately, the measured fluorescence lifetimes for C-beads and YG-beads are 1.89 ± 0.10 ns and 1.49 ± 0.66 ns, respectively. However, when both types of beads are flowing together, the measured fluorescence lifetimes for C-beads and YG-beads are 1.87 ± 0.13 ns and 1.64 ± 0.43 ns, respectively, where the data are extracted by using a phasor gate and intensity threshold. Furthermore, the system shows the measured fluorescence lifetime of flowing cell lines incubated with nanoprobe of 1.34 ± 0.34 ns and 1.14 ± 0.26 ns for PC3 and Hek293, respectively. This indicates that our platforms can detect the fluorescence lifetime difference from the nanoprobe inside the cancer and non-cancer cells.

Chapter 7 Conclusion and future work

To conclude, our research efforts have yielded significant results in the successful development of a compact flow cytometry platform, incorporating a wide-field microscope setup equipped with a SPAD camera. This promising platform stands as proof of the collaborative efforts from multiple disciplines, seamlessly integrating various fields of science and engineering. The fusion of fluidics, optics, electronics, chemical synthesis, cell culture techniques, and programming has pushed this project forward, introducing the fluorescence lifetime into cytometric analysis. Our platform can be applied across a range of experimental settings, including clinical laboratories and research institutions. This transformative technology has the potential to revolutionise diagnostics, drug discovery, and personalised medicine, enabling rapid and accurate analysis of cell populations with enhanced sensitivity and specificity.

The development of FLACS is outlined in Chapters 3-6. Chapter 3 shows the development of a FLIM analysis platform and its application for analysing FLIM data of cancer and non-cancer cell lines incubated with the RNA nanoprobe. To achieve this, the GUI tool in MATLAB is combined with fit-free analytical methods, such as the CMM, phasor plot, scatter plot, and distribution plot, to effectively analyse and visualise data obtained from the LSM510 system (Zeiss) equipped with the SPC-830 TCSPC module (Becker & Hickl GmbH). This analysis platform can successfully differentiate between cancer and non-cancer cells based on their respective fluorescence lifetime images and phasor plots. This integration of promising analytical methodologies and speedy performance helps cancer research. Moreover, this FLIM analysis platform can be used for routine FLIM data for cell imaging and FRET study,

Chapter 4 provides comprehensive details about the characterisation and calibration of a SPAD camera. The Megapixel integration method has been developed to enhance the photon bandwidth by combining all pixels into one pixel that can detect 24,576 photons at once. Due to the non-identical electrical and physical properties of every single pixel, the megapixel has been characterised using software by adding and removing time delay and applying the bad pixel mask, leaving the usable area of 78.91% of the total sensor area. As SPADs at room temperature typically present higher dark counts compared to cooled SPADs, a background reduction process is performed prior to analysis. This involves applying a Savitzky-Golay filter and background subtraction, with the background value calculated from the average

photon counts of the time-resolved data before the decay peak. Finally, a comparison is conducted between non-calibrated and calibrated sensors using fluorescein, a reference dye with a mono-exponential decay model and a lifetime of 4 ns. The comparison demonstrates that the calibrated sensor yields more accurate lifetime measurements and a narrower lifetime distribution.

Chapter 5 outlines the comprehensive development and characterisation of the fluidic system. Specifically, for FCM applications, the fluidic system plays an important role in assisting the introduction of the suspended sample into the flow cell where laser illumination occurs. To achieve optimal single particle measurement, the sample stream is hydrodynamically focused into a narrower stream by adjusting the flow rate ratio of sheath fluid to the sample. The sheath fluids commonly include distilled water or PBS. In this study, two distinct designs of the flow cell based on a flow-through quartz cuvette and a microfluidic channel slide have been presented and compared. Currently, the flow rate of both pumps is fixed at 10 µl/min, and 62.6 µl/min, respectively, to create the focused flow in the flowcell and the sample stream can be narrowed down to the diameter of 45 µm.

The development from Chapter 3 to Chapter 5 is assembled into the prototype of the FLACS platform that is described in Chapter 6. A GUI software has been developed using MATLAB that controls the SPAD camera and allows users to adjust measurement configurations including exposure time, intensity threshold, ROI and measurement modes. The current version of the software is capable of achieving speeds of up to 1147 fps on a typical office PC with the storage of temporal data for up to 30,000 frames on RAM. The fluidic system is configured and tested with a sample density of 1.8×10^5 particles/ml. The fluorescence signal from the hydrodynamically focused sample is collected through the optical system to the SPAD camera that is configured as a Megapixel. The prototype has been tested with C- and YG- beads, which represents positive and negative sample respectively. Then, cancer and non-cancer cell lines incubated with the RNA nanoprobe are successfully detected by the prototype indicated by showing the different phasor position and fluorescence lifetime of 1.34 ± 0.34 ns and 1.14 ± 0.26 ns for PC3 and Hek293, respectively. This demonstrates that this platform can detect the fluorescence lifetime difference between the nanoprobes inside cancer and non-cancer cells. This prototype can be applied to routine biological research such as cell screening and rare cell population detection, potentially an alternative tool for early-stage cancer diagnosis.

Lastly, notable contributions to the FLACS platform encompass the following key points: (1) we have implemented pixel integration, referred to as "megapixel," on the SPAD camera.

This developed technique significantly improves the bandwidth for single photon counting. The megapixel undergoes several characterisation processes, including response time alignment, bad pixel masking, noise filtering, and background subtraction, to enhance its accuracy and reliability. (2) Our work includes the design of a flow cell and the optical setup required for flow cytometry, which is based on a wide-field microscope. The flow cell configuration ensures precise and controlled sample handling, facilitating efficient analysis of the flowing particles. (3) We have developed an FCM platform for cancer cell screening by using the RNA nanoprobe. We showcase the capability to differentiate fluorescence lifetime differences between flowing cancer and non-cancer cells. This demonstrates the potential of our platform in providing valuable insights into cellular characteristics and advancing cancer cell analysis. (4) We introduce the time-domain fluorescence lifetime measurement for flowing particles by combining the megapixel integration with fast and fit-free CMM and phasor method to enable real-time fluorescence lifetime estimation as the particle passes through the FOV. All FCM parameters are displayed graphically in the developed software based on MATLAB. This approach allows for the extraction of more comprehensive fluorescence dynamics, leading to an intense characterisation of the samples under investigation.

7.1 Current development

In addition to the current measurement techniques including fluorescence intensity and lifetime measurements, which have been successfully implemented into the platform, there is a plan to improve the platform with additional analysing parameters such as forward scattering intensity and sorting capabilities. These improvements aim to broaden the platform's utility and transform it into a versatile benchtop flow cytometer. By incorporating forward scattering intensity as a parameter for analysis, the platform can provide valuable insights into cell or particle size and can be used to distinguish dead or alive cells, accompanied by the existing fluorescence-based measurements.

The forward scattering signal, characterised by the scattered light at a small angle (< 5°) to the excitation line with the same wavelength, is commonly used as an indicator of cell or particle size and for sample counting. The forward scattering system, depicted in Figure 7.1, includes Arduino and Matlab which operates independently. Currently, the Arduino is used to continuously read the light intensity detected by the BH1750 light sensor module and reports it over the serial port, while Matlab listens to the serial port for data receiving. However, the current implementation of the system shows a significant decrease in measurement speed, where a single measurement of 3 ms exposure time can become 40 ms with scattering

detection compared to 4.5 ms without scattering detection. Hence, there is a need for code optimisation and hardware upgrades to improve the speed of forward scattering detection, for example, using USB3.0 to reduce the connectivity lags and change the microcontroller chip to achieve higher clock speed.

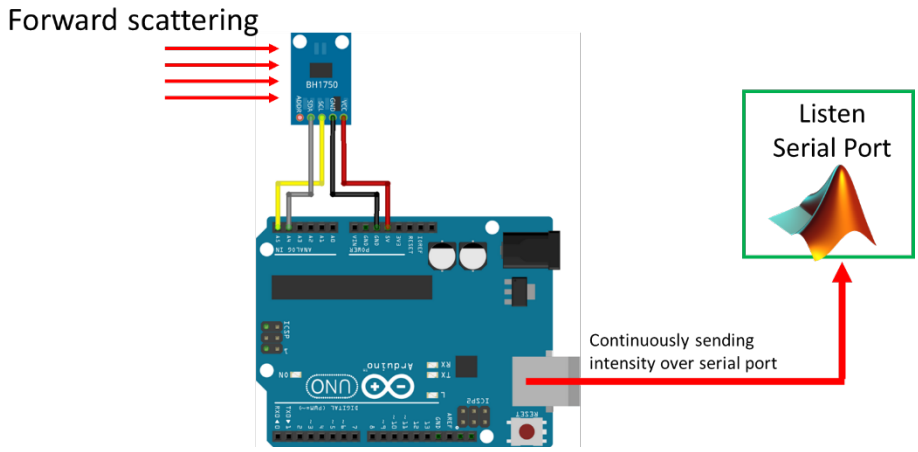

Figure 7.1 Schematic diagram of the forward scattering detection system including lux sensor (BH1750) and Arduino Uno, which is connected to the software through the serial port.

Furthermore, the inclusion of sorting capabilities will enable the platform to perform efficient and targeted separation of specific cell populations based on various parameters, enhancing its functionality as a complete tool for flow cytometric analysis and cell sorting. The cell sorting process is important in various fields of biological and medical research as it allows researchers to isolate and separate specific cell populations based on their characteristics using FCM parameters. This process can enrich a specific cell population, extract rare cells such as stem cell and circulating tumour, or other investigation that requires cell isolation for detailed analysis. The proposed design for future cell sorting is presented in Figure 7.2. The sorting system is an additional component integrated into the existing setup, comprising a piezoelectric pump equipped with a pump driver chip (BT-mp6-liq, Bartels), and a Raspberry Pi 4 used for pump control. Upon the passage of cells or particles through the FOV, the fluorescence lifetime data captured by the SPAD camera is transmitted to the developed software for analysis and gating based on user-defined parameters, including fluorescence intensity, lifetime, or phasor position. If the sample satisfies the gating criteria, the software triggers the Raspberry Pi, applying the diagonal water pressure for a short duration, driving the particle/cell to the output channel. The time interval that particle flows from FOV to the sorting area can be calculated based on the particle velocity and flow cell dimension. At present, the sorting capability is under development. Once implemented, this advanced

platform will serve as a versatile tool for various biological research applications, expanding the scope and functionality of the current system.

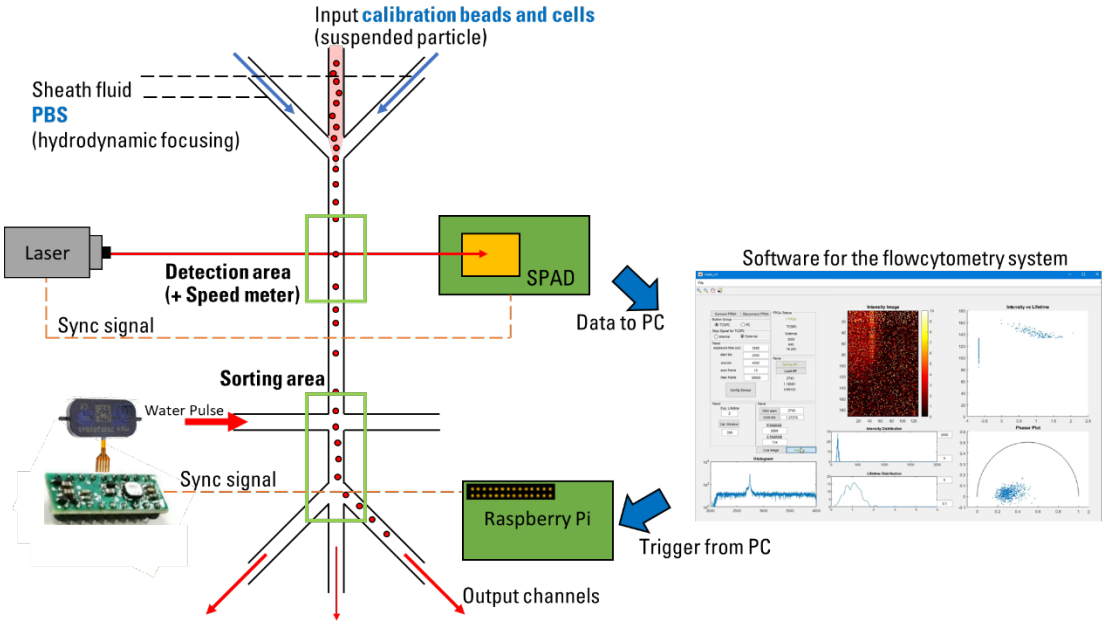

Figure 7.2 Schematic design for cell sorting

7.2 Further work

The current development of the platform reveals several gaps that need further attention. Firstly, it has been observed that the SPAD camera exhibits poor noise performance when operating at room temperature [100]. To address this limitation, the inclusion of additional cooling measures such as heatsinks, cooling fans, and a cooling liquid system becomes essential. These cooling mechanisms would effectively reduce temperature-related noise, offering potential benefits for future advancements, such as super-resolution imaging research.

Secondly, for the platform to achieve a broader range of applications, further testing with different types of cell lines and mRNA nanoprobe is required. Currently, the photophysics group at the University of Strathclyde has developed several nanoprobes to target cancer biomarker RNAs, including c-Myc, Sox2, and linc0026. To enable more specific cancer type screening, it is important to explore the performance of the detection with different cancer types. Additionally, investigating mixed cell lines containing both cancerous and non-cancerous cells, and incubating them with the mRNA nanoprobes, will facilitate a more comprehensive evaluation of the platform's capabilities.

Lastly, the current prototype employs the CMM method, which requires a minimum of 200 photon counts to perform accurate lifetime estimation. While this photon count is sufficient for positive cell lines, it shows challenges when dealing with negative cell samples or cells with low levels of target RNA which have weak fluorescence intensity. To overcome this limitation, the future development of the platform will incorporate deep learning techniques. Dong et al. have demonstrated the effectiveness of this approach in calculating fluorescence lifetimes from FCM data [58] and this is possible to implement in our real-time data analysis. Moreover, the deep learning techniques will enable the extraction of meaningful signals from the sea of background noise. The usage of microlens can also improve the SNR allowing the platform to have better photon collection efficiency [130].

Further improvements and exploration in the areas discussed above will enhance the performance of the platform, expand its applications, and refine its capabilities for more advanced research applications in future.

References

[1] J. P. Houston, Z. Yang, J. Sambrano, W. Li, K. Nichani, and G. Vacca, "Overview of Fluorescence Lifetime Measurements in Flow Cytometry," in *Flow Cytometry Protocols*, T. S. Hawley and R. G. Hawley, Eds., New York, NY: Springer New York, 2018, pp. 421–446. doi: 10.1007/978-1-4939-7346-0_18.

[2] D. J. S. Birch, Y. Chen, and O. J. Rolinski, "Fluorescence," in *Photonics*, 2015, pp. 1–58. doi: https://doi.org/10.1002/9781119011804.ch1.

[3] J. R. Lakowicz, *Principles of fluorescence spectroscopy*, 3rd ed. New York: Springer US, 2006.

[4] N. Boens *et al.*, "Fluorescence lifetime standards for time and frequency domain fluorescence spectroscopy," *Anal Chem*, vol. 79, no. 5, pp. 2137–2149, Mar. 2007, doi: 10.1021/ac062160k.

[5] L. D. Lavis and R. T. Raines, "Bright ideas for chemical biology," *ACS Chemical Biology*, vol. 3, no. 3. pp. 142–155, Mar. 20, 2008. doi: 10.1021/cb700248m.

[6] J. Surre, C. Saint-Ruf, V. Collin, S. Orenga, M. Ramjeet, and I. Matic, "Strong increase in the autofluorescence of cells signals struggle for survival," *Sci Rep*, vol. 8, no. 1, Dec. 2018, doi: 10.1038/s41598-018-30623-2.

[7] K. Ray and J. R. Lakowicz, "Metal-enhanced fluorescence lifetime imaging and spectroscopy on a modified SERS substrate," *Journal of Physical Chemistry C*, vol. 117, no. 30, pp. 15790–15797, Aug. 2013, doi: 10.1021/jp404590j.

[8] D. Magde, G. E. Rojas, and P. G. Seybold, "Solvent dependence of the fluorescence lifetimes of xanthene dyes," *Photochem Photobiol*, vol. 70, no. 5, pp. 737–744, 1999, doi: 10.1111/j.1751-1097.1999.tb08277.x.

[9] J. R. Lakowicz and G. Weber, "Quenching of fluorescence by oxygen. Probe for structural fluctuations in macromolecules," *Biochemistry*, vol. 12, no. 21, pp. 4161–4170, Oct. 1973, doi: 10.1021/bi00745a020.

[10] C. S. Yun *et al.*, "Nanometal surface energy transfer in optical rulers, breaking the FRET barrier," *J Am Chem Soc*, vol. 127, no. 9, pp. 3115–3119, Mar. 2005, doi: 10.1021/ja043940i.

[11] C. Chen, C. Midelet, S. Bhuckory, N. Hildebrandt, and M. H. V. Werts, “Nanosurface Energy Transfer from Long-Lifetime Terbium Donors to Gold Nanoparticles,” *Journal of Physical Chemistry C*, vol. 122, no. 30, pp. 17566–17574, Aug. 2018, doi: 10.1021/acs.jpcc.8b06539.

[12] X. Huang and M. A. El-Sayed, “Gold nanoparticles: Optical properties and implementations in cancer diagnosis and photothermal therapy,” *Journal of Advanced Research*, vol. 1, no. 1. pp. 13–28, Jan. 2010. doi: 10.1016/j.jare.2010.02.002.

[13] O. R. Odaudu and A. A. Akinsiku, “Toxicity and Cytotoxicity Effects of Selected Nanoparticles: A Review,” in *IOP Conference Series: Earth and Environmental Science*, Institute of Physics, Sep. 2022. doi: 10.1088/1755-1315/1054/1/012007.

[14] C. Racknor, M. R. Singh, Y. Zhang, D. J. S. Birch, and Y. Chen, “Energy transfer between a biological labelling dye and gold nanorods,” *Methods Appl Fluoresc*, vol. 2, no. 1, p. 015002, Nov. 2013, doi: 10.1088/2050-6120/2/1/015002.

[15] E. Dulkeith *et al.*, “Fluorescence Quenching of Dye Molecules near Gold Nanoparticles: Radiative and Nonradiative Effects,” *Phys Rev Lett*, vol. 89, no. 20, 2002, doi: 10.1103/PhysRevLett.89.203002.

[16] Y. Zhang, G. Wei, J. Yu, D. J. S. Birch, and Y. Chen, “Surface plasmon enhanced energy transfer between gold nanorods and fluorophores: Application to endocytosis study and RNA detection,” *Faraday Discuss*, vol. 178, pp. 383–394, Jun. 2015, doi: 10.1039/c4fd00199k.

[17] G. Wei, J. Yu, J. Wang, P. Gu, D. J. S. Birch, and Y. Chen, “Hairpin DNA-functionalized gold nanorods for mRNA detection in homogenous solution,” *J Biomed Opt*, vol. 21, no. 9, p. 097001, Sep. 2016, doi: 10.1117/1.jbo.21.9.097001.

[18] Z. S. Mbalaha, P. R. Edwards, D. J. S. Birch, and Y. Chen, “Synthesis of Small Gold Nanorods and Their Subsequent Functionalization with Hairpin Single Stranded DNA,” *ACS Omega*, vol. 4, no. 9, pp. 13740–13746, Aug. 2019, doi: 10.1021/acsomega.9b01200.

[19] J. P. Houston, Z. Yang, J. Sambrano, W. Li, K. Nichani, and G. Vacca, “Overview of fluorescence lifetime measurements in flow cytometry,” in *Methods in Molecular Biology*, vol. 1678, Humana Press Inc., 2018, pp. 421–446. doi: 10.1007/978-1-4939-7346-0_18.

[20] L. Bene and L. Damjanovich, “The other side of the coin: Time-domain fluorescence lifetime in flow,” *Cytometry Part A*, vol. 87, no. 2, pp. 101–103, Feb. 2015, doi: 10.1002/cyto.a.22615.

[21] X. Liu *et al.*, “Fast fluorescence lifetime imaging techniques: A review on challenge and development,” *J Innov Opt Health Sci*, vol. 12, no. 5, Sep. 2019, doi: 10.1142/S1793545819300039.

[22] H. M. Shapiro, *How Flow Cytometers Work*, 3rd ed. 2003. doi: https://doi.org/10.1002/0471722731.

[23] J. Vives-Rego, P. Lebaron, and G. Nebe-von Caron, “Current and future applications of flow cytometry in aquatic microbiology,” *FEMS Microbiol Rev*, vol. 24, no. 4, pp. 429–448, Oct. 2000, doi: 10.1111/j.1574-6976.2000.tb00549.x.

[24] M. Brown and C. Wittwer, “Flow Cytometry: Principles and Clinical Applications in Hematology,” *Clin Chem*, vol. 46, no. 8, pp. 1221–1229, 2000, doi: 10.1093/clinchem/46.8.1221.

[25] M. J. Crow, S. M. Marinakos, J. M. Cook, A. Chilkoti, and A. Wax, “Plasmonic flow cytometry by immunolabeled nanorods,” *Cytometry Part A*, vol. 79 A, no. 1, pp. 57–65, Jan. 2011, doi: 10.1002/cyto.a.20994.

[26] J. A. Steinkamp, T. M. Yoshida, and J. C. Martin, “Flow cytometer for resolving signals from heterogeneous fluorescence emissions and quantifying lifetime in fluorochrome-labeled cells/particles by phase-sensitive detection,” *Review of Scientific Instruments*, vol. 64, no. 12, pp. 3440–3450, 1993, doi: 10.1063/1.1144265.

[27] ThermoFisher Scientific, “FCS Express™ Flow Cytometry Analysis Software.” Accessed: Jan. 25, 2023. [Online]. Available: https://www.thermofisher.com/order/catalog/product/A48515

[28] M. J. Crow, S. M. Marinakos, J. M. Cook, A. Chilkoti, and A. Wax, “Plasmonic flow cytometry by immunolabeled nanorods,” *Cytometry Part A*, vol. 79 A, no. 1, pp. 57–65, Jan. 2011, doi: 10.1002/cyto.a.20994.

[29] G. D. Craig, “Fluorescent Gold Nanorod Probes for the Detection of Cancer mRNA Biomarkers,” Doctoral thesis, University of Strathclyde, Glasgow, 2020. doi: 10.48730/30g0-wy45.

[30] D. Kage, K. Hoffmann, M. Wittkamp, J. Ameskamp, W. Göhde, and U. Resch-Genger, “Luminescence lifetime encoding in time-domain flow cytometry,” *Sci Rep*, vol. 8, no. 1, Dec. 2018, doi: 10.1038/s41598-018-35137-5.

[31] B. G. Pinsky, J. J. Ladasky, J. R. Lakowicz, K. Berndt, and R. A. Hoffman, “Phase-resolved fluorescence lifetime measurements for flow cytometry,” *Cytometry*, vol. 14, no. 2, pp. 123–135, 1993, doi: 10.1002/cyto.990140204.

[32] J. A. Steinkamp, T. M. Yoshida, and J. C. Martin, “Flow cytometer for resolving signals from heterogeneous fluorescence emissions and quantifying lifetime in fluorochrome-labeled cells/particles by phase-sensitive detection,” *Review of Scientific Instruments*, vol. 64, no. 12, pp. 3440–3450, 1993, doi: 10.1063/1.1144265.

[33] C. Deka, L. A. Sklar, and J. A. Steinkamp, “Fluorescence lifetime measurements in a flow cytometer by amplitude demodulation using digital data acquisition technique,” *Cytometry*, vol. 17, no. 1, pp. 94–101, 1994, doi: 10.1002/cyto.990170112.

[34] P. Jenkins, M. A. Naivar, and J. P. Houston, “Toward the measurement of multiple fluorescence lifetimes in flow cytometry: Maximizing multi-harmonic content from cells and microspheres,” *J Biophotonics*, vol. 8, no. 11–12, pp. 908–917, Nov. 2015, doi: 10.1002/jbio.201400115.

[35] D. Kage, K. Hoffmann, H. Borcherding, U. Schedler, and U. Resch-Genger, “Lifetime encoding in flow cytometry for bead-based sensing of biomolecular interaction,” *Sci Rep*, vol. 10, no. 1, Dec. 2020, doi: 10.1038/s41598-020-76150-x.

[36] F. Alturkistany, K. Nichani, K. D. Houston, and J. P. Houston, “Fluorescence lifetime shifts of NAD(P)H during apoptosis measured by time-resolved flow cytometry,” *Cytometry Part A*, vol. 95, no. 1, pp. 70–79, Jan. 2019, doi: 10.1002/cyto.a.23606.

[37] W. Li, K. D. Houston, and J. P. Houston, “Shifts in the fluorescence lifetime of EGFP during bacterial phagocytosis measured by phase-sensitive flow cytometry,” *Sci Rep*, vol. 7, Jan. 2017, doi: 10.1038/srep40341.

[38] J. Nedbal *et al.*, “Time-domain microfluidic fluorescence lifetime flow cytometry for high-throughput Förster resonance energy transfer screening,” *Cytometry Part A*, vol. 87, no. 2, pp. 104–118, Feb. 2015, doi: 10.1002/cyto.a.22616.

[39] D. Kage *et al.*, “Tempo-spectral multiplexing in flow cytometry with lifetime detection using QD-encoded polymer beads,” *Sci Rep*, vol. 10, no. 1, Dec. 2020, doi: 10.1038/s41598-019-56938-2.

[40] R. Cao *et al.*, “Phasor plotting with frequency-domain flow cytometry,” *Opt Express*, vol. 24, no. 13, p. 14596, Jun. 2016, doi: 10.1364/oe.24.014596.

[41] F. M. Della Rocca *et al.*, “Real-time fluorescence lifetime actuation for cell sorting using a CMOS SPAD silicon photomultiplier,” *Opt Lett*, vol. 41, no. 4, pp. 673–676, 2016, doi: 10.1364/OL.41.000673.

[42] Kinetic River, “Introducing the Danube.” Accessed: Dec. 05, 2022. [Online]. Available: https://www.kineticriver.com/danube/

[43] Kinetic River, “Introducing the Danube II,” 2014, Accessed: Dec. 05, 2022. [Online]. Available: https://www.kineticriver.com/introducing-the-danube-ii/

[44] W. He *et al.*, “Quantitation of circulating tumor cells in blood samples from ovarian and prostate cancer patients using tumor-specific fluorescent ligands,” *Int J Cancer*, vol. 123, no. 8, pp. 1968–1973, Oct. 2008, doi: 10.1002/ijc.23717.

[45] B. Korzh *et al.*, “Demonstration of sub-3 ps temporal resolution with a superconducting nanowire single-photon detector,” *Nat Photonics*, vol. 14, no. 4, pp. 250–255, Apr. 2020, doi: 10.1038/s41566-020-0589-x.

[46] C. Zhang, S. Lindner, I. M. Antolovic, J. Mata Pavia, M. Wolf, and E. Charbon, “A 30-frames/s, 252 × 144 SPAD Flash LiDAR with 1728 Dual-Clock 48.8-ps TDCs, and Pixel-Wise Integrated Histogramming,” *IEEE J Solid-State Circuits*, vol. 54, no. 4, pp. 1137–1151, Apr. 2019, doi: 10.1109/JSSC.2018.2883720.

[47] R. K. Henderson *et al.*, “A 192x128 Time Correlated SPAD Image Sensor in 40-nm CMOS Technology,” *IEEE J Solid-State Circuits*, vol. 54, pp. 1907–1916, 2019, doi: 10.1109/JSSC.2019.2905163.

[48] I. Isenberg and R. D. Dyson, “The Analysis of Fluorescence Decay by a Method of Moments,” *Biophys J*, vol. 9, no. 11, pp. 1337–1350, 1969, doi: https://doi.org/10.1016/S0006-3495(69)86456-8.

[49] M. A. Digman, V. R. Caiolfa, M. Zamai, and E. Gratton, “The phasor approach to fluorescence lifetime imaging analysis,” *Biophys J*, vol. 94, no. 2, Jan. 2008, doi: 10.1529/biophysj.107.120154.

[50] Y. Li *et al.*, “Lifetime Determination Algorithms for Time-Domain Fluorescence Lifetime Imaging: A Review,” in *Fluorescence Imaging - Recent Advances and Applications [Working Title]*, IntechOpen, 2022. doi: 10.5772/intechopen.106423.

[51] Y. Li *et al.*, “Investigations on Average Fluorescence Lifetimes for Visualizing Multi-Exponential Decays,” *Front Phys*, vol. 8, Oct. 2020, doi: 10.3389/fphy.2020.576862.

[52] N. Sapermsap *et al.*, “A rapid analysis platform for investigating the cellular locations of bacteria using two-photon fluorescence lifetime imaging microscopy,” *Methods Appl Fluoresc*, vol. 8, no. 3, Jul. 2020, doi: 10.1088/2050-6120/ab854e.

[53] D.-U. Li, B. R. Rae, R. Andrews, J. Arlt, and R. K. Henderson, “Hardware implementation algorithm and error analysis of high-speed fluorescence lifetime sensing systems using center-of-mass method,” *J Biomed Opt*, vol. 15, no. 1, p. 017006, Jan. 2010, doi: 10.1117/1.3309737.

[54] D. D.-U. Li *et al.*, “Video-rate fluorescence lifetime imaging camera with CMOS single-photon avalanche diode arrays and high-speed imaging algorithm,” *J Biomed Opt*, vol. 16, no. 9, p. 096012, 2011, doi: 10.1117/1.3625288.

[55] S. P. Poland *et al.*, “New high-speed centre of mass method incorporating background subtraction for accurate determination of fluorescence lifetime,” *Opt Express*, vol. 24, no. 7, p. 6899, Apr. 2016, doi: 10.1364/oe.24.006899.

[56] D. U. Li *et al.*, “Video-rate fluorescence lifetime imaging camera with CMOS single-photon avalanche diode arrays and high-speed imaging algorithm,” *J Biomed Opt*, vol. 16, no. 9, pp. 1–13, Sep. 2011.

[57] D. M. Miller, S. D. Thomas, A. Islam, D. Muench, and K. Sedoris, “c-Myc and cancer metabolism,” *Clinical Cancer Research*, vol. 18, no. 20. pp. 5546–5553, Oct. 15, 2012. doi: 10.1158/1078-0432.CCR-12-0977.

[58] D. Xiao *et al.*, “Dynamic fluorescence lifetime sensing with CMOS single-photon avalanche diode arrays and deep learning processors,” *Biomed Opt Express*, vol. 12, no. 6, p. 3450, Jun. 2021, doi: 10.1364/boe.425663.

[59] W. Becker, *The bh TCSPC handbook*, 9th ed. 2021.

[60] HORIBA Jobin Yvon IBH, *User guide: DAS6 Fluorescence Decay Analysis Software*.

[61] J. R. Lakowicz, *Principles of fluorescence spectroscopy, 3rd Edition, Joseph R. Lakowicz, editor*. New York: Springer, 2006. doi: 10.1007/978-0-387-46312-4.

[62] Philip Yip, “Nanometrology using Time-Resolved Fluorescence Techniques,” Doctoral thesis, University of Strathclyde, Glasgow, 2016. doi: 10.48730/g0d9-1603.

[63] S. Ranjit, L. Malacrida, D. M. Jameson, and E. Gratton, “Fit-free analysis of fluorescence lifetime imaging data using the phasor approach,” *Nat Protoc*, vol. 13, no. 9, pp. 1979–2004, Sep. 2018, doi: 10.1038/s41596-018-0026-5.

[64] D. Li and Y. Chen, “Hardware-friendly bi-exponential fluorescence lifetime imaging algorithms and phasor approaches,” in *Advanced Microscopy Techniques IV; and Neurophotonics II*, Munich: SPIE Proceedings (Optica Publishing Group, 2015), 2015, pp. 141–548. doi: 10.1364/ECBO.2015.95360M.

[65] S.-C. Liao, Y. Sun, and U. Coskun, “FLIM Analysis using the Phasor Plots,” *ISS TECHNICAL NOTE*. 2014.

[66] R. L. Siegel, K. D. Miller, and A. Jemal, “Cancer statistics, 2016,” *CA Cancer J Clin*, vol. 66, no. 1, pp. 7–30, Jan. 2016, doi: 10.3322/caac.21332.

[67] D. Sparanese and C. H. Lee, “CRD-BP shields c-myc and MDR-1 RNA from endonucleolytic attack by a mammalian endoribonuclease,” *Nucleic Acids Res*, vol. 35, no. 4, pp. 1209–1221, Feb. 2007, doi: 10.1093/nar/gkl1148.

[68] Y. Zhang, D. J. S. Birch, and Y. Chen, “Two-photon excited surface plasmon enhanced energy transfer between DAPI and gold nanoparticles: Opportunities in intra-cellular imaging and sensing,” *Appl Phys Lett*, vol. 99, no. 10, Sep. 2011, doi: 10.1063/1.3633066.

[69] S. Link and M. A. El-Sayed, “Spectral Properties and Relaxation Dynamics of Surface Plasmon Electronic Oscillations in Gold and Silver Nanodots and Nanorods,” *Journal of Physical Chemistry B*, vol. 103, no. 40, pp. 8410–8426, Oct. 1999, doi: 10.1021/jp9917648.

[70] S. Farooq, F. Wali, D. M. Zezell, R. E. de Araujo, and D. Rativa, “Optimizing and Quantifying Gold Nanospheres Based on LSPR Label-Free Biosensor for Dengue Diagnosis,” *Polymers (Basel)*, vol. 14, no. 8, Apr. 2022, doi: 10.3390/polym14081592.

[71] C. Wu, X. Zhou, and J. Wei, “Localized Surface Plasmon Resonance of Silver Nanotriangles Synthesized by a Versatile Solution Reaction,” *Nanoscale Res Lett*, vol. 10, no. 1, Dec. 2015, doi: 10.1186/s11671-015-1058-1.

[72] S. L. Smitha, K. G. Gopchandran, N. Smijesh, and R. Philip, “Size-dependent optical properties of Au nanorods,” *Progress in Natural Science: Materials International*, vol. 23, no. 1, pp. 36–43, Feb. 2013, doi: 10.1016/j.pnsc.2013.01.005.

[73] Y. Zhang, J. Yu, D. J. S. Birch, and Y. Chen, “Gold nanorods for fluorescence lifetime imaging in biology,” *J Biomed Opt*, vol. 15, no. 2, p. 020504, 2010, doi: 10.1117/1.3366646.

[74] Y. Zhang, G. Wei, J. Yu, D. J. S. Birch, and Y. Chen, “Surface plasmon enhanced energy transfer between gold nanorods and fluorophores: Application to endocytosis study and RNA detection,” *Faraday Discuss*, vol. 178, pp. 383–394, 2015, doi: 10.1039/c4fd00199k.

[75] Y. Zhang, D. J. S. Birch, and Y. Chen, “Two-photon excited surface plasmon enhanced energy transfer between DAPI and gold nanoparticles: Opportunities in intra-cellular imaging and sensing,” *Appl Phys Lett*, vol. 99, no. 10, p. 103701, Sep. 2011, doi: 10.1063/1.3633066.

[76] M. A. Digman, V. R. Caiolfa, M. Zamai, and E. Gratton, “The phasor approach to fluorescence lifetime imaging analysis,” *Biophys J*, vol. 94, no. 2, pp. 14–16, 2008, doi: 10.1529/biophysj.107.120154.

[77] J. S. Basuki *et al.*, “Using Fluorescence Lifetime Imaging Microscopy to Monitor Theranostic Nanoparticle Uptake and Intracellular Doxorubicin Release,” *ACS Nano*, vol. 7, no. 11, pp. 10175–10189, Nov. 2013, doi: 10.1021/nn404407g.

[78] A. Celli, S. Sanchez, M. Behne, T. Hazlett, E. Gratton, and T. Mauro, “The epidermal Ca(2+) gradient: Measurement using the phasor representation of fluorescent lifetime imaging,” *Biophys J*, vol. 98, no. 5, pp. 911–921, Mar. 2010, doi: 10.1016/j.bpj.2009.10.055.

[79] U. O. Susanne Trautmann, Volker Buschmann, Sandra Orthaus, Felix Koberling and R. Erdmann, “Fluorescence Lifetime Imaging (FLIM) in Confocal Microscopy Applications: An Overview,” *Application Note*, no. PicoQuant GmbH, 2013.

[80] C. Hille, M. Lahn, and C. Dosche, “Two-photon fluorescence lifetime imaging (2P-FLIM) for ion sensing in living cells,” *Application Note*, PicoQuant GmbH, 2008.

[81] D. U. D.-U. Li *et al.*, “Video-rate fluorescence lifetime imaging camera with CMOS single-photon avalanche diode arrays and high-speed imaging algorithm,” *J Biomed Opt*, vol. 16, no. 9, p. 096012, Sep. 2011, doi: 10.1117/1.3625288.

[82] S. P. Poland *et al.*, “New high-speed centre of mass method incorporating background subtraction for accurate determination of fluorescence lifetime,” *Opt Express*, vol. 24, no. 7, pp. 6899–6915, 2016, doi: 10.1364/OE.24.006899.

[83] Q. Wang *et al.*, “Simple and Robust Deep Learning Approach for Fast Fluorescence Lifetime Imaging,” *Sensors*, vol. 22, no. 19, Oct. 2022, doi: 10.3390/s22197293.

[84] W. Becker, “Recording the Instrument Response Function of a Multiphoton FLIM System,” Application Note. Accessed: Aug. 18, 2019. [Online]. Available: https://www.becker-hickl.com/wp-content/uploads/2018/12/irf-mp-v04.pdf

[85] B. Nikoobakht and M. A. El-Sayed, “Preparation and growth mechanism of gold nanorods (NRs) using seed-mediated growth method,” *Chemistry of Materials*, vol. 15, no. 10, pp. 1957–1962, May 2003, doi: 10.1021/cm020732l.

[86] C. J. Johnson, E. Dujardin, S. A. Davis, C. J. Murphy, and S. Mann, “Growth and form of gold nanorods prepared by seed-mediated, surfactant-directed synthesis,” *J Mater Chem*, vol. 12, no. 6, pp. 1765–1770, 2002, doi: 10.1039/b200953f.

[87] D. K. Smith and B. A. Korgel, “The importance of the CTAB surfactant on the colloidal seed-mediated synthesis of gold nanorods,” *Langmuir*, vol. 24, no. 3, pp. 644–649, 2008, doi: 10.1021/la703625a.

[88] D. K. Smith and B. A. Korgel, “The importance of the CTAB surfactant on the colloidal seed-mediated synthesis of gold nanorods,” *Langmuir*, vol. 24, no. 3, pp. 644–649, Feb. 2008, doi: 10.1021/la703625a.

[89] A. Wijaya and K. Hamad-Schifferli, “Ligand customization and DNA functionalization of gold nanorods via round-trip phase transfer ligand exchange,” *Langmuir*, vol. 24, no. 18, pp. 9966–9969, Sep. 2008, doi: 10.1021/la8019205.

[90] J. Lukomska, I. Gryczynski, J. Malicka, S. Makowiec, J. R. Lakowicz, and Z. Gryczynski, “Two-photon induced fluorescence of Cy5-DNA in buffer solution and on silver island films,” *Biochem Biophys Res Commun*, vol. 328, no. 1, pp. 78–84, Mar. 2005, doi: 10.1016/j.bbrc.2004.12.148.

[91] B. McCarte, O. T. Yeung, A. J. Speakman, A. Elfick, and K. E. Dunn, "Using ultraviolet absorption spectroscopy to study nanoswitches based on non-canonical DNA structures," *Biochem Biophys Rep*, vol. 31, Sep. 2022, doi: 10.1016/j.bbrep.2022.101293.

[92] D.-U. Li *et al.*, "Real-time fluorescence lifetime imaging system with a 32 × 32 0.13μm CMOS low dark-count single-photon avalanche diode array," *Opt Express*, vol. 18, no. 10, pp. 10257–10269, 2010, doi: 10.1364/OE.18.010257.

[93] Hamamatsu Photonics, *Photomultiplier Tubes: Basics and Applications.*, 3rd ed. 2007.

[94] S. Burri, C. Bruschini, and E. Charbon, "LinoSPAD: A compact linear SPAD camera system with 64 FPGA-based TDC modules for versatile 50 ps resolution time-resolved imaging," *Instruments*, vol. 1, no. 1, Dec. 2017, doi: 10.3390/instruments1010006.

[95] F. Zappa, S. Tisa, A. Tosi, and S. Cova, "Principles and features of single-photon avalanche diode arrays," *Sens Actuators A Phys*, vol. 140, no. 1, pp. 103–112, Oct. 2007, doi: 10.1016/j.sna.2007.06.021.

[96] J. Richardson *et al.*, "A 32×32 50ps resolution 10 bit time to digital converter array in 130nm CMOS for time correlated imaging," in *Proceedings of the Custom Integrated Circuits Conference*, 2009, pp. 77–80. doi: 10.1109/CICC.2009.5280890.

[97] H. Chen, "Design and implementation of high linearity FPGA-TDCs and an integrated large scale TCSPC system for time-resolved applications," Doctoral thesis, University of Strathclyde, Glasgow, 2020. doi: 10.48730/d58m-pt35.

[98] I. Rech *et al.*, "Optical crosstalk in single photon avalanche diode arrays: a new complete model," *Opt Express*, vol. 16, no. 12, pp. 8381–8394, 2008, doi: 10.1364/OE.16.008381.

[99] Y. Liu *et al.*, "Accurate Prediction of Photon Detection Probability Based on the 2-D Dead-Space Model for SPADs," *IEEE Sens J*, vol. 23, no. 2, pp. 1115–1123, 2023, doi: 10.1109/JSEN.2022.3226237.

[100] E. Slenders *et al.*, "Cooled SPAD array detector for low light-dose fluorescence laser scanning microscopy," *Biophysical Reports*, vol. 1, no. 2, Dec. 2021, doi: 10.1016/j.bpr.2021.100025.

[101] X. Meng, D. G. Cunningham, I. H. White, and R. V Penty, “SPAD-Array Contention Signal and Noise Model Suitable for Multilevel Modulation Schemes With Signal Processing,” *IEEE Access*, vol. 9, pp. 48483–48500, 2021, doi: 10.1109/ACCESS.2021.3068314.

[102] H. Mahmoudi, M. Hofbauer, B. Goll, and H. Zimmermann, “Noise and breakdown characterization of SPAD detectors with time-gated photon-counting operation,” *Sensors*, vol. 21, no. 16, Aug. 2021, doi: 10.3390/s21165287.

[103] M. Y. Berezin and S. Achilefu, “Fluorescence lifetime measurements and biological imaging,” *Chem Rev*, vol. 110, no. 5, pp. 2641–2684, May 2010, doi: 10.1021/cr900343z.

[104] S. Krishna, F. Alnaimat, A. Hilal-Alnaqbi, S. Khashan, and B. Mathew, “Dielectrophoretic 3D-focusing for on-chip flow cytometry,” *Micro Nano Lett*, vol. 15, no. 5, pp. 296–301, Apr. 2020, doi: 10.1049/mnl.2019.0404.

[105] G. Goddard, J. C. Martin, S. W. Graves, and G. Kaduchak, “Ultrasonic particle-concentration for sheathless focusing of particles for analysis in a flow cytometer,” *Cytometry Part A*, vol. 69, no. 2, pp. 66–74, Feb. 2006, doi: 10.1002/cyto.a.20205.

[106] M. Reisbeck *et al.*, “Hybrid integration of scalable mechanical and magnetophoretic focusing for magnetic flow cytometry,” *Biosens Bioelectron*, vol. 109, pp. 98–108, Jun. 2018, doi: 10.1016/j.bios.2018.02.046.

[107] J. Zhao and Z. You, “Microfluidic hydrodynamic focusing for high-throughput applications,” *Journal of Micromechanics and Microengineering*, vol. 25, no. 12, Oct. 2015, doi: 10.1088/0960-1317/25/12/125006.

[108] A. J. De Mello and J. B. Edel, “Hydrodynamic focusing in microstructures: Improved detection efficiencies in subfemtoliter probe volumes,” *J Appl Phys*, vol. 101, no. 8, 2007, doi: 10.1063/1.2721752.

[109] X. Yuan, A. Glidle, H. Furusho, and H. Yin, “A 3D hydrodynamic flow-focusing device for cell sorting,” *Microfluid Nanofluidics*, vol. 25, no. 3, Mar. 2021, doi: 10.1007/s10404-021-02425-y.

[110] J. Comas-Riu and N. Rius, “Flow cytometry applications in the food industry,” *Journal of Industrial Microbiology and Biotechnology*, vol. 36, no. 8. pp. 999–1011, Aug. 2009. doi: 10.1007/s10295-009-0608-x.

[111] S. Bohne, M. Heymann, H. N. Chapman, H. K. Trieu, and S. Bajt, “3D printed nozzles on a silicon fluidic chip,” *Review of Scientific Instruments*, vol. 90, no. 3, Mar. 2019, doi: 10.1063/1.5080428.

[112] O. O. Dada, B. J. Huge, and N. J. Dovichi, “Simplified sheath flow cuvette design for ultrasensitive laser induced fluorescence detection in capillary electrophoresis,” *Analyst*, vol. 137, no. 13, pp. 3099–3101, Jul. 2012, doi: 10.1039/c2an35321k.

[113] microfluidic ChipShop, “Lab-on-a-Chip Catalogue.” Accessed: Mar. 13, 2023. [Online]. Available: https://www.microfluidic-chipshop.com/wp-content/uploads/2022/02/Lab-on-a-Chip-Catalogue-02_2022.pdf

[114] J. P. Robinson and G. Grégori, “Principles of Flow Cytometry,” in *Flow Cytometry with Plant Cells*, 2007, pp. 19–40. doi: https://doi.org/10.1002/9783527610921.ch2.

[115] S. J. Hao, Y. Wan, Y. Q. Xia, X. Zou, and S. Y. Zheng, “Size-based separation methods of circulating tumor cells,” *Advanced Drug Delivery Reviews*, vol. 125. Elsevier B.V., pp. 3–20, Feb. 01, 2018. doi: 10.1016/j.addr.2018.01.002.

[116] R. Tennant and P. Rutten, “Calibration Protocol - Fluorescence Standard Curve with Fluorescein,” protocols.io. Accessed: Dec. 25, 2022. [Online]. Available: dx.doi.org/10.17504/protocols.io.zgkf3uw

[117] New Era, “NE-300 Infusion Pump manual,” 2016. Accessed: Jan. 30, 2023. [Online]. Available: https://www.syringepump.com/download/NE-300%20Just%20Infusion%20User%20Manual.pdf

[118] J. B. Knight, A. Vishwanath, J. P. Brody, and R. H. Austin, “Hydrodynamic Focusing on a Silicon Chip: Mixing Nanoliters in Microseconds,” *Phys Rev Lett*, vol. 80, no. 17, pp. 3863–3866, Apr. 1998, doi: 10.1103/PhysRevLett.80.3863.

[119] Y. Fu and J. R. Lakowicz, “Enhanced fluorescence of Cy5-labeled DNA tethered to silver island films: Fluorescence images and time-resolved studies using single-molecule spectroscopy,” *Anal Chem*, vol. 78, no. 17, pp. 6238–6245, Sep. 2006, doi: 10.1021/ac060586t.

[120] R. Vaidyanathan, R. H. Soon, P. Zhang, K. Jiang, and C. T. Lim, “Cancer diagnosis: from tumor to liquid biopsy and beyond,” *Lab on a Chip*, vol. 19, no. 1. Royal Society of Chemistry, pp. 11–34, Jan. 07, 2019. doi: 10.1039/c8lc00684a.

[121] M. Ilié and P. Hofman, “Pros: Can tissue biopsy be replaced by liquid biopsy?,” *Transl Lung Cancer Res*, vol. 5, no. 4, pp. 420–423, Aug. 2016, doi: 10.21037/tlcr.2016.08.06.

[122] L. E. Moore, “The Advantages and Disadvantages of Endoscopy,” *Clin Tech Small Anim Pract*, vol. 18, pp. 250–253, 2003, doi: 10.1016/S1906-2867(03)00000-0.

[123] A. M. Lennon *et al.*, “Feasibility of blood testing combined with PET-CT to screen for cancer and guide intervention,” *Science (1979)*, vol. 369, no. 6499, Jul. 2020, doi: 10.1126/science.abb9601.

[124] R. K. Henderson *et al.*, “A 192x128 Time Correlated SPAD Image Sensor in 40-nm CMOS Technology,” *IEEE J Solid-State Circuits*, vol. 54, no. 7, pp. 1907–1916, Jul. 2019, doi: 10.1109/JSSC.2019.2905163.

[125] J. Spidlen *et al.*, “Data file standard for flow cytometry, version FCS 3.1,” *Cytometry Part A*, vol. 77, no. 1, pp. 97–100, Jan. 2010, doi: 10.1002/cyto.a.20825.

[126] M. Celestino and O. Horikawa, “Velocity Measurement Based On Image Blur,” *ABCM Symposium Series in Mechatronics*, vol. 3, pp. 633–642, 2008.

[127] R. C. Gonzalez, R. E. Woods, and S. L. Eddins, *Digital Image processing using MATLAB*, 3rd ed. Upper Saddle River, NJ: Pearson/Prentice Hall, 2004.

[128] R. S. Boogar, R. Gheshlaghi, and M. A. Mahdavi, “The effects of viscosity, surface tension, and flow rate on gasoil-water flow pattern in microchannels,” *Korean Journal of Chemical Engineering*, vol. 30, no. 1, pp. 45–49, Jan. 2013, doi: 10.1007/s11814-012-0119-8.

[129] A. B. Shrirao, R. S. Schloss, Z. Fritz, M. V. Shrirao, R. Rosen, and M. L. Yarmush, “Autofluorescence of blood and its application in biomedical and clinical research,” *Biotechnology and Bioengineering*, vol. 118, no. 12. John Wiley and Sons Inc, pp. 4550–4576, Dec. 01, 2021. doi: 10.1002/bit.27933.

[130] I. Gyongy *et al.*, “Cylindrical microlensing for enhanced collection efficiency of small pixel SPAD arrays in single-molecule localisation microscopy,” *Opt Express*, vol. 26, no. 3, p. 2280, Feb. 2018, doi: 10.1364/oe.26.002280.